Quantum Coherence in Molecular Magnets

Quantenkohärenz in Molekularen Magneten

Von der Fakultät für Mathematik und Physik der
Universität Stuttgart zur Erlangung der Würde eines Doktors der
Naturwissenschaften (Dr. rer. nat.) genehmigte Abhandlung

Vorgelegt von

Christoph Schlegel

aus Böblingen

Hauptberichter:	Prof. Dr. M. Dressel
Mitberichter:	Prof. Dr. E. Roduner
Mitberichter:	Dr. habil. Joris van Slageren
Tag der mündlichen Prüfung:	29. Oktober 2009

1. Physikalisches Institut der Universität Stuttgart

2009

Meinen Eltern

Contents

List of Abbreviations

AC	Alternating Current
BWO	Backward Wave Oscillator
CW	Continuous Wave
DC	Direct Current
ESEEM	Electron Spin Echo Envelope Modulation
ESR	Electron Spin Resonance
ENDOR	Electron Nuclear Double Resonance
FDMRS	Frequency Domain Magnetic Resonance Spectroscopy
FWHM	Full With at Half Maximum
INS	Inelastic Neutron Scattering
MW	Microwave
SMM	Single Molecule Magnet
SQUID	Superconducting QUantum Interference Device
VTI	Variable Temperature Insert
ZFS	Zero Field Splitting

List of Figures

List of Tables

Kurzfassung

Das Ziel dieser Arbeit war, Überlagerungszustände und kohärente Eigenschaften von molekularen Magneten zu untersuchen. Quantenkohärenz bezeichnet die Eigenschaft, dass die Wellenfunktionen zweier oder mehrerer Teilchen interferieren können. Dies bedingt eine feste Phasenbeziehung zwischen den beteiligten Wellenfunktionen. In kohärenten Systemen ist die Überlagerung von Zuständen möglich, in welchen alle Eigenzustände gleichzeitig vorhanden sind. Dieser Umstand ist seit dem Beginn der Entwicklung der Quantenmechanik bekannt, und hat eine grundlegende Bedeutung für den Übergang von der klassischen Physik zur Quantenphysik.

Zusätzlich können Superpositionszustände auch in Quantencomputern und der Quantenkryptographie angewandt werden. Quantencomputer sind Computer, bei welchen die Anwendung von Überlagerungs- und verschränkten Zuständen es möglich macht, bestimmte Probleme zu lösen, die mit klassischen Computern unlösbar wären. Es wurden Algorithmen wie die Faktorisierung großer Zahlen oder Quanten-Suchalgorithmen vorgeschlagen. Die kleinste Informationseinheit in einem Quantencomputer ist dabei ein Quantenbit (Qubit), welches durch die kohärente Überlagerung von zwei Basiszuständen in einem Zweiniveausystem dargestellt wird.

Erste Experimente zur Realisierung eines Quantencomputers wurden mit NMR-Spektroskopie, Photonen und Rydberg-Atomen unternommen. Die endgültige Implementierung eines anwendbaren Quantencomputers wird aber wahrscheinlich in einem Festkörpersystem mit Hilfe von Elektronenspins stattfinden. Dies stellt eine Herausforderung dar, da in einem Festkörper eine starke Kopplung der Spins mit der Umgebung stattfindet. Dadurch geht die Kohärenz schnell verloren. Da für einen Quantencomputer lange Kohärenzzeiten (T_2) vonnöten sind [1], ist es unabdingbar sowohl die Kohärenzzeiten selbst als auch die Dekohärenzpfade zu untersuchen. Die letzteren sind insbesondere interessant, da sie den relativen Einfluss verschiedener Dekohärenzmechanismen in verschiedenen Systemen bestimmen. Zudem erlaubt das Wissen über Dekohärenzprozesse die Verlängerung von Kohärenzzeiten über die gezielte Variation von zum Beispiel den Liganden in

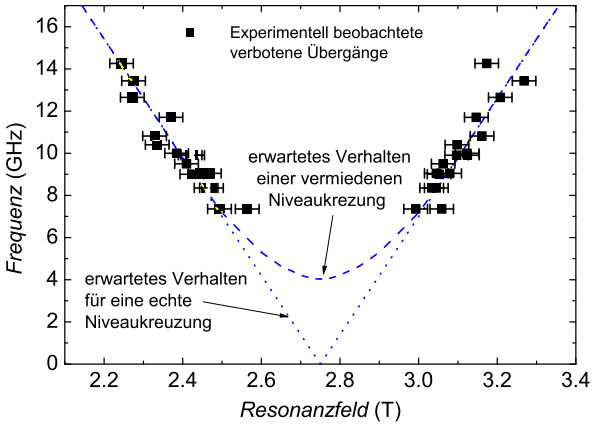

Abbildung 1: Experimentelle Frequenz in Abhängigkeit des Resonanzfeldes im molekularen Magneten V_{15} für $\vec{B}_0 \| \vec{B}_1$. Blaue gepunktete Linie: Erwartetes Verhalten eines Systems, welches eine echte Niveaukreuzung aufweist. Blaue gestrichelte Linie: Erwartetes Verhalten der Niveaus in einem System an einer Antikreuzung mit einer Aufspaltung von 4 MHz.

einem Komplex. In dieser Arbeit versuchen wir genau dieses Wissen zu erweitern.

Wir untersuchen die spektroskopischen Eigenschaften einer Klasse von molekularen Materialien welche molekulare Magnete genannt werden. Die Cluster bestehen aus paramagnetischen Übergangsmetallionen, die Spins sind dabei magnetisch gekoppelt. Die magnetischen Moleküle sind monodispers und können sehr gut mit einem Spin-Hamiltonian beschrieben werden. Sie stellen Modellsysteme zur Untersuchung von Nanomagnetismus und Dekohärenzeigenschaften dar.

Diese Arbeit verfolgt einen multidisziplinären Zugang zu diesem Problem, in dessen Zuge verschiedene Moleküle mit unterschiedlichen Methoden untersucht wurden. Dafür wurde auch ein neuer experimenteller Aufbau entwickelt und realisiert, um die magnetische Niveaustruktur direkt zu untersuchen, und die physikalischen Prinzipien, die die magnetischen Eigenschaften beeinflussen, zu identifizieren. In Kapitel 1 führen wir ausgewählte grundlegende Konzepte des molekularen Magnetismus ein. Darunter sind der Spin-Hamiltonian-Formalismus, welcher zur Beschreibung grundlegender physikalischer Eigenschaften wie magnetischer Anisotropie und Quantentunneln der Magnetisierung geeignet ist. Zudem führen wir Elektronenspinrelaxationsprozesse und den Begriff und die Bedeutung der

Kohärenz ein.

In Kapitel 2 beschäftigen wir uns mit der Elektronenspinresonanz (ESR). Hier präsentieren wir neben den Grundlagen der ESR den Dichtematrixformalismus und den Produktoperatorformalismus, welche zur Beschreibung der Elektronenspinrelaxation und von kohärenten Eigenschaften benötigt werden. Zudem beschreiben wir weitverbreitete experimentelle Prinzipien von Elektronenspinresonanzspektrometern, behandeln aber auch exotische Methoden, die nur von einzelnen Gruppen verwendet werden. Wir vermitteln dieses Hintergrundwissen, um die Notwendigkeit des später vorgestellten, neuartigen breitbandigen Elektronenspinresonanzaufbaus zu verstehen. In Kapitel 3 zeigen wir Entwicklungkriterien und grundlegende Eigenschaften des Aufbaus auf, und präsentieren Testmessungen mit verschiedenen Proben. Mit einem abstimmbaren Hohlraumresonator in Transmissionsgeometrie können wir die hohe Empfindlichkeit eines resonanten Aufbaus (Gütefaktor $Q > 1000$) mit der Abdeckung eines breiten Frequenzbereiches, welche normalerweise nur in nichtresonanten Aufbauten ($Q = 1$) erreicht wird, verbinden. Breitbandige Mikrowellenkomponenten, wie Koaxialkabel und ein Netzwerkanalysator, sind notwendig, um diesen speziellen Frequenzbereich abzudecken. Der Aufbau erlaubt Messungen in einem Freqenzbereich von 14–40 GHz, einem Magnetfeldbereich von 0–10 T und einem Temperaturbereich von 1,5–300 K. Der Frequenzbereich des Aufbaus kann durch das Einbringen von Dielektrika zu niedrigeren Frequenzen erweitert werden. Zudem ist es möglich die Probe in verschiedene Orientierungen des magnetischen Wechselfeldes $\vec{B}_1$ im Verhältnis zum statischen Magnetfeld $\vec{B}_0$ einzubringen. Durch die einzigartige Verbindung eines Frequenzbereiches von 5–40 GHz und hohen Magnetfeldern, ist es möglich spezielle Untersuchungen an ungepaarten Elektronenspins durchzuführen. Zum Beispiel untersuchten wir den molekularen Magneten V_{15}, da hier die Ursache der vermiedenen Niveaukreuzung bei ungefähr 2,75 T bisher nicht eindeutig bestimmt werden konnte. Sowohl Erklärungen über eine Assymetrie in der Molekülstruktur als auch der Einfluss von assymetrischer Austauschwechselwirkung oder Hyperfeinwechselwirkungen kommen dafür in Frage [2]. Indem der normalerweise in der ESR verbotene Übergang zwischen den $S = 1/2$ und $S = 3/2$-Multipletts in der parallelen Orientierung von magnetischem Wechselfeld und äußerem Magnetfeld bei verschiedenen Frequenzen aufgenommen wurde (siehe Abbildung 1), konnte das Verhalten der Niveaus nahe der Kreuzung bestimmt werden. Daraus können wir den Schluss ziehen, dass Wechselwirkungen wie die antisymmetrische Austauschwechselwirkung oder Hyperfeinkopplungen für die Aufspaltung verantwortlich sind, da die Assymetrie in der Molekülstruktur die Mischung der Nive-

aus nicht erklären kann. Für eine genaue Quantifizierung der Aufspaltung bei der Antikreuzung müssen noch Messungen bei niedrigeren Frequenzen durchgeführt werden.

In Kapitel 4 präsentieren wir Untersuchungen an dem antiferromagnetisch gekoppelten Ring Cr_7Ni, welcher einen molekularen Magneten mit einem $S = 1/2$ Spingrundzustand darstellt. Es wurden CW und gepulste Experimente an einem W-Band (94 GHz) ESR-Spektrometer durchgeführt, um Informationen über Relaxation und Kohärenz des Systems zu erhalten. Während die Relaxation der Magnetisierung und zum Teil auch die Elektronenspinrelaxation von molekularen Magneten schon im Detail untersucht wurden, ist wenig über die kohärenten Eigenschaften bekannt. Indem wir die Spin-Gitter-Relaxationszeiten bei unterschiedlichen Feldern verglichen haben, können wir ausschliessen, dass ein direkter Spin-Gitter-Relaxationsprozess verantwortlich ist. Die Phasengedächtniszeit T_2^* wurde zu (357 ± 10) ns bei 5 K bestimmt. Dieser Wert stimmt gut mit dem bei X-Band-Frequenz (9.5 GHz) bei 4.5 K gefundenen Wert [3] (379 ± 10) ns überein. Mit der Hilfe von gepulster ENDOR-Spektroskopie konnten wir die Hyperfeinkopplung des Elektronenspins an die Kernspins als den verantwortlichen Dekohärenzpfad ausmachen. Die Hyperfeinkopplungskonstante konnte zu $a_{\mathrm{iso}} = (-0.80 \pm 0.05)$ MHz bestimmt werden, wobei die Kopplungsstärke eine Verteilung in Folge der unterschiedlichen Abstände der Protonen zum Elektronenspinsystem zeigt.

In Kapitel 5 und 6 untersuchen wir Einzelmolekülmagnete der Fe_4-Familie. Einzelmolekülmagnete sind eine Untergruppe der molekularen Magnete; sie zeigen bei tiefen Temperaturen eine langsame Relaxation der Magnetisierung und besitzen damit eine magnetische Bistabilität einzig basierend auf molekularen Eigenschaften. Zuerst haben wir die magnetischen Eigenschaften zweier Fe_4-Verbindungen, sowohl in Pulverproben als auch in gelöstem Zustand, untersucht. Hiermit wollten wir den Einfluss der Umgebung auf die molekularen magnetischen Eigenschaften feststellen. Normalerweise werden die magnetischen Eigenschaften eines Einzelmolekülmagneten als Verhalten eines einzelnen Moleküls erklärt. Dabei wird der Einfluss der Umgebung vernachlässigt. Für die Beschreibung von manchen Eigenschaften mag dies ausreichend sein, aber wenn es um die exakte Energieniveaustruktur oder kohärente Eigenschaften geht, spielt die Umgebung eine entscheidende Rolle. Zum Beispiel können kleine Verzerrungen in der Molekülstruktur zu veränderten Energieniveaus führen. Durch das Verdünnen in einem Lösungsmittel können die intermolekularen Wechselwirkungen verringert werden. Und auch die Kernspins des Lösungsmittels beeinflussen die Kohärenzeigenschaften, wie wir

später sehen werden.

Wir führten eine umfassende magnetische Charakterisierung von zwei Fe_4-Verbindungen durch, namentlich $[Fe_4^{III}(acac)_6(Br\text{-}mp)_2]$ **(1)** und $[Fe_4^{III}(acac)_6(tmp)_2]$ **(2)**. Messungen der AC-Suszeptibilität bei tiefen Temperaturen zeigen eine langsame Relaxation der Magnetisierung, wobei langreichweitige Ordnung als Grund hierfür ausgeschlossen werden konnte. Sowohl die effektive Barriere die der Inversion der Magnetisierung entgegensteht, als auch der Frequenzfaktor ändern sich, wenn die Moleküle in Lösung gegeben werden. Dies bringen wir mit Verzerrungen des Moleküls in gefrorener Lösung, beziehungsweise mit der unterschiedlichen Schallgeschwindigkeit von Pulver und Lösung, in Verbindung. Um die Spin-Hamiltonian-Parameter festzustellen, führten wir ESR-Messungen in der Feld-und Frequenzdomäne durch. Eine Simulation einer W-Band-Messung von **(1)** resultierte in der Bestimmung einer negativen axialen Anisotropie mit einem Nullfeldaufspaltungsparameter von $D = (-0.3429 \pm 0.0005)\,\mathrm{cm}^{-1}$ unter der Verwendung eines $S = 5$ Gesamtspins. Messungen an einer gefrorenen Lösung von **(1)** in verschiedenen Lösungsmitteln zeigten eine stark abweichende Linienform, die aber trotzdem mit einem ähnlichen Spin-Hamiltonian, jedoch mit wesentlich größerer Linienbreite simuliert werden konnte. Dieses Ergebnis unterstreicht einerseits die Gültigkeit des Spin-Hamiltonian-Modells, welches Wechselwirkungen zwischen Molekülen vernachlässigt. Andererseits eröffnen die in Lösung immer noch vorhandenen Einzelmoleküleigenschaften die Möglichkeit, kohärente Eigenschaften bei signifikant reduzierten magnetodipolaren Wechselwirkungen, das heisst praktisch bei niedriger Konzentration, zu messen. Diese Eigenschaften wiederum sind stark von der Umgebung abhängig. Zusätzlich zeigen die erhaltenen Spin-Hamiltonian-Parameter im Vergleich mit Literaturwerten [4], dass die Anisotropiebarriere durch den gezielten Austausch von Liganden in einem breiten Bereich variiert werden kann.

Kapitel 6 beschreibt den ersten direkten Nachweis von Quantenkohärenz in einem Einzelmolekülmagneten. Einzelmolekülmagnete haben für die Verwendung als Qubits mehrere Vorteile: Durch die Ausnutzung der magnetischen Anisotropie, das heisst der Aufspaltung der magnetischen Energieniveaus im Nullfeld, können Superpositionszustände mit einer geeigneten Mikrowellenfrequenz im Nullfeld hergestellt werden. Darüberhinaus kann das Mehrniveausystem des Grundzustandes eines Einzelmolekülmagneten zur Implementierung von Algorithmen genutzt werden, welche in einem Zweiniveausystem nicht möglich sind [5]. Kohärenzzeiten in molekularen Magneten wurden in der Größenordnung von 10 ns erwartet [6] [7] [8]. Wir konnten die mit den Kohärenzzeiten eng verknüpften

Phasengedächtniszeiten direkt mit gepulster W-Band ESR-Spektroskopie bestimmen. Darüberhinaus konnten wir über die gezielte Variation des Lösungsmittels Phasengedächtniszeiten signifikant verlängern. Die Dephasierungszeit T_2^* für **(1)** wurde mit 614 ns in Toluol bei 4.3 K bestimmt. T_2^* stellt eine untere Grenze für die Kohärenzzeit T_2 dar, da für den Verlust der Phaseninformation zusätzlich andere Prozesse eine Rolle spielen. Hierzu wurde die Konzentration von **(1)** in Lösung so lange verringert bis keine Änderung in den Phasengedächtniszeiten mehr zu sehen war; damit sind magnetodipolare Wechselwirkungen als Dekohärenzpfad auszuschließen. Unter der Verwendung des Lösungsmittels CS_2, welches nahezu keine ungepaarten Kernspins besitzt, konnten die Phasengedächtniszeiten weiter bis auf 1.27 μs verlängert werden, was zwei Größenordnungen länger ist als die prognostizierten Zeiten. Einzelmolekülmagnete stellen schon mesoskopische Systeme am Übergang von Quantensystemen zu klassischen Systemen dar, da sich viele gekoppelte Spins kohärent verhalten müssen, ist die langlebige Quantenkohärenz ein verblüffendes Ergebnis. Zusätzlich untersuchten wir die verantwortlichen Dekohärenzpfade mit ESEEM (Electron Spin Echo Envelope Modulation) Spektroskopie und mit echodetektierter ESR. Wir konnten zeigen, dass der Elektronenspin sowohl an die Kernspins des Lösungsmittels, als auch an die intramolekularen Protonen gekoppelt ist. Eine Erklärung für den starken Einfluss der Lösungsmittelkernspins konnten wir mit einem möglichen π-Stacking der aromatischen Lösungsmittelmoleküle zwischen zwei Liganden des Fe_4-Moleküls erklären. Die Analyse der Temperaturabhängigkeit der Spingitterrelaxationszeit T_1 zeigte einen dominierenden Einfluss eines Orbach-Prozesses auf die Relaxation. Hierbei handelt es sich um einen Zwei-Phononenprozess, für welchen die Absorption von Phononen über ein höherliegendes Energieniveau angenommen wird. Dieses liegt nach unseren Messungen innerhalb des Grundzustandmultipletts, wodurch höherliegende m_S-Niveaus eine entscheidende Rolle bei der Relaxation spielen. Schliesslich gelang uns die Präparation von einem beliebigen Überlagerungszustand zwischen zwei Spinniveaus. Die Rabi-Oszillationen, die dabei beobachtet werden konnten (siehe Abbildung 2), gelten als Voraussetzung für die Anwendung eines Systems als Qubit.

Für zukünftige Experimente spielen weitere limitierende Faktoren über die Kopplung zu Kernspins hinaus eine wichtige Rolle. Fe_4 gelöst in CS_2 hat bei 4.3 K eine ähnliche Relaxationszeit (T_1) wie Phasengedächtniszeit (T_2^*). Falls nun einem Gedankenexperiment alle Protonen aus dem Mokekül entfernt werden, so erwarten wir dass T_2^* von T_1 begrenzt wird (da $T_2 < 2T_1$ [9]). Da die Spingitterrelaxation von einem Orbach-Prozess bestimmt wird, und dieser Prozess für an-

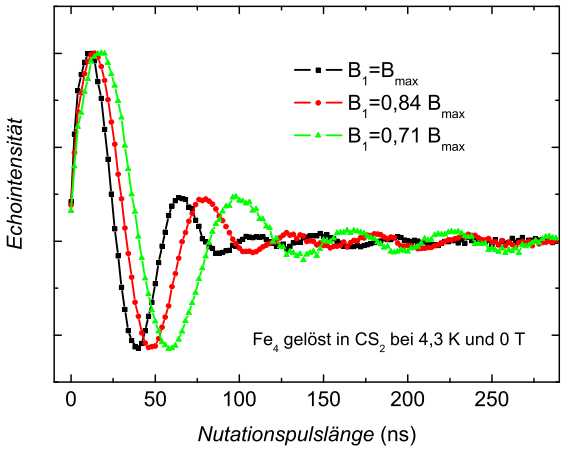

Abbildung 2: Rabi-Oszillationen von Fe_4 gelöst in CS_2 bei verschiedenen Feldstärken des magnetischen Wechselfeldes.

dere Hochspinsysteme auch zu erwartet ist, können wir annehmen, dass dies eine generelle Beschränkung für T_2 in Einzelmolekülmagneten darstellt. Dehalb ist es wahrscheinlich dass wesentlich längere Kohärenzzeiten in Einzelmolekülmagneten als die hier beobachteten nur bei niedrigen Temperaturen erreicht werden können.

Die hier gezeigte Bestimmung von Kohärenzzeiten in Einzelmolekülmagneten eröffnet viele neue Perspektiven. Die erste Hürde für die Verwendung von solchen Systemen als Qubits ist genommen. Es ist interessant, die Kohärenzzeiten weiterer Hochspinsysteme zu untersuchen um festzustellen ob dort ähnlich lange Kohärenzzeiten gemessen werden können. Darüberhinaus hilft die Identifizierung der Dekohärenzpfade bei der zielgerichteten Synthese von weiteren, kohärenzzeitoptimierten Verbindungen. Ein vielversprechender Weg könnte die Verwendung von Polyoxometallat-basierten molekularen Magneten sein, welche als Systeme ohne ungepaarte Kernspins synthetisiert werden können. Der nächste logische Schritt, das heisst die Herstellung von gekoppelten molekularen Magneten wird zu der Möglichkeit der Verschränkung von Zuständen führen. Die Erkenntnis, dass die Eigenschaften von Einzelmolekülmagneten in Lösung großteils erhalten bleiben, und dass Kohärenzzeiten durch die Variation des Lösungsmittels verlängert werden konnten, regt weitere Untersuchungen an Einzelmolekülmagneten in anderen Umgebungen wie zum Beispiel auf Oberflächen an.

Chapter 1

Introduction to Molecular Magnetism

Abstract. In this chapter, we introduce selected facets of molecular magnetism. First, magnetic anisotropy of purely molecular origin as a key feature of single-molecule magnets is explained. Then, we introduce the spin Hamiltonian formalism, making the reader familiar with the important interactions necessary to understand the energy level structure of molecular spin systems. The relaxation of the magnetization of a single molecule magnet over the anisotropy barrier is distinguished from the spin-lattice relaxation time. We describe the most important mechanisms on the microscopic level that are responsible for spin-lattice relaxation in solids. Finally, we discuss coherent properties of spin systems, and the relevance of long coherence times for quantum information processing.

1.1 Overview

Magnetic properties of matter have attracted attention for a long time: From the discovery of the properties of lodestone ($FeO - Fe_3O_4$) of the ancient Greece and China, through the application of lodestone in a compass, the discovery of the connection between electricity and magnetism in the 19th century to the modern understanding of magnetism given by quantum mechanics. Magnetic materials are essential for many technical applications: They are central parts in electrical motors, generators, hard disks, avalanche transceivers, loudspeakers, magnetic resonance imaging and so on. Thus, many research institutes and companies nowadays still investigate the potential of new magnetic materials, with the goal of improved properties or even new groundbreaking applications.

Molecular magnetism is a research area which deals with the design, synthesis and investigation of magnetic properties of molecular and molecule-based materials. It is not limited to spin clusters, called molecular magnets. Spin clusters show magnetic properties, where interactions between different molecules can be

neglected in first approximation, making them point-like zero-dimensional magnets. Molecular magnetism also deals with, for example, spin-crossover compounds that show different spin states between low and high temperatures. The transition between the different spin values can also be induced by pressure or light. Moreover, single-chain magnets (SCMs) are an interesting class of molecular polymeric materials. Because they show a magnetic hysteresis behavior in single polymeric chains, they can be considered to be one-dimensional magnets. Compared to standard solids, molecular magnetic materials have an important advantage, in that their properties are easily tunable: Changing a side group or a counter ion may change the electronic structure in a favorable way.

A molecular magnet is a molecule with one or more exchange coupled magnetic centers. During the last 15 years a special class of molecular magnets has drawn a lot of attention: Single-molecule magnets (SMMs), which behave as tiny magnets at low temperatures, showing slow relaxation of the magnetization. This leads to the observation of a hysteresis cycle, like in bulk magnets. The difference to bulk magnets is, that the magnetic properties are of purely molecular origin. Thus, one can for example dilute SMMs without changing their basic properties. Moreover, molecular magnets are monodisperse in contrast to e.g. magnetic nanoparticles, which means all molecules are the same.

Molecular magnets are mesoscopic materials, being at the frontier between the microscopic and the macroscopic world. Because mesoscopic objects are often in the nanometer size-regime, mesoscopic physics is normally thought of as a discipline of nanoscience. In contrast to most nanotechnological approaches, which include top-down techniques like lithography, molecular magnets are fabricated in a bottom-up approach. For mesoscopic systems, both quantum mechanics and classical physics are necessary to describe the properties. In the case of molecular magnets the magnetic properties lie between those of a quantum spin and a bulk magnet. Investigating mesoscopic systems helps us to understand how classical properties evolve from quantum mechanical properties from smaller to larger systems.

1.2 Magnetic Anisotropy and Spin Hamiltonian

Magnetic anisotropy is the property of a magnetic system to have a preferred orientation of the spin with respect to the quantization axis, in the case of molecular magnets a molecular axis. It is the crucial phenomenon underlying all applications

of magnetism in information storage systems. The two orientations (sometimes called 'spin-up' and 'spin-down') represent the bits, that means the smallest unit of information in a binary system.

The energies of a system can be described with a Hamiltonian, which determines the energy levels. The complete Hamiltonian and its solution for a molecular system is very complex, thus for the focus on the important lowest lying levels the spin Hamiltonian approach [10] was developed: It allows to interpret spectra without using fundamental theories. This makes it a phenomenological model, which implies that there are several approximations involved. In the following, we present the most common spin Hamiltonian terms used in molecular magnetism:

$$\text{Zeeman interaction: } H_{\text{Zeeman}} = \mu_B \mathbf{S} \cdot \mathbf{g} \cdot \mathbf{B}_0 \tag{1.1}$$

The Zeeman interaction describes the splitting of the energy levels due to an external magnetic field $\mathbf{B}_0$.[1] In Eq. (1.1) $\mathbf{S}$ is the spin operator, μ_B is the Bohr magneton, and $\mathbf{g}$ is the g-tensor, which is isotropic and 2.002319 for a free electron.

$$\text{Zero-field splitting: } H_{\text{ZFS}} = \mathbf{S} \cdot \mathbf{D} \cdot \mathbf{S} + \sum_{N,k} B_N^k \mathbf{O}_N^k \tag{1.2}$$

The different m_S states that are split in zero external field are described by the zero-field splitting term (Eq. (1.2)). The first term describes the zero-field splitting for a system with axial or rhombic symmetry, where $\mathbf{D}$ is the zero-field splitting tensor. This tensor is in normally given in ESR by the axial (D) and transverse (E) zero-field splitting parameters: $H_{\text{ZFS}} = \mathbf{S} \cdot \mathbf{D} \cdot \mathbf{S} = D\left[S_z^2 - \frac{1}{3}S(S+1)\right] + E(S_x^2 - S_y^2)$. It has to be taken care, that S_z in this formula donate a spin operator (see also Eq. (2.3)), and S is the total spin. The eigenstates of the first term in this equation are the m_S states themselves, whereas the second term mixes states with $\Delta m_S = \pm 2$. For $D < 0$ the axial term can lead to an energy barrier in between the lowest lying m_S levels which then leads to slow relaxation of the magnetization, in combination with phonon induced transition selection rules. The mixing of levels caused by transverse terms can lead to quantum tunneling of the magnetization. The second term in Eq. (1.2) is necessary to

[1] We use today's definition of the fields $\mathbf{B}$ and $\mathbf{H}$ [11] [12]: $\mathbf{B}$ is the fundamental quantity, e.g. the externally applied magnetic field in an ESR experiment. $\mathbf{H}$ is a derived field, considering the magnetic fields produced by a material. $\mathbf{H}$ is defined by $\mathbf{H} \equiv \mathbf{B}/\mu_0 - \mathbf{M}$, where $\mathbf{M}$ is the magnetization of the material and μ_0 is the permeability of free space. The unit of $\mathbf{B}$ in the SI system is Tesla (T), wheras $\mathbf{H}$ is measured in Ampere per meter (A/m).

describe higher-order splittings, if present, in systems with $S \geq 3/2$. Here, $\mathbf{O}_N^k$ are the Stevens operators [13], where $N = 2, 4, 6, ..., 2S$ and $-N \leq k \leq N$.

$$\text{Exchange interaction: } H_{\text{exchange}} = -2J\mathbf{S}_1 \cdot \mathbf{S}_2 \tag{1.3}$$

The Heisenberg or isotropic exchange Hamiltonian describes interactions between unpaired electrons; J is the exchange coupling constant. If the exchange interaction is much stronger than the magnetic anisotropy, S and M_S are good quantum numbers. This approximation is valid for many single molecule-magnets (for example Mn_{12} derivates, Fe_4 molecules). Thus, is is possible to use Eq. (1.2), which only describes single-ion anisotropy, to model the lowest lying energy levels of a coupled spin system. This approximation can then describe the observed properties of a system in the spin ground state at low temperatures.

$$\text{Hyperfine interaction: } H_{\text{HF}} = \mathbf{I} \cdot \mathbf{A} \cdot \mathbf{S} \tag{1.4}$$

The hyperfine interaction describes the coupling of the electron spin to nuclear spins in the molecule. Here, A is the hyperfine splitting tensor. Hyperfine interactions are much smaller than electron-electron interactions (due to the smaller nuclear magnetic moment).

1.3 Quantum Tunneling

Quantum tunneling is an effect, where a particle tunnels through a potential barrier, which could not be overcome in classical physics. Quantum tunneling is the origin of the alpha decay in nuclear physics, and is also applied in scanning tunneling microscopes and many other applications.

Magnetic quantum tunneling was discovered early in the research on molecular magnets, and remains one of the most striking quantum phenomena in these systems. Experimentally, tunneling can be identified by the occurrence of steps in the magnetization in a hysteresis curve (Fig. 1.1(a)) [14] [15]. Considering a spin system with an easy axis anisotropy $H = -DS_z^2 + \mu_B g B_0$. At low temperatures, the lowest lying, degenerate levels in the double-well potential are occupied. The spin is now restricted to either side of the barrier. If now a finite transverse anisotropy $E(S_x^2 - S_y^2)$ is taken into account, different m_S levels mix. Both split eigenstates are now simultaneously occupied. Using the time evolution of the system, the spin tunnels with a frequency $\Delta/\hbar$, where Δ is the energy splitting between the tunnel split states. The mixing of states at the left and right side of

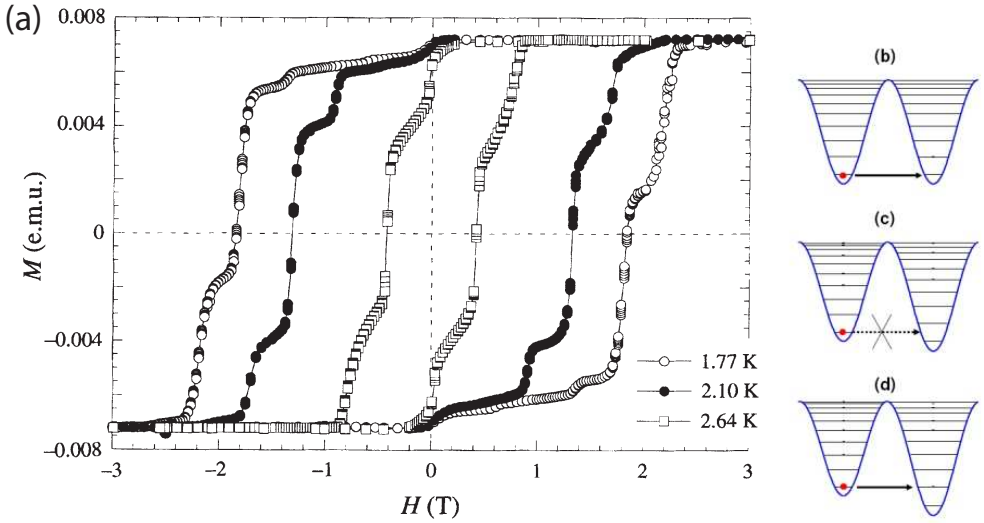

Figure 1.1: (a) Magnetization hysteresis loops of a Mn_{12} single-molecule magnet from [14]. The curve exhibits steps where quantum tunneling contributes to the relaxation process.
(b) Ground state tunneling for zero external magnetic field.
(c) Tunneling is suppressed, because the levels are not degenerate at the chosen field.
(d) Tunneling at finite field, where the energy of different m_S levels match.

the barrier is only possible if the states are degenerate, this means only if B_0 is 0 or corresponds to a value where two levels are again degenerate, tunneling may take place (Fig. 1.1(b) and (d)). In a hysteresis cycle the external magnetic field is swept. If now two energy levels are degenerate, steps in the magnetization are observed, because the relaxation rate is increased significantly due to tunneling.

If quantum tunneling is present, thermal relaxation over the barrier is not the only mechanism to flip the spin. Thus, the classical energy barrier obtained from e.g. spectroscopic measurements of the spin level separations will differ from the effective barrier against magnetization reversal gained from e.g. AC susceptibility measurements. This opens another way to determine the influence of quantum tunneling besides the magnetization measurements at very low temperatures. If the classical barrier is higher than the effective energy barrier, it is possible to quantify the influence of quantum tunneling.

1.4 Relaxation of the Magnetization

In this section, we discuss the thermally activated relaxation of the magnetization over the barrier in single-molecule magnets. The material is magnetized in a certain external magnetic field B_0. After that, the field is either removed or changed, and the time-dependence of the magnetization is monitored. We discuss the situation, where the relaxation is exponential, that means where the time-dependence of the magnetization is [16]

$$M(t) = M_{\text{equilibrium}} + M_0 e^{-t/\tau}. \tag{1.5}$$

Herein τ is the relaxation time. In many cases the temperature dependence of the relaxation of the magnetization is represented by the Arrhenius formula

$$\tau(T) = \tau_0 e^{\Delta_{\text{eff}}/(\mathrm{k}_B T)}. \tag{1.6}$$

Here, τ_0 is the attempt relaxation rate and Δ_{eff} is the effective energy barrier. At low temperatures, the relaxation of the magnetization is slower than at high temperatures. If there is no tunneling involved in the relaxation, the energy barrier for an axial high-spin single-molecule magnet is $\Delta = |D|\, S^2$.

1.5 Electron Spin Relaxation

In this section, we discuss electron spin relaxation, that means the relaxation of the electron spin from an excited state to the ground state. This process can be

observed in any electron spin system, and a barrier against magnetization reversal is not necessary as in Chapter 1.4. If an electron spin system is perturbed, it relaxes back to its equilibrium state. The time constant at which this occurs, is the spin-lattice relaxation time (T_1), sometimes also called longitudinal relaxation time. In a relaxation process, the spin system exchanges energy with the environment, for example by spontaneous emission of electromagnetic radiation or spin-phonon coupling. Thus, the energy of the spin system changes. This is in contrast to decoherence (Chapter 1.6), where no exchange of energy with the environment is needed. In solids, relaxation is due to the the absorption or stimulated emission of phonons, therefore in these systems the relaxation is called spin-lattice-relaxation. The spontaneous emission by a magnetic dipole does not play a significant role in relaxation at normal experimental conditions. Even at 1 THz ($T_1 \propto 1/f^3$) the rate of spontaneous emission is of the order of years [9].

The microscopic processes in solids for spin flips induced by the absorption of phonons are the direct process (one-phonon), the Raman process and the Orbach process (which are both two-phonon processes). In the direct process, one phonon is absorbed, with the Larmor frequency ω_L. At higher temperatures ($T > \frac{\hbar\omega_L}{k_B}$) this process becomes inefficient, because the phonon density will be at its maximum for frequencies $\omega_{\max} > \omega_L$. Here the Raman process, which involves the absorption of a phonon of higher frequency via a virtual level becomes important. This process leads to a typical temperature dependence of $T_1 \propto T^{-9}$ (for half-integer spin systems) or $T_1 \propto T^{-7}$ (for integer spin systems) [9]. If the phonon absorption does not take place via a virtual level, but via a real excited level (e.g. an excited spin state), the process is called Orbach process. Because the transition probability to this real level is higher than to a virtual one, the efficiency of the two-phonon process increases. For an Orbach process, the temperature dependence of the relaxation time is given by $1/T_1 \propto \frac{\Delta^3}{e^{\Delta/k_BT}-1}$ [13]. Thus, one can determine the energy difference Δ from the ground to the excited state which is involved in the transition.

Because spin-lattice relaxation times will be studied for different molecular magnets in this thesis, in the following we will review timescales and relaxation processes from literature: In the study of del Barco *et al.* [7] the longitudinal relaxation time of the SMM Fe_4 was measured to be 25-44 s (dependent on field). Mitrikas *et al.* [17] measured the spin-lattice relaxation time of a trinuclear iron (III) ($S = 1/2$) complex using pulsed ESR with the relaxation time $T_1 \approx 0.7$ ms at 5.5 K. The temperature dependence indicated an Orbach process being responsible for the relaxation, because the fit for a Raman process led to an unusually

large exponent. In the SMM Fe_8, spin-lattice relaxation times were found to be in the order of 2 μs at 1.6 K in a pump-probe experiment [18]. In this study, hyperfine interaction is considered to be responsible for most of the relaxation. In magnetization measurements combined with short radiation pulses performed by Bal *et al.* [19], T_1 was calculated to be $T_1 \approx 40$ ns. Takahashi *et al.* [20] studied the single-molecule magnet Fe_8 with pulsed ESR. Here, spin-lattice relaxation times were found to be $T_1 \approx 1$ ms, and thus significantly longer than in the studies of Bahr *et al.* [18] and Bal *et al.* [19]. In the molecular magnet Cr_7Ni, Ardavan *et al.* [3] determined T_1 to be up to $T_1 \approx 1$ ms at 1.8 K.

1.6 Electron Spin Coherence

The ability of wavefunctions of objects to interfere is called quantum coherence. Quantum coherence implies that there is a fixed phase relationship between the wave functions of the two objects. For a coherent system, a superposition of states is possible:

$$|\psi\rangle = \sum_n c_n |\psi_n\rangle \tag{1.7}$$

In a quantum superposition state, e.g. $|\psi\rangle = (|0\rangle + |1\rangle)/\sqrt{2}$, both components are simultaneously present, it is not a statistical distribution of component states.
Recently, the transition of the quantum mechanical to the classical world that we live in has received a great deal of attention [21]. The distinguishing property of the quantum world is the above mentioned quantum coherence. For a single spin $s = 1/2$, like electrons or protons, coherent properties are well-known and have been used extensively over decades in pulsed ESR and NMR. But the bigger and more complex a system is, the more likely it is, that it has interactions with its surrounding or with parts of itself. In molecular magnets, long-living quantum coherence was not expected to be present, because these molecules consist typically of more than 100 atoms, and contain tens of electron spins. In contrast to spin-lattice relaxation (see Chapter 1.5), the decay of coherence, also called transverse relaxation or spin-spin relaxation, does not require an exchange of energy with the environment [9].
The period during which the phase of the wavefunction remains intact is the coherence time, T_2. Directly accessible in a pulsed ESR experiment (Chapter 2.2.2) is the phase-memory time T_2^*, sometimes also denoted with T_m. Please note that not only spin-spin relaxation, but also processes such as spectral, spin and in-

stantaneous diffusion contribute to T_2^* [9]. T_2^* therefore gives a lower limit for T_2.

During the last two decades, different approaches for a physical implementation of a quantum computer were investigated. Requirements for this implementation of quantum computation were discussed by DiVincenzo [1]. He gives five criteria, amongst which one is long relevant decoherence times, which are much longer than the gate operation time. An exact requirement cannot be given, because the needed coherence times are also dependent on quantum error correction. Molecular magnets are a promising system for the use as a qubit because of several reasons, which we will discuss in the following. First, molecular magnet qubits are easier to address than single spins, due to the rather large size of the spin cluster [22]. In a straightforward proposal for the realization of qubits in single-molecule magnets two options were considered [23]: The two states of a qubit can be the ground state and first excited state, or they can be the symmetric and antisymmetric combinations of the twofold lowest lying states in a system with strong ground state tunneling.

For the Cr_7Ni molecular ring, Troiani *et al.* [24] suggested to realize one-qubit and two-qubit gates without an individual addressing of the rings by using local magnetic fields. Further, two Cr_7Ni molecules were chemically linked [25], creating a three-qubit system. The coupling between the molecules can be tuned by choosing the linker molecule. Additionally, microwave pulse sequences for the creation of entangled states were proposed.

Single molecule magnets exhibit a high total spin, and the resulting magnetic sublevels are split in zero magnetic field (Chapter 1.2). With the resulting high number of spin projections, complex superpositions of magnetic sublevels are possible. These allow to process more quantum information at the same time than in a two-level qubit. A detailed proposal of how this could be used to implement Grover's algorithm in a single molecule magnet, was published by Leuenberger and Loss [5].

The signal obtained in the readout step of a quantum operation decreases exponentially with increasing qubit number, if the thermal energy exceeds the energy splitting of the quantum states involved [26]. This leads to a further advantage of single-molecule magnets, namely the possibility to employ numerous single-molecule qubits without this exponential decrease in signal. With the typical energy splitting between magnetic sublevels at zero external field, already ^{4}He temperatures are sufficient to fulfill the criterion of higher level splitting than the thermal energy. In contrast, for $S = 1/2$ systems static magnetic fields of several

Tesla would be required to reach this splitting.

One of the greatest obstacles in building a quantum computer is controlling decoherence. For quantum computational applications the needed coherence times have to be defined. If the coupling to the environment is too strong, coherence times are too short to be accessed with appropriate techniques. Therefore the measurement technique and the timescale in which the technique allows to determine coherence times is crucial for both preliminary investigations and potential applications. The error rate of a quantum computer is typically proportional to the ratio of manipulation time to decoherence time, therefore it is desirable to complete a computation much more quickly than the decoherence time.

Pulsed magnetic resonance is a well-suited tool for manipulating quantum spin systems such as electron and nuclear spins. This technique employs microwave pulses with the exact energy splitting of the level separation. Typical pulse lengths to invert the population in a two level electron spin system (π-pulse) are in the order of 10 ns, depending on the used frequency. From resonant phonon absorption in Cr_7Ni, coherence times were thought to be smaller than 10 ns [6]. It would not be possible to fulfill the criterion to complete a computation much more quickly than the decoherence time with the mentioned values. Therefore the direct observation and quantification of coherence in molecular magnets is crucial to assess the suitability of molecular magnets for quantum computation. Direct access to coherence times by other means than pulsed ESR remains unsuccessful to date. Several studies showing the superposition of states were performed on molecular magnets. One study by del Barco *et al.* presents measurements combining microwave spectroscopy with high sensitivity magnetic measurements [7] on the SMM Ni_4. They monitor the energy splitting of low lying magnetic states dependent on transverse magnetic field. Only an lower bound on decoherence times ($T_2 > 0.8$ ns) could be given from absorption linewidts. Keren *et al.* determined dephasing times of several isotropic molecular magnets with different spin values using muon spin relaxation measurements [8]. The dephasing times were found to be independent on S and in the order of 10 ns.

Long living quantum coherence can also be shown by quantum oscillations, sometimes called Rabi oscillations. In this experiment, the magnetization is rotated by an arbitrary angle around the x- or y-axis (in the Bloch sphere picture) by an oscillatory driving field. This turning by an arbitrary angle is a prerequisite for potential quantum information applications. If then a sinusoidal behavior of the S_z magnetization is observed, it is proven that quantum oscillations can be distinctively induced.

Chapter 2

Introduction to Electron Spin Resonance

Abstract. In this chapter, we describe the experimental technique of Electron Spin Resonance, because it is the experimental method most used in this work. First, we discuss the basics of both CW and pulsed ESR. Because as a part of the thesis, a unique ESR spectrometer was built (Chapter 3), we present an overview of different experimental approaches, both commonly used and special ones.

2.1 Principles

The experimental technique of Electron Spin Resonance (ESR) is widely used in biology, chemistry, medicine and physics to study systems that have one or more unpaired electrons. In Chapter 1.2 we introduced the spin Hamiltonian associated with an exchange-coupled system with magnetic anisotropy. Here, we will first consider an uncoupled electron in constant applied magnetic field (Zeeman interaction):

$$H_{\text{Zeeman}} = g\mu_B B_0 S_z \tag{2.1}$$

Here, B_0 is the external magnetic field applied in direction of the z-axis, g is the Landé factor (gyromagnetic ratio), μ_B is the Bohr magneton and S_z is the z operator of the electron spin (see equation 2.3). We denote the spin as being spin-up, when its projection on the z-axis is parallel to the magnetic field, and spin-down when it is antiparallel to B_0. We can calculate the energy of each of the orientation of the spins using the states $|\frac{1}{2}\rangle$ and $|-\frac{1}{2}\rangle$:

$$\langle \pm\frac{1}{2}|H|\pm\frac{1}{2}\rangle = g\mu_B B_0 \langle \pm\frac{1}{2}|S_z|\pm\frac{1}{2}\rangle = \pm\frac{1}{2} g\mu_B B_0 = \pm\frac{1}{2}\hbar\omega_0, \tag{2.2}$$

where ω_0 is the Larmor frequency. The basic phenomenon in ESR is the absorption of a photon with the energy $E = \hbar\omega_0$ by a spin in the $|-\frac{1}{2}\rangle$ state. Normally, the ESR experiment is performed by keeping the microwave frequency constant

Table 2.1: Letter designation of the microwave band, as defined by the Radio Society of Great Britain, the corresponding frequency range, the typical ESR frequency in the band and the resonance field for a free electron.

Band	Frequency range	ESR frequency	Resonance field
L	1-2 GHz	2 GHz	0.07 T
X	8-12 GHz	9.5 GHz	0.26 T
Q	30-50 GHz	34 GHz	1.21 T
W	75-110 GHz	94 GHz	3.36 T

and sweeping the applied magnetic field. This experiment is called continuous wave (CW) ESR. The energy of the resonance transition is the microwave region (1 GHz to about 300 GHz). Historically, different microwave frequency bands were defined. For each of these bands microwave equipment was developed, so that many microwave components only work in these bands. Table 2.1 shows the microwave bands commonly used in ESR, the frequency of the setups and the magnetic field where resonance conditions for a free electron spin are matched.

2.2 Pulsed ESR

Pulsed ESR is a very versatile and powerful technique. Unlike in nuclear magnetic resonance (NMR), pulsed techniques are not that common in ESR. Pulsed ESR in its most basic form involves applying a short microwave pulse, and then to measure the emitted microwave signal created by the sample magnetization. The Fourier transformation of the microwave signal leads to the ESR spectrum in the frequency domain [9]. Nowadays it is possible to apply a whole variety of pulse sequences, which reveal comprehensive structural and dynamical properties of paramagnetic compounds. For example, it enables the elucidation of interactions of the electron spin with the surrounding nuclear spins using ESEEM or pulsed ENDOR techniques. Moreover, it is possible to quantify coherence times, even if the lines are inhomogeneously broadened and therefore this information cannot be extracted from CW measurements.

In the following, we will show a mathematical description of the evolution of a spin system under microwave pulses, and then apply this framework to pulsed methods which were used in Chapter 4 and Chapter 6. The nomenclature of a

pulse sequence is as follows and will be used throughout the whole thesis: $\pi/2 - \tau - \pi - \tau -$ echo means that a $\pi/2$ pulse is followed by a variable time delay τ, then by a π-pulse, the same variable time delay τ after which the echo is recorded.

2.2.1 Density Operator and Product Operator Formalism

To be able to mathematically describe the evolution of a spin system under manipulation with coherent electromagnetic radiation, we will give a short introduction to the density operator and product operator formalism.
We will describe a two-level system with the two eigenstates $|0\rangle$ and $|1\rangle$. A superposition of these states is given by

$$|\psi\rangle = c_0(t)|0\rangle + c_1(t)|1\rangle,$$

where $c_0(t)$ and $c_1(t)$ denote normalized ($|c_o|^2 + |c_1|^2 = 1$) complex coefficients. The density matrix ρ_ψ is given by

$$\rho_\psi = |\psi\rangle\langle\psi| = \begin{pmatrix} |c_o|^2 & c_0 c_1^* \\ c_1 c_0^* & |c_1|^2 \end{pmatrix},$$

where c_0^* denotes the complex conjugate of c_0. For the states $|0\rangle$ and $|1\rangle$, the density matrix can be written as follows:

$$|0\rangle : \ \rho_0 = \begin{pmatrix} 1 & 0 \\ 0 & 0 \end{pmatrix}, \ |1\rangle : \ \rho_1 = \begin{pmatrix} 0 & 0 \\ 0 & 1 \end{pmatrix}$$

One can see that the diagonal elements in the density matrix describe the probability to find a system in its eigenstates. The off-diagonal elements describe the coherences. Coherences is the expression commonly used in ESR to describe superposition states. Therefore, the time taken for off-diagonal components of the density matrix to effectively vanish is the decoherence time.

For a $S = 1/2$ system, the electron spin operators are the Pauli matrices

$$\hat{S}_x = \frac{1}{2}\begin{pmatrix} 0 & 1 \\ 1 & 0 \end{pmatrix}, \ \hat{S}_y = \frac{1}{2}\begin{pmatrix} 0 & -\mathrm{i} \\ -\mathrm{i} & 0 \end{pmatrix} \text{ and } \hat{S}_z = \frac{1}{2}\begin{pmatrix} 1 & 0 \\ 0 & -1 \end{pmatrix}. \tag{2.3}$$

The time dependence of the density matrix under a Hamiltonian $H(t)$ is described with the Liouville-von Neumann equation [9]:

$$\frac{d\rho(t)}{dt} = -\frac{\mathrm{i}}{\hbar}\left[H(t), \rho(t)\right] \tag{2.4}$$

Here [,] are the commutator brackets, where $[A, B] = AB - BA$. In the case of the Cartesian spin operators the commutators are $[S_x, S_y] = iS_z$, $[S_y, S_z] = iS_x$ and $[S_z, S_x] = iS_y$.

In the product operator formalism we describe the time evolution of the system with ρ decomposed into a linear combination of orthogonal basis operators, called product operators. This method has the advantage, that each of the basis operators has a certain physical meaning; so interpretation is easy. Because the levels in high-spin systems with zero-field splitting are no longer equally spaced a specific microwave excitation of one transition is possible. In this case a simpler description of the system using a so called fictitious or effective spin-1/2 operator formalism can be used [27] [28].

For a time-independent Hamiltionan, one can solve the Liouville-von Neumann equation for a product operator A evolving under another product operator B:

$$e^{-\mathrm{i}\Phi B/\hbar} A e^{\mathrm{i}\Phi B/\hbar} = C \tag{2.5}$$

In a shorthand notation [9]:

$$A \xrightarrow{\Phi B} C$$

A general solution of Equation 2.5 is [9]:

$$A \xrightarrow{\Phi B} A\cos\Phi - \mathrm{i}\,[B, A]\sin\Phi \text{ for } B \neq A \text{ and } A \xrightarrow{\Phi B} A \text{ for } B = A \tag{2.6}$$

.

2.2.2 Electron Spin Echo

A $\pi/2$ pulse along the x-axis rotates the equilibrium magnetization from the z to the $+y$ axis (Fig. 2.1): $-S_z \xrightarrow{\pi/2\, S_x} S_y \sin(\pi/2) = S_y$. In any real system there are local inhomogeneities, which cause a dephasing of the magnetization in the x-y plane. We can recover (or refocus) the magnetization by applying an additional π pulse after a time τ measured from the first pulse. Then the magnetization is refocused at the time 2τ. After this time, the echo intensity is determined by recording the echo area in a certain time span.

Introducing decoherence, the signal decays proportional to $e^{(-t/T_2^*)}$ in time. We would like to emphasize the difference in between dephasing, where the magnetization can be recovered, and decoherence, which is an intrinsic effect of the system, where the phase information is lost and cannot be refocused.

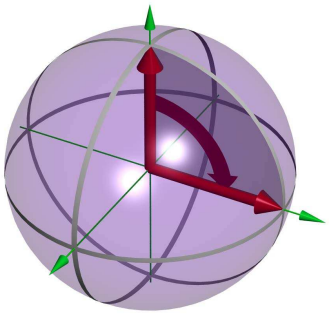

Figure 2.1: Rotation of the equilibrium magnetization under the application of a $(\pi/2)_x$ pulse on the Bloch sphere.

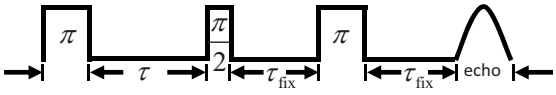

Figure 2.2: Inversion recovery pulse sequence.

To obtain a quantitative picture of the Hahn echo experiment, we assume a narrow-line case (the linewidth of the transition is narrower than the excitation linewidth) and neglect relaxation. Using the product operator formalism we obtain after a time delay t after the second pulse (Ω_S is the frequency offset due to local inhomogeneities) [9]:

$$\begin{aligned} -S_z &\xrightarrow{-\frac{\pi}{2}S_x} -S_y \\ &\xrightarrow{\Omega_S \tau S_z} S_y \cos(\Omega_S \tau) - S_x \sin(\Omega_S \tau) \\ &\xrightarrow{\pi S_z} -S_y \cos(\Omega_S \tau) - S_x \sin(\Omega_S \tau) \\ &\xrightarrow{\Omega_S t S_z} S_x \sin(\Omega_S (t-\tau)) - S_y \cos(\Omega_S (t-\tau)) \end{aligned}$$

In the case of a symmetric line being excited in the center, only the cos term would lead to an echo intensity, because the cosine function is even.

2.2.3 Relaxation

If the magnetic quantum number m_S of the spin system changes, this is called longitudinal spin relaxation (see also Chapter 1.5). To determine the longitudinal relaxation, an inversion recovery sequence can be used Fig. 2.2. In this sequence, a π pulse inverts the polarization. Using a Hahn echo with a fixed delay time τ_{fix}, one can detect the longitudinal magnetization after a variable time delay

τ between inversion and detecting pulses. The recovery of the magnetization (that means the relaxation) is described by a function $1 - e^{-\tau/T_1}$, where T_1 is the longitudinal relaxation time.

2.2.4 ESEEM Spectroscopy

Electron Spin Echo Envelope Modulation (ESEEM) is a technique in pulsed ESR to measure hyperfine and quadrupole interactions between the electron spin and neighboring nuclear spins. It is particularly powerful if hyperfine couplings cannot be resolved in ESR spectra.

The non-selective $(\pi/2)_x$ pulse (a non-selective pulse is a pulse which excites all transitions of a spin system) of a Hahn echo sequence excites coherence on all transitions to hyperfine-split levels, also to the forbidden ones. The echoes refocus at different places in the $x-y$-plane, if the coherence is refocused on a transition different to the one on which it was defocused. Along the observation direction y the intensity of the coherence-transfer echoes is modulated. This modulation is the origin of the modulation of the total echo amplitude.

To determine the quantitative behavior of this modulation, we will calculate the amplitude of the transverse magnetization (and therefore the echo amplitude) for a $S = 1/2$ and $I = 1/2$ system [9] after a two-pulse echo sequence (see Chapter 2.2.2).
The Hamiltonian in its eigenbasis for a small isotropic hyperfine coupling with the constant a_{iso} and the nuclear Zeeman frequency $\omega_I = -g_n\beta_n B_0/\hbar$ is given by

$$H_0 = \Omega_S S_z + \omega_I I_z + a_{\text{iso}} S_z I_z.$$

Because in the cartesian product basis it is not easy to calculate the free evolution under this Hamiltonian, we transform the density matrix using the unitary transformation $U_1 = \exp(-\mathrm{i}(\xi I_y + \eta 2 S_z I_y))$, where ξ and η depend on different components of the hyperfine coupling tensor ([9], p. 60). After calculating the series of transformations $-S_z \xrightarrow{\pi/2 S_x} \xrightarrow{A} \xrightarrow{H_0\tau} \xrightarrow{-A} \xrightarrow{\pi S_x} \xrightarrow{A} \xrightarrow{H_0\tau} \xrightarrow{-A} S_{echo}$, the following modulation depth $V(\tau)$ of the echo intensity is obtained [9]:

$$V(\tau) = \left\langle -S_{echo_y} \right\rangle \tag{2.7}$$

$$= 1 - \frac{k}{4}\left[2 - 2\cos\left(\omega_I + \frac{a_{\text{iso}}}{2}\right) - 2\cos\left(\omega_I - \frac{a_{\text{iso}}}{2}\right) + \cos\left(a_{\text{iso}}\tau\right) + \cos\left(2\omega_I\right)\right] \tag{2.8}$$

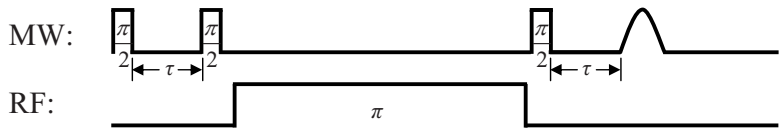

Figure 2.3: Mims-ENDOR pulse sequence. All pulse delays are fixed and the RF frequency is varied.

In this equation k is the modulation depth parameter. We observe a modulation with the frequencies of the coupled nuclear spins, additionally the sum and difference of these frequencies are observed. If several nuclei are coupled to the electron spin, the resulting modulation V_{res} is

$$V_{res}(\tau) = \prod V_i(\tau),$$

where V_i are the modulations of the individual nuclei. The equation is an expression of the fact that interactions between the single nuclei can be neglected.

2.2.5 ENDOR of $S = 1/2$, $I = 1/2$ Spin Systems

Electron **n**uclear **do**uble **r**esonance (ENDOR) is another magnetic resonance technique to determine nuclear transition frequencies in paramagnetic compounds.

ENDOR is a technique which is often applied as a CW method. Here, an ESR transition is partially saturated by applying a microwave field; a second radiation field in the energy range of nuclear transition frequencies (radio frequency, RF) induces nuclear transitions. Observing the desaturation of the ESR transition as a function of the radio frequency allows to determine the nuclear transition frequencies.

Due to low RF duty cycles, thermal heating is a smaller problem in pulsed ENDOR compared to CW ENDOR. In some cases, it is also possible to excite only a selection of spins, dependent on their hyperfine coupling and relaxation times. There are two common pulse sequences in pulsed ENDOR: Davies ENDOR and Mims ENDOR. Because in the experiment (Chapter 4.3.3) Davies ENDOR showed an lower relative ENDOR intensity, we will only present the basics of Mims ENDOR in the following.

In Mims ENDOR (Fig. 2.3), the preparation sequence $\pi/2 - \tau - \pi/2$ creates a z-polarization which shows a τ-dependent oscillation in time. In the following period, the polarization is changed by an RF pulse. Subsequently, a stimulated Echo is induced by a third $\pi/2$-pulse, the echo is then recorded as a function of

the RF frequency. For a $S = 1/2$ and $I = 1/2$ system the spin Hamiltonian is $H_0 = \omega_S S_z + \omega_I I_z + a_{iso} S_z I_z$. Here ω_S and ω_I are the electron and nuclear spin Larmor frequencies and a_{iso} is the isotropic hyperfine interaction. The density matrix after a pulse sequence with an arbitrary RF flip angle α reads [9]:

$$-S_z \xrightarrow{\pi/2 S_x} \xrightarrow{H_0\tau} \xrightarrow{\pi/2 S_x} \xrightarrow{\alpha I_z} \xrightarrow{\pi/2 S_x} \xrightarrow{H_0\tau} \tag{2.9}$$

$$- \left[\cos^2(\Omega_S\tau)\cos^2(\frac{a_{\text{iso}}}{2}\tau) + \frac{1}{2}\sin^2(\Omega_S\tau)\sin^2(\frac{a_{\text{iso}}}{2}\tau)(1+\cos\alpha)\right] S_y \tag{2.10}$$

Assuming the maximum polarization transfer by the RF pulse (length π) we can integrate over the $\cos^2$ functions and obtain as a resulting echo amplitude [9]:

$$V_{echo} = \frac{1}{4}(1 - \cos(a_{\text{iso}}\tau))$$

Considering the change in ENDOR intensity induced by the RF pulse V_{echo}, one can see that for $\tau = \frac{2n\pi}{a_{\text{iso}}}$ $(n = 0, 1, 2, ...)$ the echo intensity is not changed, that means we observe blind spots in the spectrum. Therefore minima in the change in ENDOR intensity have to be checked carefully, whether they are not due to the blind spot behavior. This check can be performed for example by adding several spectra recorded with different τ.

ENDOR and ESEEM are both techniques which reveal electron nuclear couplings, but have different application areas. ESEEM is a technique which is mostly used for ESR at lower frequencies, as the modulation depth is $\propto B_0^{-2}$, and B_0 scales with the ESR frequency (for non-zero field split compounds). In pulse ENDOR, the signal intensity increases approximately linearly with the ENDOR frequency. Therefore, at high fields (e.g. W-Band ESR at 94 GHz) ENDOR is the most suitable method to determine nuclear couplings, if relaxation and coherence times are sufficiently long. For zero-split systems which the consequential observation of transitions at lower B_0, even in high frequency experiments sufficient modulation depth in ESEEM experiments can be observed (see Chapter 6.3.1).

To determine the expected energy spectrum in an ENDOR experiment we will analyze the allowed RF transitions. Fig. 2.4 shows the energy level diagram for a $S = 1/2$ electron spin coupled to one magnetic nucleus ($I = 1/2$). The external magnetic field splits the electron spin levels, the position of the nuclear sublevels is influenced by the Zeeman splitting plus the hyperfine interaction between electron and nucleus. With the selection rules for NMR transitions, $\Delta m_I = \pm 1$ and $\Delta m_S = 0$, the ENDOR frequencies are found at $f_{\text{ENDOR}} = |\omega_I \pm a_{\text{iso}}/2|$. In the high-field limit, that means for $\omega_I > |a/2|$, two signals appear in the ENDOR

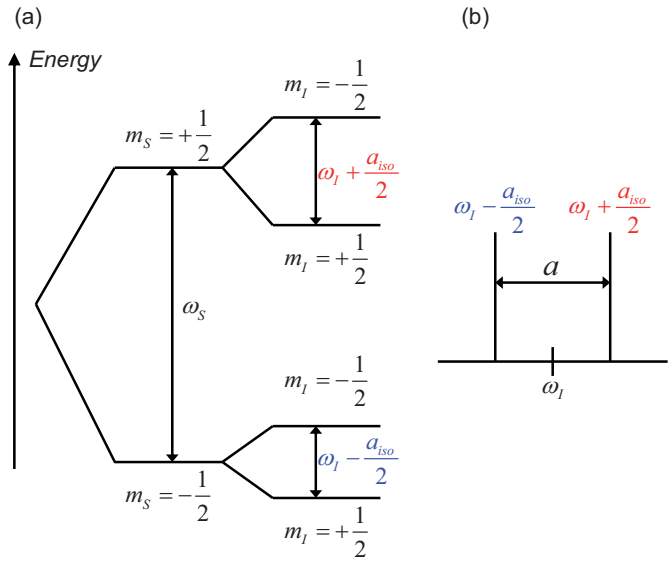

Figure 2.4: (a) Energy level diagram of an $S = 1/2$ electron spin coupled to a single $I = 1/2$ nuclear spin in the high field approximation. ω_S is the electron Larmor frequency, whereas ω_I is the nuclear Larmor frequency. (b) Expected ENDOR spectrum.

spectrum, centered about the free Larmor frequency ω_I and separated by the isotropic hyperfine coupling constant a_{iso}.

2.2.6 Rabi Oscillations

Rabi oscillations are the cyclic behavior of a two-level quantum system in the presence of an oscillatory driving field. Without a driving field the Hamiltonian is [21]

$$\hat{H}_0 = E_0|0\rangle\langle 0| + E_1|1\rangle\langle 1|,$$

where E_0 and E_1 are the energies of the corresponding eigenstates. With an external oscillatory driving field in resonance, the Hamiltonian writes

$$\hat{H} = \hat{H}_0 + \frac{\omega_{\text{Rabi}}}{2} e^{\mathrm{i}\omega_{\text{Rabi}}t}|0\rangle\langle 1| + \frac{\omega_{\text{Rabi}}}{2} e^{-\mathrm{i}\omega_{\text{Rabi}}t}|1\rangle\langle 0|.$$

Assuming the spin being present in the ground state $|0\rangle$ in the beginning, the probability $|c_1(t)|^2$ that it can be found in the state $|1\rangle$ after the time t is

$$|c_1(t)|^2 = \frac{1}{2}(1 - \cos(\omega_{\text{Rabi}}t)).$$

Table 2.2: Phase cycling for pulse sequence used to detect Rabi oscillations.

Cycle	Pulse	Pulse Phase	Detection
1	a	$+x$	$+x$
2	a	$-x$	$-x$

The spin system shows cyclic behavior with the Rabi frequency ω_{Rabi}.
In ESR this phenomenon is also called transient nutation. For a $S = 1/2$ system the Rabi frequency is [9]

$$\omega_{\text{Rabi}} = \frac{g_1 \mu_B B_1}{\hbar},$$

where g_1 is the g-value in the x-axis of the laboratory frame and B_1 is the magnetic field strength of the microwave field.
The dependence of the matrix elements of S_x and S_y on spin quantum number leads to a different transition amplitude in a high-spin system [9], dependent on which transition is excited. The Rabi frequency of the transition from the magnetic sublevel m_S to $m_S + 1$ is

$$\omega_{\text{Rabi}}(m_S, m_S + 1) = \frac{g_1 \mu_B B_1}{\hbar} \sqrt{S(S+1) - m_S(m_S+1)}.$$

In ESR, different methods to detect Rabi oscillations are known ([9], Chapter 14.2). Here we will calculate coherences detected with the pulse sequence $a - \tau_{\text{fix}} - \pi -$ echo with the phase cycling given in Table 2.2; this pulse sequence was used in the experiments shown in Chapter 6.3.3. We use the product operator formalism for a fictitious $S = 1/2$ system, because we excite only one transition of the spin multiplet. Please note that this is a calculation for the simpler narrow line case. Ω_S is the frequency offset due to local inhomogeneities.

$$\begin{aligned}
-S_z &\xrightarrow{aS_x} S_y \sin a - S_z \cos a \\
&\xrightarrow{\Omega_S \tau_{\text{fix}} S_z} -S_x \sin a \sin(\Omega_S \tau_{\text{fix}}) + S_y \sin a \cos(\Omega_S \tau_{\text{fix}}) - S_z \cos a \\
&\xrightarrow{\pi S_x} -S_x \sin a \sin(\Omega_S \tau_{\text{fix}}) - S_y \sin a \cos(\Omega_S \tau_{\text{fix}}) + S_z \cos a \\
&\xrightarrow{\Omega_S t S_z} S_x \sin a \sin(\Omega_S (t - \tau_{\text{fix}})) - S_y \sin a \cos(\Omega_S (t - \tau_{\text{fix}})) + S_z \cos a
\end{aligned}$$

In analogy with the inverted phase of the first pulse we obtain:

$$-S_z \xrightarrow{-aS_x} \xrightarrow{\Omega_S \tau_{\text{fix}} S_z} \xrightarrow{\pi S_x} \xrightarrow{\Omega_S t S_z}$$
$$- S_x \sin a \sin\left(\Omega_S(t-\tau_{\text{fix}})\right) + S_y \sin a \cos\left(\Omega_S(t-\tau_{\text{fix}})\right) + S_z \cos a$$

Subtracting the signal of the two cycles leads to

$$2S_x \sin a \sin\left(\Omega_S(t-\tau_{\text{fix}})\right) - 2S_y \sin a \cos\left(\Omega_S(t-\tau_{\text{fix}})\right).$$

Integrating the signal around the time $t = \tau_{\text{fix}}$, only the S_y-term leads to an echo signal, because the cos function is even and $\Omega_S(t-\tau_{\text{fix}}) \ll \pi$. In summary, we detect the cyclic, sinusoidal dependence on $\sin a$ of the nutation of the magnetization, which are Rabi oscillations. Because it is only possible to obtain an echo in the $x-y$-plane, the observed signal is phase shifted by $\pi/2$ compared to the conventional presentation of Rabi oscillations, where the S_z expectation value is plotted. Nevertheless the frequency of the oscillations remains unchanged.

2.3 Commonly Used ESR Spectrometers

2.3.1 Fixed Frequency Setups

Most setups built during the about 60 year-long history of ESR are fixed-frequency setups. This means, that except for a small frequency tuning range of the resonator, only one frequency is accessible with one setup (see also Table 2.1). Thus, it it possible to use tailored microwave components which are only suitable in narrow frequency ranges. In this section, we will only discuss similarities of common ESR spectrometers, due to the plentifulness of details we refer the reader the monograph from Poole [29].

A cavity is a simple metal box, usually of cylindrical or rectangular shape, but sometimes also more complex geometries were chosen. Standing electromagnetic waves store the energy coupled into the cavity. The ratio of the stored energy compared to the energy dissipated per microwave period gives the Q-factor of a cavity:

$$Q = \frac{2\pi(\text{energy stored in cavity})}{\text{energy dissipated per cycle}} = \frac{f_0}{\text{FWHM}}$$

The second expression relates the Q-factor with the resonance frequency f_0 and the full width at half maximum of the resonance, FWHM. High Q-factors indicate low relative losses, and provide higher electromagnetic fields B_1, which increases

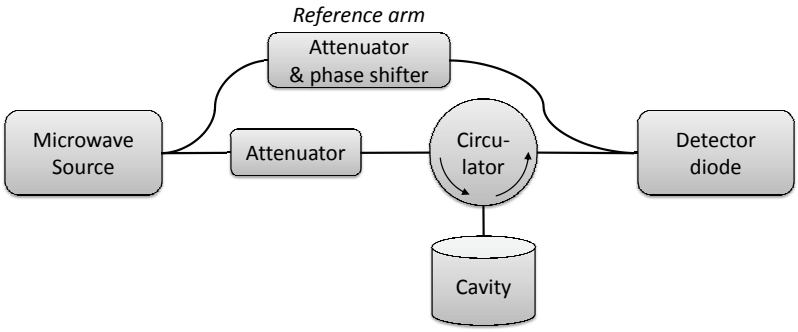

Figure 2.5: Principle hardware configuration of a CW ESR spectrometer. Shown are the main microwave components.

the sensitivity of the spectrometer. Mechanisms responsible for losses will be discussed in Chapter 3.2.2. Microwaves are coupled into the cavity using coupling holes and adjustable iris screws allow to vary the strength of the coupling.

Fig. 2.5 shows the general layout of an ESR spectrometer: A microwave source, typically a Gunn diode, generates the microwave radiation. Because the power of these sources cannot be varied easily over orders of magnitude, an attenuator makes it possible to precisely control the power. The circulator will now direct microwaves coming from the source into the cavity. Signals coming back from the cavity will be directed to the detector. The use of the circulator is necessary, because the cavity works in reflection mode. That means, that the reflected signal of the cavity dependent on magnetic field is measured. If the cavity is critically coupled, out of resonance no microwave radiation is reflected. A resonant absorption in the sample changes the impedance of the cavity, and microwaves will be reflected and detected by a detector diode. To keep the diode at its working point, it is fed with additional microwave power with the correct phase for constructive interference from the resonance arm. Normally, the static magnetic field is modulated using modulation coils, which enables a lock-in detection.

2.3.2 Multi-Frequency and Broadband Setups

If several distinct frequencies from a broad range can be accessed, we talk about multi-frequency setups. This principle was applied for example by Takahashi *et al.* [30], by using the different modes of a cylindrical cavity. The cavity used by this group accesses a frequency rage of about 50 GHz to 350 GHz. The microwaves

are fed into the cryostat using cylindrical waveguides, the transmission signal is recorded using a millimeter-wave vector network analyzer.

Broadband ESR or microwave spectroscopy, that means a setup which is able to detect small absorptions at any frequency in a broad range at cryogenic temperatures, is a technique which is not commercially available yet. Thus, only specific setups, which were normally developed to study a certain class of materials, will be described in the following.

With a bolometric technique [31] it is possible to detect microwave absorption using an in-situ normal metal reference sample that calibrates the absolute microwave field strength. This is accomplished by positioning both the sample under test and the reference sample on equivalent spots, in respect to the spatial distribution of electromagnetic fields. The absorption is detected via the heating of the temperature sensor being thermally coupled to the sample. This is in contrast to all other methods presented here, where the reflected or transmitted microwave signal is used for detection. With this technique, also field-swept ESR measurements can be performed. The frequency of this setup is limited by the waveguides, because both sample and normal reference sample are placed in the waveguide.

To study metallic wire samples, Mahdjour *et al.* [32] designed a coil with μm dimensions, which is driven by a microwave generator in the frequency range between 0.1 and 8.5 GHz. Both frequency-domain and field-domain studies are reported. For small sample sizes the setup showed higher sensitivity compared to a conventional cavity spectrometer.

For thin film samples, measurements with microwave striplines are advantageous: In a frequency range, of 0.1-40 GHz, Goglio *et al.* [33] measured ferromagnetic resonance of a thin film sample being a part of the stripline. Absorption in the sample then changes the transmission properties of the line.

For conducting samples, a broadband spectrometer in corbino geometry was successfully used [34] [35] [36]: Here, the flat sample terminates a coaxial transmission line. The complex reflection coefficient is measured using a vector network analyzer. From the reflection coefficient it is possible to calculate the impedance of the sample and the complex conductivity. To correct for the strong influence of the transmission line itself, a three standard calibration has to be performed. This requires a high reproducibility of the cryogenic conditions, because the properties of the transmission lines are strongly temperature dependent. In principle, this technique allows for measurements at a frequency range of 45 MHz up to 40 GHz. Up to now, measurements in an external magnetic field using this technique were

not reported. For nonconducting samples, the surface impedance approach used for analysis of the data fails, and a solution for the field distribution inside the sample has to be used [37].

2.3.3 Frequency Domain Magnetic Resonance Spectroscopy

Frequency Domain Magnetic Resonance Spectroscopy (FDMRS) is a magnetic resonance technique referring the magnetic resonance spectroscopy, performed by sweeping the frequency and keeping the magnetic field constant [38]. The setup works in a quasi-optical design, that means no waveguides or cables are used to guide the radiation. This is then a far-field technique, in contrast to all other techniques presented in Chapter 2.3.2, which are near-field setups. Because in the microwave region, the wavelength of the radiation is comparable to the sample size, diffraction will dominate the transmission signal in a quasi-optical geometry. Thus, the accessible frequencies are in the range from 1-40 cm^{-1} (30-1200 GHz), also given by the continuously tunable sources available in this range, which are backward-wave oscillators (BWOs). A BWO is a vacuum tube, in which a cathode generates an electron beam, which passes over a comb-like fine metallic structure. Here, electric fields lead to an acceleration and deceleration generating an electromagnetic wave. This wave shows a group velocity directed opposite to the propagation direction of the electrons. The radiation is coupled out through oversized waveguides.

The BWOs of the FDMRS spectrometer are frequency modulated. This modulation is realized by wobbling the high voltage of the power supply energizing the BWO. A consequence of this method to reduce standing waves can be the broadening of absorption lines, if the modulation frequency is larger than the linewidth. In the experiment the modulation voltage was gradually decreased until no change in lineshape could be observed any more.

2.4 Bruker W-Band Spectrometer

In this section, we present the ESR spectrometer Bruker ELEXSYS E680 [39] used for the measurements in Chapter 4 and Chapter 6. The most important parts of the spectrometer are the W-band resonator, the magnet system, the W-band bridge, the IF-bridge, the ELEXSYS console with the acquisition server and the front-end workstation. The spectrometer works according to a inter-

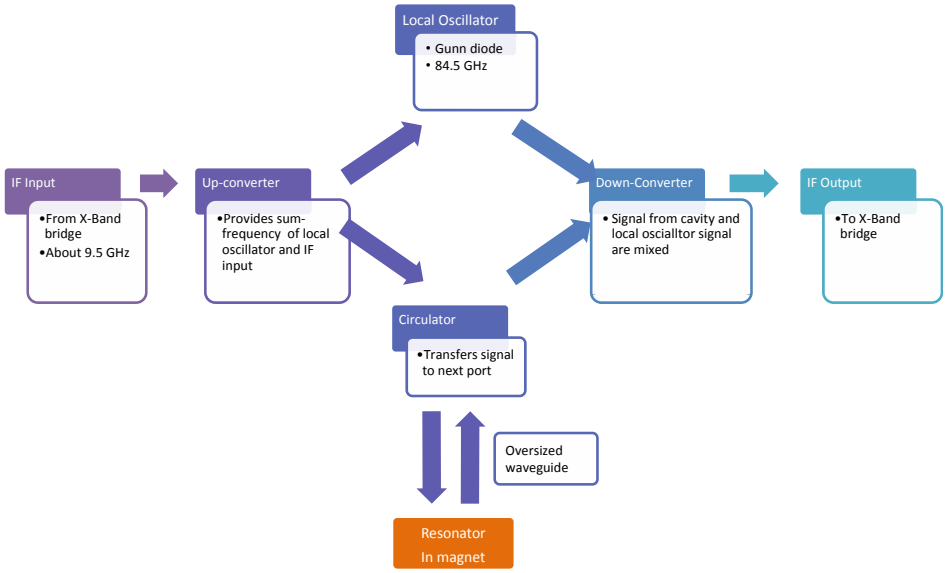

Figure 2.6: Intermediate frequency concept: Schematics of the W-Band bridge.

mediate frequency concept, as shown in Fig. 2.6. In this concept, a standard X-Band (9.5 GHz) bridge performs all functions necessary for ESR, whereas an up-converter in the W-Band bridge using a local oscillator frequency at 84.5 GHz generates the electron-spin resonance frequency of 94 GHz. This radiation is transmitted through a circulator and an oversized waveguide to the cavity. The signal from the cavity then is transmitted through the circulator into the down-converter, where the IF signal (9.5 GHz) is generated using the signal from the local oscillator (84.5 GHz). The advantage of this concept is the easy implementation from functions which are already available from X-Band spectrometers, like pulse shaping at different phases and frequencies.

W-Band bridge. The W-Band bridge consists of the microwave source, the up-converter and the down-converter. The microwave source is a Gunn diode with a frequency of 84.5 GHz with a high phase stability. The up-converter, which generates the operating W-Band frequency (94 GHz) from the Gunn diode mm-wave and the IF signal, also generates the lower frequency. This then is strongly suppressed by the microwave components and waveguides used.

IF bridge. The intermediate frequency bridge provides all main functions of an ESR spectrometer, like power control, reference arm phase adjustment and automatic frequency control.

W-Band resonator. The spectrometer employs a cylindrical resonator (dimensions: ≈ 3 mm) in the TE_{011} mode. Samples are brought into the geometrical center of the cavity using a 0.9 mm outer diameter quartz tube. The probehead is equipped with an ENDOR coil. The RF circuit is broadband, and covers the frequency range of 20-200 MHz, whereas the RF microwave field strength is lower at the lower and higher end of this field range.

Magnet system. For a free electron with $g = 2$, the resonance field at 94 GHz is 3.36 T. Because in ESR the magnetic field is swept, and most species have a resonance close to $g = 2$, the magnet system Bruker-Magnex Hybrid[3] consists of a superconducting main magnet (up to 6 T) and a water-cooled resistive magnet for small field sweeps (700 G). For all measurements presented in this thesis only the superconducting magnet was used, due to the wide spectra observed. The maximum field sweep speed of the superconducting magnet is 6 T/h, but

is strongly reduced above 4.5 T. The persistent switch of the superconducting magnet causes a large hysteresis, especially at the beginning of a field scan. In this case, the current doesn't path only through the magnet, but a significant current is flowing through the resistive switch due to the large magnet inductance. This effect is taken into account by the XEPR software, except for the measurements in pulsed mode.

Chapter 3

Tunable Cavity Setup

Abstract. In this chapter, we describe the broadband cavity ESR setup, which was designed and built as part of this thesis, and show measurements carried out with the setup. First, we will discuss design criteria, which were considered while building this setup. The final assembly consists (Fig. 3.1) of a microwave cavity incorporated in a ^{4}He cryostat with a 10 T superconducting magnet. We are able to perform field-dependent microwave absorption measurements from 14–40 GHz, by varying the cavity height in-situ. The insertion of dielectrics into the cavity allows us to perform measurements down to frequencies of 5 GHz. The microwave generation, waveguide and detection system are unusual for ESR measurements. This opens up a wide range of new applications. A vector network analyzer with a principal frequency range of 45 MHz–40 GHz, and semi-rigid coaxial cables with a cutoff frequency of 64 GHz enable broad band measurements. We present empty cavity test measurements and magnetic resonance test measurements using a transition metal system. Moreover, we present preliminary studies of a level crossing in V_{15}, an $S = 1/2$ molecular magnet.

3.1 Introduction

Studying spin systems close to a level anticrossing (Fig. 3.2) is very interesting, because it is possible to investigate quantum effects, such as the mixing of spin states: At the field, where the two spin states $|M_S\rangle$ and $|M'_S\rangle$ would become degenerate in the case of a real crossing, the degeneracy can be lifted by a suitable type of interaction, and the eigenstates of the system are the symmetric and antisymmetric superpositions of the two spin states $1/2(|M_S\rangle + |M'_S\rangle)$ and $1/2(|M_S\rangle - |M'_S\rangle)$, which are separated by the splitting energy Δ. These superposition states have attracted recent interest, because they are necessary to perform quantum computation operations [22]. The quantum superposition in the case of

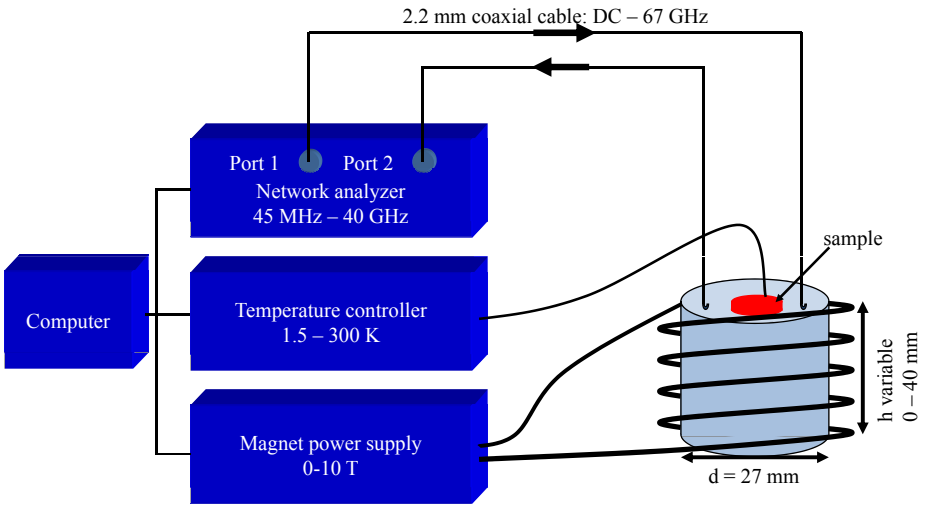

Figure 3.1: Schematic drawing of the principal components of the tunable cavity setup. The network analyzer, the temperature controller of the cryostat and the magnet power supply are controlled by a computer.

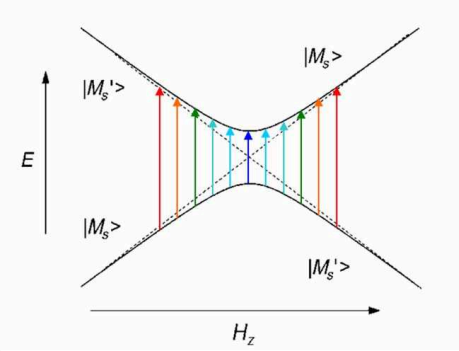

Figure 3.2: Energy level diagram of an avoided level crossing. The arrows indicate induced transitions with different, fixed frequencies. The transitions occur at different fields, dependent on the topology of the avoided crossing.

an avoided level crossing is an intrinsic property of the system in an external magnetic field, the superposition state does not have to be prepared. Examining the topography of the spin levels close to the crossing field, enables quantification of the mixing interactions, and to investigate if an anticrossing with the subsequent superposition of states is present.

The level separation of an avoided crossing in a molecular magnet due to antisymmetric exchange interactions dependent on the external magnetic field was not studied so far. In general, different techniques to experimentally study level crossings are available: Inelastic neutron scattering (INS) allows to observe the energy of magnetic transitions, and is not limited by the selection rule $\Delta S = \pm 0$ like ESR. Thus, it proved possible to observe transitions between superposition states [40] in the antiferromagnetic molecular cluster $CsFe_8$. INS remains challenging due to the large amounts of sample needed. In specific heat measurements [41], there are indications for induced tunnel splittings by a transverse external magnetic field. Del Barco *et al.* [7] studied the magnetic resonance absorption at different frequencies of the single-molecule magnet Ni_4 with a hall sensor. The longitudinal field was varied while a fixed transverse field was applied. Close to zero longitudinal field, the absorption shape shows the signature of quantum superposition states with a splitting dependent on the transverse field. In muon spin resonance (μSR, sometimes also called muon spin rotation or relaxation), there is a technique known as Avoided Level Crossing Resonance (ALC-μSR) [42]. Here, the muon Zeeman splitting is tuned with a longitudinal external magnetic field to match the splitting between electron spin levels in the sample. The resonance is detected by the loss of polarization of the muons, which is induced by a flip-flop transition. ALC-μSR can only determine the position of the resonances, and cannot map the topology of the crossing.

Electron spin resonance (ESR) is a powerful tool to study magnetic transitions (Chapter 2). For the study of level crossings, multiple frequencies are inevitable (see Fig. 3.2). Because common and available resonant ESR setups in the needed frequency range are tunable only in a very narrow region, level crossings and avoided crossings cannot be studied in detail [2]. Nonresonant methods, like frequency domain magnetic resonance spectroscopy (Chapter 2.3.3) and transmission or reflection measurements in a coaxial cable, have too low sensitivity to observe the transitions between different spin multiplets. These transitions are normally not allowed, and only obtain a nonzero matrix element if the levels are mixed. This mixing can be caused, for example, by hyperfine interactions, or close to a level crossing due to antisymmetric exchange interactions. Thus a

setup combining the sensitivity of a tunable cavity with broadband microwave components is suitable to perform such a measurement. Here we present a setup capable of covering the frequency range from 5–40 GHz. In Chapter 2.3.2 other experimental approaches to perform microwave absorption measurements at low temperatures in a wide frequency range are given.

3.2 Experimental Setup

3.2.1 Measurement Principle

In the following we will discuss the transmission properties of a cavity, if the real part (χ') or the imaginary part (χ'') of the magnetic susceptibility of a sample at resonance field change compared to the initial value. Two effects are detected with the network analyzer: First, there is absorption of electromagnetic radiation due to χ'', second there is dispersion due to χ'. Due to the nonzero χ'', the quality factor Q_{unloaded} of the unloaded cavity changes. This change in Q also depends on the filling factor η [29]:

$$\Delta Q = -\chi'' \eta Q^2_{\text{unloaded}}. \tag{3.1}$$

With a change in χ', the wavelength of the standing wave inside the cavity changes. For $\chi'' = 0$ the frequency shift is [29]

$$\Delta f = \frac{1}{\lambda\sqrt{\mu_0 \epsilon_0}} \left(\frac{1}{\sqrt{\chi'}} - \frac{1}{\sqrt{\chi' + \Delta\chi'}} \right). \tag{3.2}$$

Absorption and dispersion in magnetic resonance are connected by the Kramers-Kronig relations. With the used detection method, both absorption and dispersion can be measured simultaneously, by monitoring the quality factor and the resonance frequency of a certain mode as a function of external magnetic field. In test measurements, it will be explored whether either absorption or dispersion can be measured with higher precision.

3.2.2 Cavity Design

Our goal was to design a microwave system to perform ESR measurements in a wide frequency range from 5–40 GHz with high sensitivity.[1] To be able to

[1] Considering the experimentally observed signal-to-noise ratio of the measurement in Chapter 3.4.1 we give a rough estimation of the number of spins which can be detected: At

completely study a level crossing, any frequency in this range should be accessible. A further requirement is the incorporation of the setup in a superconducting magnet system, to be able to access the fields of level crossings, which can be high (several T). In most X- or Q-Band ESR setups, which operate at fixed frequencies in the required range, the magnet systems are not capable of reaching fields >2 T. Previously, in the frequency range from 40–60 GHz, a tunable cylindrical cavity was employed [43]. Using basic considerations from this approach, we constructed a setup which works from 5–40 GHz, that means it covers a much wider relative range compared to the setup from [43].

In microwave technology, cylindrical cavities have been widely used, because they are relatively easy to produce and because analytical solutions exist for the eigenmodes [44]. Rectangular cavities are another commonly used type of cavities. Due to the cylindrical magnet core we decided to employ a cylindrical cavity. Moreover, tunable cylindrical cavities in transmission mode used to be wavemeters. These setups make it possible to read the frequency via the setting of a screw which indicates the height of the cavity, at maximum transmission [45]. The TE_{011} mode in a cylindrical cavity shows no microwave currents between the cylindrical walls and the end plates (Fig. 3.5(a)). Therefore, the end plate can be moved without the necessity of a good electrical contact to the cylindrical walls. The cylindrical cavity built (Fig. 3.3) has a diameter of 27 mm and a variable height of 0–40 mm. The chosen diameter is the maximum diameter available in the magnet core, and leads to the desired frequency range (see quantitative analysis below). The tuning mechanism is made such that the plunger on top of the cavity stays in position, while the cap at the bottom is moved. This has the advantage that samples attached to the top of the cavity stay at the same position in the external magnetic field, while varying the cavity height in-situ. Moreover, the microwave radiation is coupled into the cavity at the stationary top. The whole cavity is made out of copper, both because of low losses due to the small skin effect resistance, and the large thermal conductivity (see Chapter 3.2.4).

For cylindrical cavities, analytical solutions for the magnetic and electric field distributions are known. In addition, we performed simulations of the eigenmodes using CST microwave studio, a finite elements 3D electromagnetic simulation program [46]. Thus, we were also able to study the influence of dielectrics, which

14.35 GHz, 10^{13} spins can be detected per 0.1 mT linewidth with $\vec{B}_0 \perp \vec{B}_1$, at the parallel orientation $\vec{B}_0 \| \vec{B}_1$ in the order of 10^{12} spins can be detected. For this calculation the number of spins in a 2.4 mg crystal of V_{15} and the linewidth of the transition were considered.

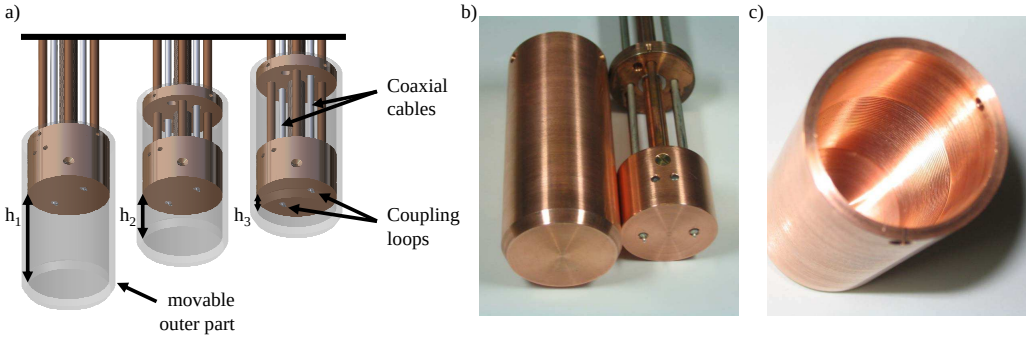

Figure 3.3: (a) CAD drawing of the cavity at three different positions of the movable outer part. The top plunger of the cavity stays fixed in the laboratory frame. (b) and (c) show photographs of the actual setup including the coaxial cables, but without temperature sensor and heater.

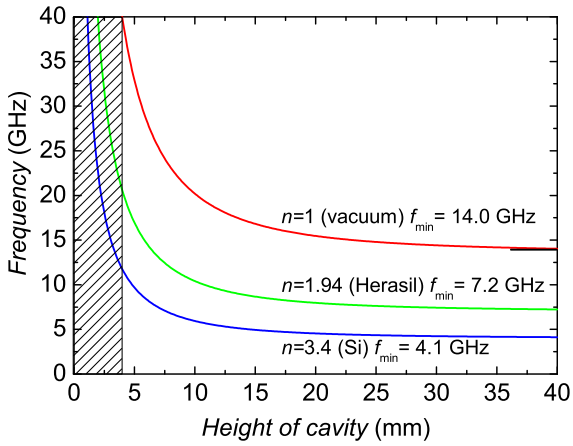

Figure 3.4: Frequency of TE_{011} mode in a cylindrical cavity (radius $a = 13.5\,\mathrm{mm}$) dependent on cavity height for three dielectrics (filling factor 1).

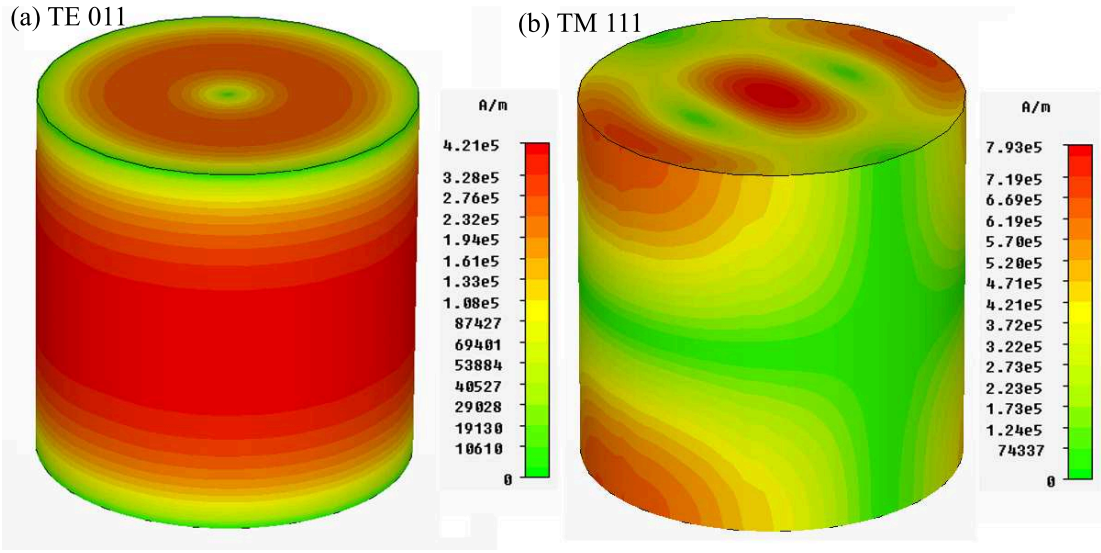

Figure 3.5: Surface currents determined with CST microwave studio in a cylindrical cavity with $h = d = 27\,\text{mm}$ for the modes (a) TE_{011} and (b) TM_{111}

were partly inserted into the cavity. The resonance frequencies of the transverse electric TE_{mnp} modes in a cylindrical cavity with height d, radius a are [29]

$$f_0 = \frac{\sqrt{\left(\frac{c(k_c a)'_{mn}}{\pi}\right)^2 + \left(\frac{cp}{2}\right)^2 \left(\frac{2a}{d}\right)^2}}{2a}. \tag{3.3}$$

Here, c is the speed of light, and $(k_c a)'_{mn}$ is the nth root of the mth-order Bessel function, while $J'_m(k_c a) = 0$. Introducing a dielectric with a refractive index of $n > 1$ into the cavity, reduces the resonance frequency by a factor of $1/n$. The TE_{011} mode is commonly used in ESR, normally by placing the sample in the middle of the cavity, with $\vec{B}_0 \perp \vec{B}_1$ [29] and a vertical external magnetic field. The TE_{011} mode is suited for our measurements due to the symmetric, simple field distribution, and the possibility to place the sample both in a defined $\vec{B}_0 \| \vec{B}_1$ or $\vec{B}_0 \perp \vec{B}_1$ configuration. Therefore, in the following we will only focus on the TE_{011} mode. The theoretical frequency-height dependence of the TE_{011} mode for the constructed cavity, according to Equation 3.3, is shown in Fig. 3.4. For cavity heights of $< 4\,\text{mm}$ the area is shaded, as here the microwave field will be inhomogeneous in the sample volume and the cavity quality factor decreases significantly. In vacuum, a frequency of 40 GHz is reached at a cavity height

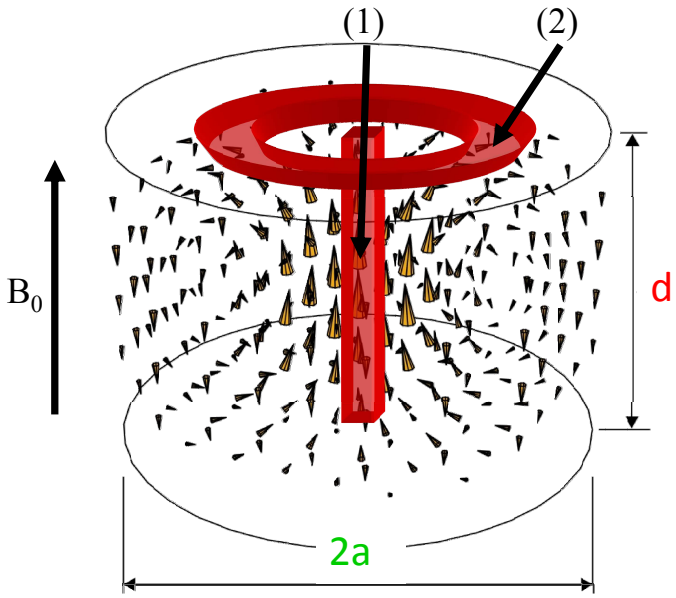

Figure 3.6: Magnetic field vector plot of the TE_{011} mode in a cylindrical cavity with $d = 2a$. Possible sample positions are given in red. The plot is the result of a simulation with CST Microwave Studio [46]. (1) denotes the position for a $\vec{B}_0 \| \vec{B}_1$ position, whereas for (2) $\vec{B}_0 \perp \vec{B}_1$ is fulfilled.

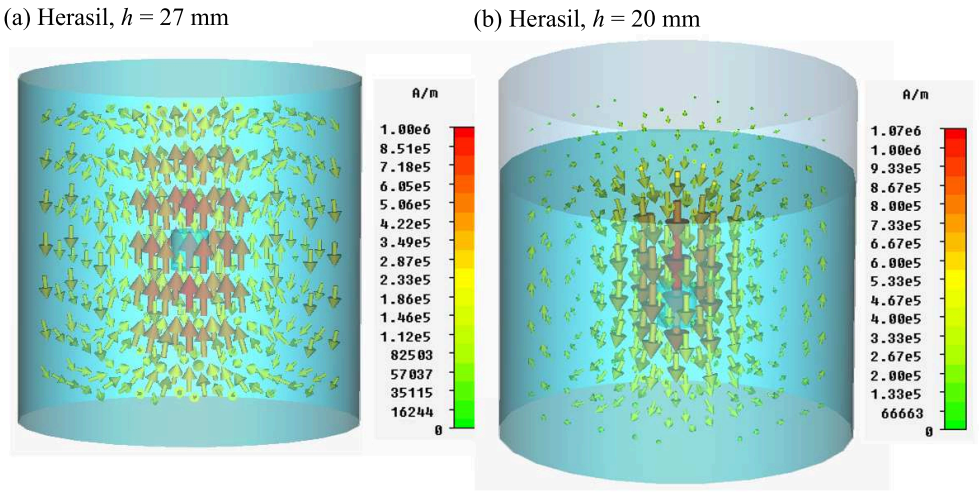

Figure 3.7: Magnetic field distribution for cavities filled with dielectrics ($n = 1.94$) as simulated using CST microwave studio [46]. (a) Simulation for a cylindrical clearance (vacuum) which accounts for the sample space in the middle of the cavity. (b) Simulation for a cylindrical clearance and an incomplete filling in height to account for the tuning of the height above the filling height (20 mm).

of about 4 mm, at 40 mm height the minimum frequency of about 14 GHz is reached. Introducing dielectrics into the cavity reduces the effective minimum frequencies. Two materials, which were both used in experiments were included in the plot: Herasil, a type of quartz glass from Heraeus and single crystalline silicon. The refractive indices of both were experimentally determined at 14 GHz by measuring the resonance frequency without and with dielectric. To reduce the frequency significantly by changing the dimensions of the cavity, a cavity with a larger radius would be necessary. This is not possible in the available space in the magnet bore. Fig. 3.5 shows the surface currents from a simulation for the employed TE_{011} mode and the degenerate TM_{111} mode. This illustrates, how it is possible to suppress the TM_{111} mode by the introduction of a gap in between the plunger and the walls (in the experiment: 0.5 mm): In contrast to the TE_{011} mode, the TM_{111} mode exhibits surface currents at the boundaries, whereas the TE_{011} remains virtually unaffected by the introduction of the gap. Fig. 3.6 shows the magnetic field vector plot of the TE_{011} mode in a cylindrical cavity as a result of a CST microwave studio simulation. In a vertical external magnetic field the sample can be either positioned on the axis of the cavity (1) ($\vec{B}_0 \| \vec{B}_1$) or on the

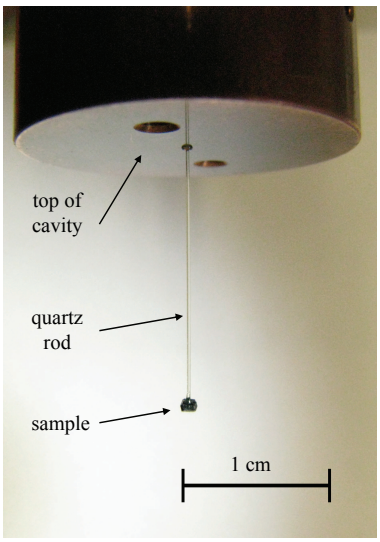

Figure 3.8: Photograph of a sample put on the position in the center of the cavity using a quartz rod.

top (2) or bottom of the cavity ($\vec{B}_0 \perp \vec{B}_1$). If the sample is positioned on the top of the cavity, the frequency tuning can be used without restrictions, because the sample remains at the same position with respect to the external magnetic field distribution at all times. If the sample is put on the symmetry axis of the cavity, especially in the geometrical center of the cavity where the alternating magnetic field is strongest, the cavity can only be tuned in a small range, because the sample position cannot be varied in-situ. Moreover, care has to be taken that for the position of the sample the whole setup is moved up in the VTI, so that the sample stays in the center of the external magnetic field. Fig. 3.7(a) shows the magnetic field distribution for an incomplete filling with Herasil. Here, a cylindrical volume of $d = 3\,\mathrm{mm}$ and $h = 3\,\mathrm{mm}$ in the middle of the cavity is simulated being vacuum, a blind hole was used as a sample space (analogous to the experiment). The field distribution remains virtually unchanged compared to the nonfilled version of the resonator. To access a small tuning range with a dielectric filled resonator, we varied the resonator height beginning from the height of the dielectric. This corresponds to a partly filled resonator, as simulated in Fig. 3.7(b). Here, a filling of 20 mm Herasil in a total 27 mm cavity height was assumed. It can be seen, that the field distribution at the sample position is

still comparable to the non-filled case. Thus, we can tune the cavity in a small range to access different frequencies, also while a dielectric is present in the cavity. Fig. 3.8 shows a photograph of a sample put into the center of the cavity using a quartz rod. Because on the symmetry axis of the cavity, the electrical fields of the TE_{011} mode are negligible, the different dielectric constant of quartz does not change the mode significantly.

3.2.3 Microwave Measurement System

To transmit electromagnetic radiation from the network analyzer to the cavity in the low-temperature insert and back, waveguides have to be used. In this frequency range, possible waveguides are either rectangular or cylindrical hollow waveguides or coaxial lines. We employed semi-rigid coaxial cables (Micro-coax, type UT-085C-TP-LL), which have an impedance of 50 Ω. Most ESR setups use hollow waveguides rather than coaxial cables. We have opted for coaxial cables, because for the frequency range which we want to access, only a waveguide having a cutoff frequency below the lower frequency limit of the cavity would be applicable. For higher frequencies the waveguide would then constitute an oversized waveguide. At low frequencies, appropriate waveguides reach dimensions which cannot be implemented in the magnet bore. For frequencies above 4 GHz, a cylindrical waveguide with a diameter of a minimum of 16 cm would have to be used.

The outer conductor of the used coaxial cables is made of tin-plated copper, the dielectric of low-density PTFE and the inner conductor of silver-plated copper. This cable exhibits low microwave losses, compared to other coaxial cables for this frequency range (e.g. 1.88 dB/m at 10 GHz). Therefore it is ideally suited to perform measurements with a network analyzer, where a sufficient transmission is required for a good signal to noise ratio. At the same time, a copper cable leads to increased heat conduction into the cryostat, compared to for example a stainless steel cable. Experiments using a section of stainless steel cable (length: 50 cm) in the region of the highest temperature gradient, showed only minor improvements in the base temperature (about 0.1 K), therefore the more robust, lower loss solution of continous copper cables was used. The total length from the test set (see below) to the cavity is about 2 m of coaxial cable. The coupling from the waveguides into the cavity is inductive in the experiment, which means that the AC current in a conductor induces an alternating magnetic field. To do so, the cables extend into the plunger of the cavity. At the end of the coaxial

cable, the inner and outer conductor are connected with a semicircle. The loop is oriented so that the direction of the induced change in magnetic field lines (through the loop) corresponds to the field direction of the magnetic field in the TE_{011} mode. This means the plane of the loops is oriented perpendicularly to the diameter of the upper plate. This kind of coupling supports the TE_{011} mode (and other TE_{01n} modes), because these modes exhibit a magnetic field distribution which is oriented in the same direction as magnetic fields induced by the coupling loops. This coupling to the magnetic field is called inductive coupling, in contrast to coupling to the electric field, which is called capacitative coupling. Capacitative coupling, that means the coupling with an open-ended coaxial cable, was also investigated (see Chapter 3.3.1). The penetration depth of the coupling loops into the cavity determines the strength of the coupling. First, at room temperature the coupling strength was optimized, and then fixed for low-temperature measurements. Please note that in our case an optimal coupling does not mean critical coupling. Critical coupling would mean, that no microwave power is reflected, except if the resonance condition is fulfilled. This means that the energy coupled into the resonator compensates for the losses. In our case, because the coupling is not variable, we cannot account for the major differences in coupling for different frequencies and therefore do not have critical coupling.

We employ a Hewlett Packard HP 8510 vector network analyzer system operating at frequencies from 45 MHz up to 40 GHz. The system consists of the HP 8510B network analyzer, a HP 83620A microwave source and a HP 5516A test set. We connected the test set to the coaxial cables using microwave connectors from Rosenberger of the 2.4 mm standard. At 20 GHz, the microwave power in the cavity is about 1 mW, considering an output of 10 dBm at the test set of the network analyzer, an attenuation of 6 dB in the coaxial cables (only once the distance to the cavity) and 4 dB for the coupling. This estimate is strongly frequency dependent, because both attenuation in the cables and coupling are frequency dependent.

3.2.4 Temperature Control and Cryogenics

To be able to cool the sample to low temperatures, we incorporated the setup into a variable temperature insert (VTI) of an Oxford Instruments Superconductive Magnet System, with fields up to 10 T. The VTI allows us to vary the temperature of the sample and the cavity over a wide range (1.5–300 K). A VTI is a stainless steel cylinder which is vacuum-insulated from the liquid helium reservoir. An

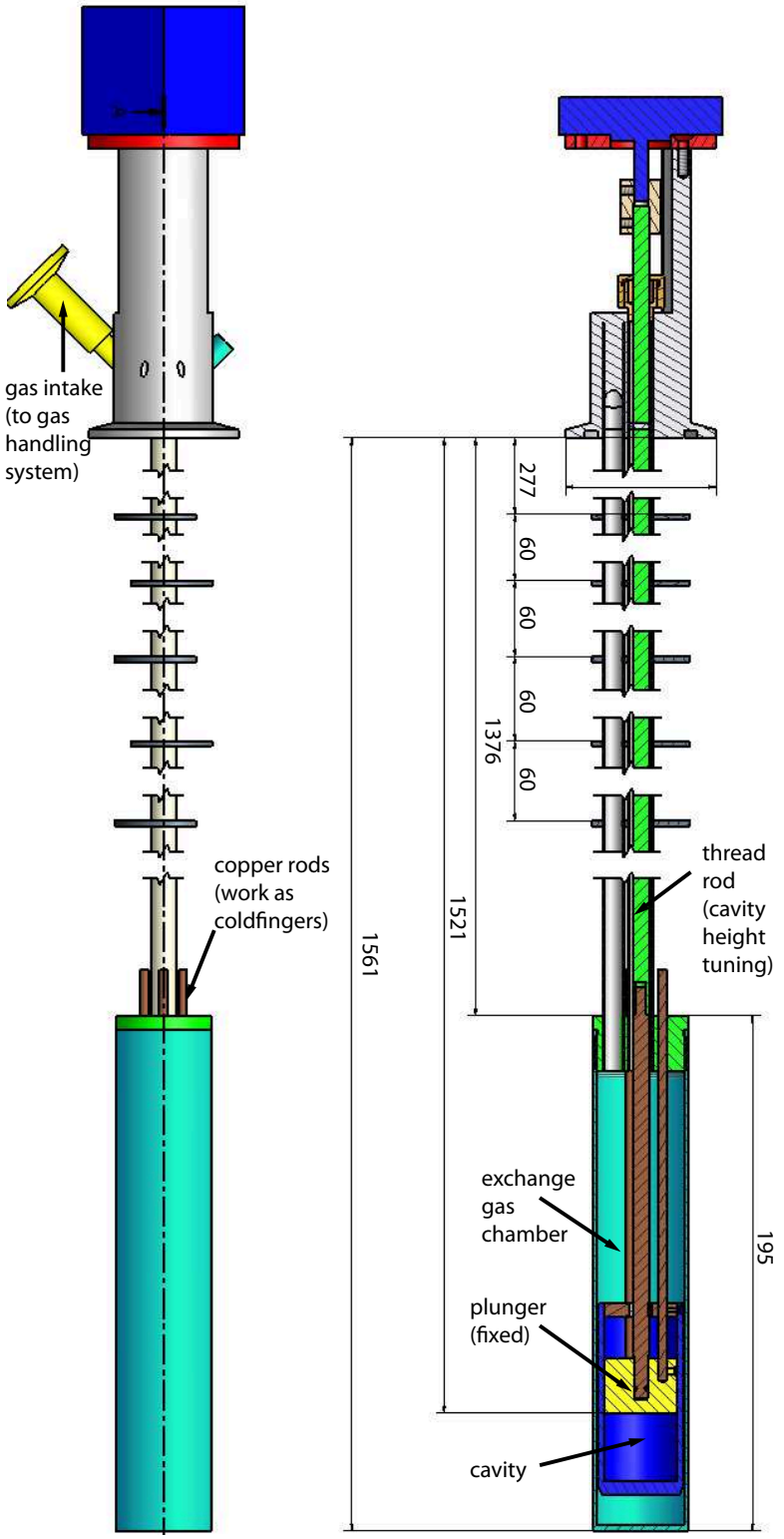

Figure 3.9: Technical drawing of complete insert. The figure on the right shows a cut through the middle of the insert, while the one on the left shows the insert from the outside. Lengths in the plot are given in mm.

indium sealed capillary tube equipped with a needle valve connects the VTI to the helium reservoir. This needle valve can be adjusted with a stepper motor, to control the liquid helium flow into the VTI. By pumping on the VTI with a rotary pump, the flow is maintained, and the VTI can be cooled to below 4.2 K by reducing the vapor pressure of liquid helium in the VTI. Fig. 3.9 shows the complete cavity insert. On the right the cavity volume can be identified in between the blue cap and the yellow plunger. The cavity is surrounded by an exchange gas chamber (in turquoise). This chamber is connected with a gas handling system on top of the insert (yellow intake on the left). Thus, we can vary the pressure in the cavity independently of the VTI. Even more important, the pressure fluctuations due to boiling helium in the VTI are prevented in the cavity itself. Pressure fluctuations of helium will lead to a change of cavity frequency, even though the refractive index of helium (1.000035) is close to that of vaccuum. During the experiment, the pressure in the exchange gas chamber is kept constant. To avoid condensation of helium, for temperatures below 4.2 K the pressure in the exchange gas chamber has to be lower than the one of the VTI.

Both temperature sensor (Lake Shore Cernox CX-1050-AA) and heater (Watlow, C1A-7863, 30 W) were incorporated in adequate holes in the plunger and thermally coupled to it using vacuum grease. Because for low pressures in the exchange gas chamber, the cooling rate would be too low, we use a cold finger technique to efficiently cool the cavity and sample: The cavity is fixed with three copper rods which are fixed themselves on top of the exchange gas cylinder in a copper block. Using the Oxford Instruments temperature controller ITC 503, it is possible to control the setting of the needle valve and the heater automatically. The cavity frequency depends crucially on temperature, due to thermal expansion of the cavity itself. Therefore the temperature was kept stable for a long period (typically for more than hours, dependent on the temperature step size) to allow for thermalization before starting the measurement. Below 4.2 K, the temperature was stabilized setting a fixed needle valve opening, which led to a more stable temperature compared to the case where it was controlled by the ITC. For measurements with $\vec{B}_0 \perp \vec{B}_1$, the sample was attached to the plunger of the cavity with grease, which ensures an excellent thermal contact in between cavity and sample, because the plunger of the cavity is made of copper. In the case of dielectrics incorporated in the cavity, and the sample positioned in the position in the middle of the cavity, a long thermalization time is required, because both Herasil and silicon have low thermal conductivities at low temperatures.

We performed data aquisition with a self-written LabView program. Princi-

pally, we want to monitor the transmission properties of the cavity dependent on external magnetic field. In the following we will give a hands-on guide which steps are performed by both the user and the program to record a spectrum. First, the desired mode is identified manually by using the network analyzer. The theoretical frequency-height dependence allows the rough determination of the center frequency. Subsequently, the exact actual center frequency (which depends also on temperature) can be defined using the maximum function of the network analyzer after performing a transmission measurement in the relevant range. This exact cavity resonance frequency, and the approximate value for twice the FWHM as a sweep width are entered in the LabView program. Moreover, the magnetic field range and step size are entered. Then, after pressing the start button, the program performs the automatic setting of a field point controlling the magnet power supply. After the field point is reached, the transmission is measured and averaged over a certain number of cycles (in most measurements: 32). By recording several cycles, the signal to noise ratio is increased. The LabView program now performs a fit with a Lorentzian lineshape of the magnitude of the transmission to determine the maximum position and width of the cavity resonance. Only the points in proximity the resonance position are used for the fit, because they contain the most of the information about the position. The number of fit points (800 corresponds to 2·FWHM) can be set in the program. After that, the new field point is set, and a new transmission measurement is performed. The complex transmission raw data, the maximum position (transmission and frequency) and mean square error (MSR) of the fit are saved.

3.3 Characterization of the Setup

3.3.1 Empty Cavity

To study the characteristics of the empty cavity, we performed field-dependent measurements without a sample.

First, we studied cavity resonances from 5–40 GHz by sweeping the frequency in a broad range with high resolution. The different modes fulfill the expected frequency-height dependence (Equation 3.3).

Fig. 3.10 shows a detailed measurement of the field-dependence of the TE_{011} mode at about 15 GHz at 139 K from 0 T to 8 T. The transmission, the quality factor Q of the cavity, the resonance frequency and the mean square error of

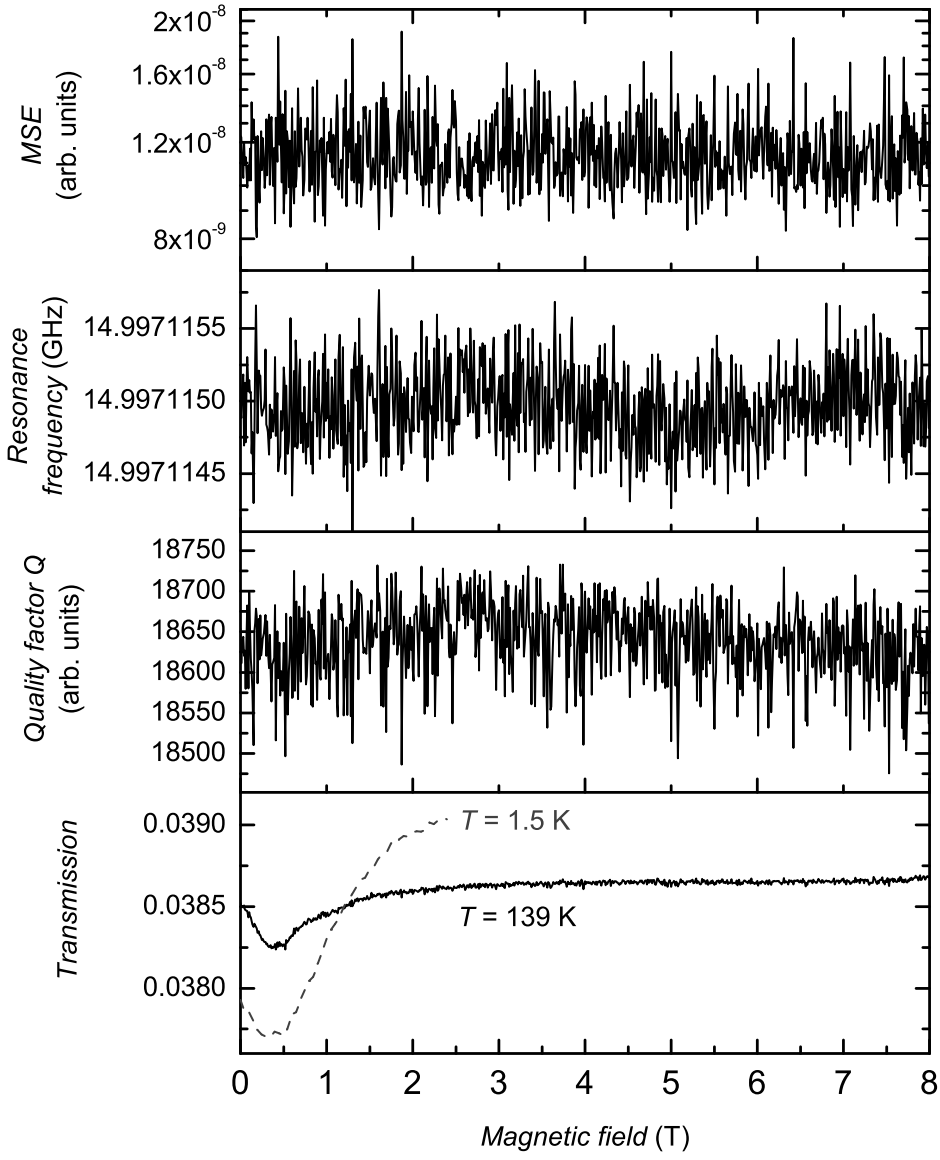

Figure 3.10: Field dependent measurement of the properties of the empty cavity at 139 K. MSE is the mean square error of the Lorentzian fit of the cavity resonance which leads to the other three values. The resonance frequency is the baseline corrected (for a linear temperature drift) resonance frequency of the cavity. The quality factor Q is determined by $Q = \frac{f}{\mathrm{FWHM}}$, whereas FWHM is the width of the cavity resonance. The transmission is the maximum transmission of the cavity resonance.

the fit, which gave the other three values are presented. The transmission signal has a low relative noise, but is superimposed on a background absorption. This absorption is centered around 0.42 T and has a width of about 1 T, showing an asymmetric lineshape. The value of the transmission is reduced by about 1% at 0.42 T. From 3 T to 8 T the transmission is virtually constant at about 0.0386. The absorption background signal is temperature dependent (see dashed trace), and is strongest for lowest temperature. At 1.5 K, the background absorption is about 3.6% of the maximum transmission. The reason for the field-dependent background absorption was not identified. Possible reasons are magnetic impurities in the copper cavity, or in the coaxial cables. This background signal complicates the measurement of broad ESR lines at low fields, because it is not reproducible. Nevertheless, the frequency dependence in a measurement with a sample gives an indication if a magnetic resonance line is observed: In this case also χ' changes, therefore the frequency shows a dispersive behaviour (Eq. 3.2). The resonance frequency shows a linear dependence on field, it changes by about 0.0001% over the whole field range, for this baseline the data shown in the plot was corrected. After correction the frequency can be assumed to be constant. The linear background in frequency was identified by changing the magnetic field sweep direction, to be due to a very slow temperature drift: This drift leads to a small variation of the cavity dimension, which then lead to the drift in frequency. For the observed drift of $\approx$15 kHz, the length change of the cavity would have to be $\approx$0.1 μm. On a piece of copper with the length of $\approx$5 cm, the temperature change would have to be $\approx$0.1 K to reach this expansion, which is within the error for the temperature. Because the cavity walls also expand, the actual temperature change would have to be even less. Because the change in frequency is smaller, the measurement shows that the frequency can be considered to be constant over the whole range. Moreover, it shows that the resonance frequency can be determined with a high precision. The lack of any frequency shift indicates, that χ' of the materials in the cavity is constant over the applied field range, because there is no signal superimposed to the frequency drift. The quality factor Q of the cavity cannot be determined with the same precision as the resonance frequency, because the line is not ideally symmetric, therefore the fit error leads to an error of about 0.5% for Q.

For a high sensitivity in the determination of ΔQ, a high Q_{unloaded} is necessary. Q_{unloaded} is given by the sum of the reciprocals of dielectric losses Q_ϵ, ohmic losses Q_Ω, and radiative losses due to the cavity coupling holes and the gap in between

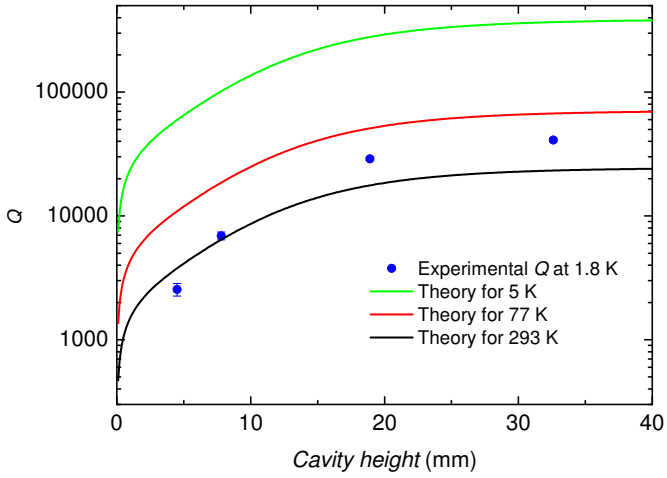

Figure 3.11: Theoretical dependence of Q on the cavity height for a cavity with a diameter of 27 mm for three different temperatures and experimentally observed quality factors.

plunger and cavity walls Q_r:

$$\frac{1}{Q_{\text{unloaded}}} = \frac{1}{Q_\epsilon} + \frac{1}{Q_\Omega} + \frac{1}{Q_r} \tag{3.4}$$

For low cavity heights, i.e. for high frequencies, the quality factor is reduced significantly [29]. Most literature only mentions Q_Ω as a product of $Q_\Omega \frac{\delta}{\lambda}$, where δ is the frequency dependent skin depth, and λ is the wavelength. We calculated Q_Ω in respect of the radius a and height d of the cavity using Eq. 3.3 and Q_Ω for a cylindrical cavity [47]

$$Q_\Omega = \frac{\epsilon_r c \left[((k_c a)'_{mn})^2 + (\frac{\pi a}{d})^2\right]^{3/2}}{2\pi f_0 \delta(f_0) \left[((k_c a)'_{mn})^2 + (\frac{2a}{d})(\frac{\pi a}{d})^2\right]}.$$

Here, $(k_c a)'_{mn}$ is the nth root of the mth-order Bessel function, whereas $J'_m(k_c a) = 0$, and $\delta(f_0)$ is the skin depth, which is dependent on frequency and electrical conductivity σ as $\delta = (\pi f_0 \mu \sigma)^{-1/2}$. Electrical conductivities for copper at low temperatures were taken from [48]. The resulting theoretical Q_Ω-dependence, only based on electrical losses, can be seen in Fig. 3.11. One can clearly see that a large cavity height leads to high Q-factors. At low cavity heights, that means increased

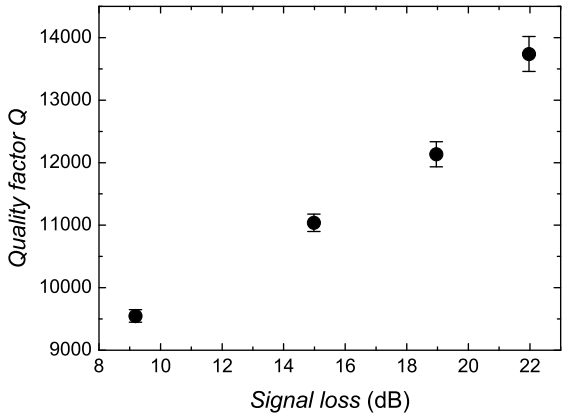

Figure 3.12: Q-factor dependent on signal loss due to reflection at the coupling loops and resistive losses inside the cavity.

frequency, Q is significantly reduced. We show the experimental cavity Q_{unloaded} at 1.8 K at four different cavity heights. The coupling was adjusted, so that the losses due to coupling at different heights should be comparable. The conductivity for $T < 10\,\text{K}$ does not change significantly [48], therefore the measurement points should be compared to the 5 K theoretical dependence. For a large cavity height, the experimental Q_{unloaded} is close to the expected value from ohmic losses only, whereas for the small cavity height the experimental Q_{unloaded} is significantly below the expected value. A significant difference in losses due to coupling cannot be the reason for the low Q-factor at high frequencies. Probably, the stronger relative deviation from an ideal cylindrical shape for low cavity heights leads the observed values of Q. In a tunable cavity, the tilt of the top plate in respect to the bottom plate relative to the absolute height is larger for small cavity heights.

If a dielectric is introduced into the cavity, Q_Ω is reduced as follows: With the same dimensions of the cavity, the wavelength of a certain mode remains constant, whereas the frequency is changed (see Fig. 3.4). At a different frequency f_0, the skin depth δ changes with $\delta \propto 1/\sqrt{f_0}$. Because $Q_\Omega \propto 1/\delta$, and because the frequency changes with $f_0 \propto 1/n$, we obtain

$$Q_\Omega \propto \sqrt{f_0} \propto 1/\sqrt{n}. \tag{3.5}$$

Additionally, the dielectric losses of the material brought into the cavity has to be taken into account (Eq. (3.4)). Experimentally, Q-factors of up to 40,000 (at

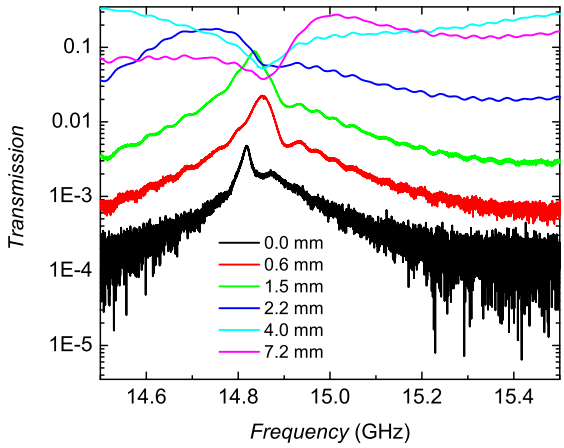

Figure 3.13: Transmission through of the cavity for capacitative coupling for different lengths of the antenna.

14.35 GHz) were found in a cavity at low temperatures without dielectric, but with sample. Using Herasil as a dielectric, Q_{unloaded} decreased to 21,000 at 7.58 GHz. For a silicon-filled cavity, $Q \approx 4{,}000$ at 4.70 GHz. These measurements are not directly comparable, because both cavity height and coupling vary, but give an order of magnitude of the reachable quality factors. To investigate the influence the coupling on the quality factor Q, the coupling strength into and out of the cavity was varied by shifting the loop. Fig. 3.12 shows Q dependent on signal loss. The signal loss was calculated subtracting the losses in the coaxial cables from the total transmission. The losses in the coaxial cables were calculated using the attenuation specifications for the cable. For higher signal losses than the shown 22 dB, the cavity resonance could not be distinguished any longer from background noise. The cavity quality factor Q is limited by the resistive losses inside the cavity and the loss due to coupling. Reducing the coupling may lead to a situation, where resistive losses dominate Q. We do not reach this limit, because upon reduction of the coupling, Q increases up to the weakest coupling which we were able to investigate with the setup. A quantitative optimization of the coupling in respect to sensitivity is possible ([29]. p. 419). We did not perform this optimization, because the optimal coupling varies for different cavity heights, and optimizing the coupling in-situ while changing the frequency is not feasible.

To investigate, if capacitative coupling would be advantageous instead of in-

ductive coupling, we varied the coupling with an open-ended coaxial cable with an inner conductor that is longer than the outer conductor of the cable by a certain length between 0 and 7.2 mm. The transmission of the cavity around the resonance frequency of the TE_{011} mode ($\approx 14.8\,\mathrm{GHz}$) is shown in Fig. 3.13. Capacitative coupling leads to low Q-factors even at weak coupling as indicated by the broad resonance, whereas for strong coupling (long antenna) the transmission data does not show any significant cavity resonance any more. Therefore we conclude that capacitative coupling is not suitable for coupling to the TE_{011} mode in the used coupling hole geometry. Thus, all measurements were performed by using inductive coupling.

3.3.2 Magnetic Resonance Test Measurements

To determine the characteristics of the setup for magnetic resonance measurements, we performed test measurements. Note, that in the following we discuss two types of resonances: On the one hand, the cavity resonance, being a result of a standing wave pattern, and on the other hand the magnetic resonance absorption due to the sample. The setup is optimized for samples with large linewidths, which requires frequency and transmission stability over a broad field range. Less emphasis was placed on the prevention of line broadening due to field inhomogeneities, and high magnetic field field resolution. Thus, standard samples in ESR like DPPH (2,2-diphenyl-1-picrylhydrazyl) are not appropriate to test the abilities of the setup. The sample chosen for the following measurements was a crystal of Mn_{20} ($((NH_4)_{32}H_{16}[Mn_{20}Mo_{132}O_{372}(SO_4)_{30}(H_2O)_{72}] \cdot 250H_2O \cdot 8SO_4^{2-}$), from Prof. A. Müller, Bielefeld) with the dimensions $2.8 \times 2.0 \times 1.2\,\mathrm{mm}$ and a mass of 7.0 mg. The measurements were performed in a $\vec{B}_0 \perp \vec{B}_1$ geometry.

To study the relation between the measured cavity transmission, frequency and resonance width, we investigate these values in detail for Mn_{20} (Fig. 3.14) at 1.8 K. From the resonance width FWHM and the corresponding frequency f_0, one can calculate the Q-factor $Q = \frac{f_0}{\mathrm{FWHM}}$. It decreases from $Q \approx 28{,}500$ out of resonance to $Q \approx 8{,}000$ at the resonance field. This shows, that the dissipation in the sample has a strong influence on the power loss in the cavity. Because the change in f_0 is negligible compared to the change in FWHM, $Q \propto$ FWHM. The field dependent resonance width was fitted with a Lorentzian ($B_0 = 0.551 \pm 0.001\,\mathrm{T}$, FWHM$= 0.078 \pm 0.001\,\mathrm{T}$). The transmission data was also fitted using a Lorentzian lineshape, which yields virtually the same center field ($B_{\mathrm{center}} = 0.549 \pm 0.001\,\mathrm{T}$, FWHM$= 0.147 \pm 0.002\,\mathrm{T}$). The Lorentzian dispersion signal has

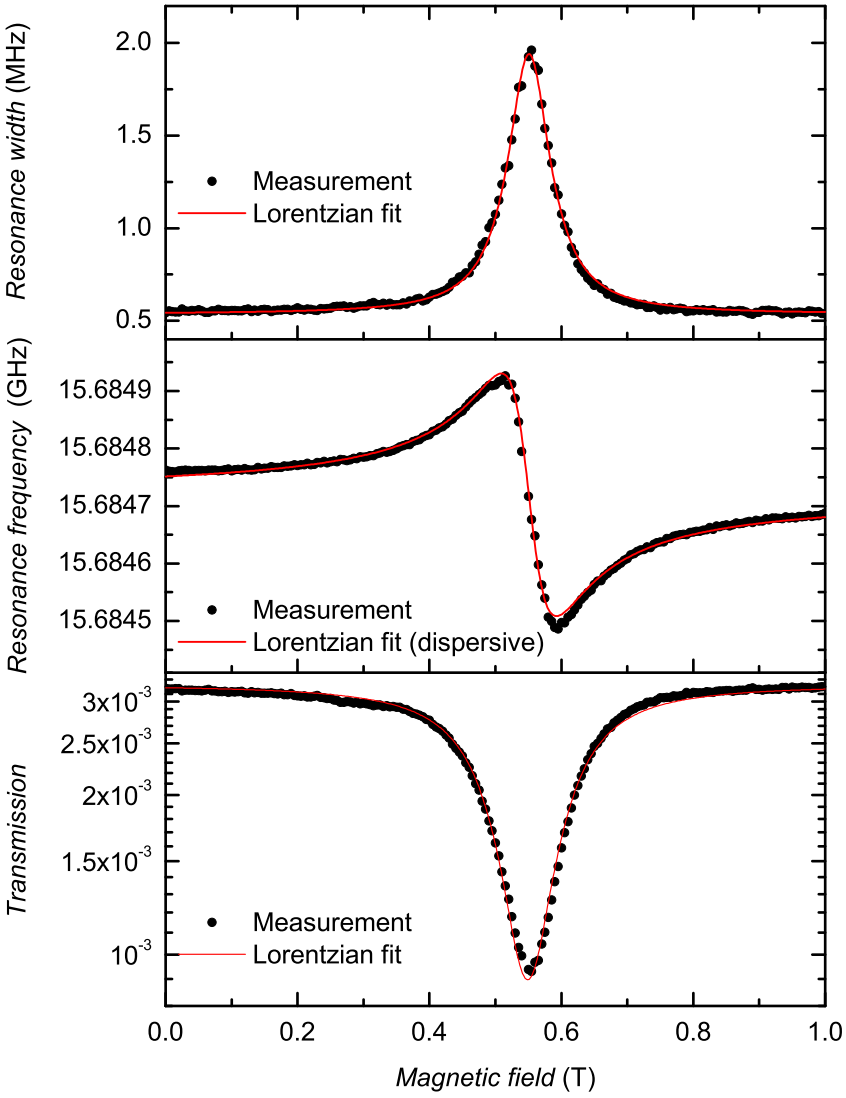

Figure 3.14: Transmission, resonance frequency and width of the magnetic resonance from an ESR measurement on Mn_{20} at 1.8 K.

the form $\frac{4[(B-B_0)/\mathrm{FWHM}]}{1+4[(B-B_0)/\mathrm{FWHM}]^2}$ [29], where B_0 is the center field, and FWHM is the width. Fitting the experimental frequency signal with this function, we gained $B_0 = 0.551 \pm 0.001\,\mathrm{T}$ and FWHM$= 0.084 \pm 0.001\,\mathrm{T}$. The common center field (for all three values) with the corresponding g-factor of $g = 2.04 \pm 0.01$ shows that the spins in Mn_{20} are virtually uncoupled. The FWHM of the fit of the transmission signal is significantly higher than for the other two values. We assign this to the strong absorption in the sample, which leads to partial saturation of the resonance line, and in consequence to a higher FWHM. Because the absorption of the sample is high (relative absorption: 71%), the background absorption found in the empty cavity measurements can be neglected.

Further measurements with lower sample volumes showed, that the signal to noise ratio is best for the cavity transmission data, rather than the frequency or cavity resonance width data. Thus, the following measurements were analyzed using the cavity transmission data.

Temperature Dependence

In order to study the intensity of absorption lines, we performed temperature dependent measurements on Mn_{20} at 36.00 GHz (see Fig. 3.15). The absorption increases for lower temperatures. The measurement data was fit using a Lorentzian. Comparing the areas of the curves from the fit with the theoretical population differences between the magnetic sublevels from Boltzmann population (see inset of Fig. 3.15), the measurements show a smaller area than expected. This shows that we are partially saturating the magnetic resonance transition. The saturation of the broad lines (about 0.1 T natural linewidth) of a transition metal system is surprising. In consequence, care has to be taken for measurements where we want to draw conclusions from the linewidth that we are not partly saturating the line. This can be done by reducing the power until no change in linewidth is visible any longer.

Frequency Dependence

To show the capabilities of the setup to perform measurements in a broad frequency range, we compare data at 15.68 GHz, 23.48 GHz and 36.00 GHz. Fig. 3.16 shows the transmission data at 1.8 K, which was normalized to 1 in transmission. The x-axis, the magnetic field relative to the resonance field, was obtained using a Lorentzian fit. Again, we expect the width of the resonance to be influenced by the saturation. Due to different microwave powers in the cavity at different

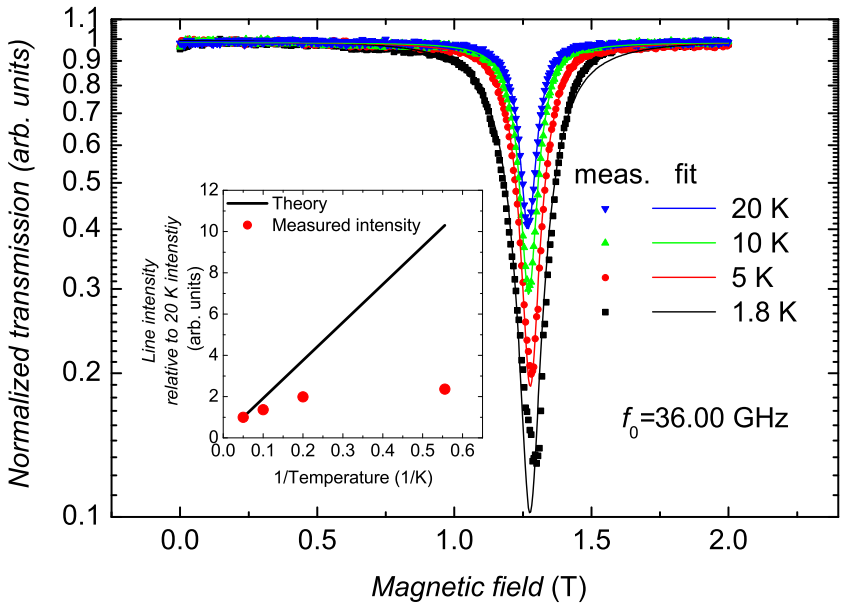

Figure 3.15: Temperature dependent absorption of Mn_{20}. The inset shows the measured line intensity (absorption area) compared to the theoretical intensity assuming a Boltzmann distribution.

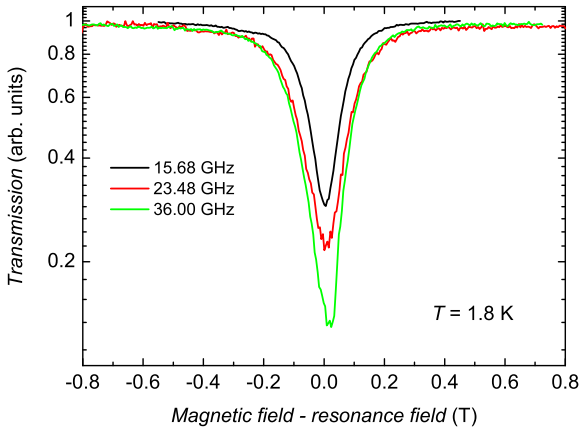

Figure 3.16: Magnetic resonance of Mn_{20} at different frequencies. The magnetic field axis was shifted fore each measurement, so that the resonance fields match.

frequencies (which induce a different coupling and a different unloaded Q), the saturation factor will differ. Moreover, the intrinsic sample magnetic resonance linewidth may be field dependent. Thus, no detailed analysis of the width dependence was performed.

3.4 Level Crossing Topography in V_{15}

The molecular magnet $K_6[V_{15}As_6O_{42}(H_2O)] \cdot 8H_2O$ (V_{15}, see Fig. 3.17(a)) was intensively studied during the last two decades [49] [50] [51] [52] . V_{15} consists of 15 V^{4+} ions each with a spin of 1/2. The V are arranged in a quasi-spherical layered structure, consisting of a triangle sandwiched by two V hexagons (Fig. 3.17(b)). The exchange-interactions lead to an $S = 1/2$ ground state and an $S = 3/2$ excited state with an energy separation of $\approx 76.5\,\mathrm{GHz}$ [53] [51] [50] [52]. These states can be obtained using the so-called three spin approximation, in which the spins of the inner triangle are coupled by an effective interaction mediated by the spins of the haxagons. Applying an external magnetic field, the $m_S = -1/2$ of $S = 1/2$ and $m_S = -3/2$ of $S = 3/2$ cross at $\approx 2.75\,\mathrm{T}$. Due to antisymmetric exchange interaction, this crossing is expected to be an anticrossing [2] [54]. Neither the energy splitting at the crossing Δ nor the topography of the levels in proximity

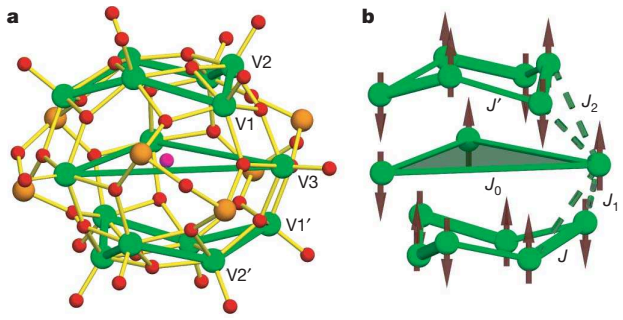

Figure 3.17: (a) Structure of the V_{15} anion (V: green; As: orange, O: red) (from [49]). (b) Schematical spin arrangement at low temperatures (three-spin approximation) and exchange interaction pathways.

of the level crossing were studied so far. We want to study the level separation close to the crossing. Because for the levels, $\Delta S = 0$, the transitions are normally not allowed in ESR.

3.4.1 Multifrequency ESR with $\vec{B}_0 \perp \vec{B}_1$

In both $\vec{B}_0 \perp \vec{B}_1$ and $\vec{B}_0 \| \vec{B}_1$ measurements, single V_{15} crystals synthesized by the group of Prof. Müller from Bielefeld were used. The mass of the crystals was around 5 mg. Because around the crossing we expect to observe ground state transitions, low experimental temperatures (1.6 K) were chosen. In all measurements, besides the specifically mentioned 90° measurements in section 3.4.2, the $\vec{B}_1$ field was oriented perpendicular to the largest face of the crystal (Fig. 3.18).

To determine, if a mixing of the spin states $S = 1/2$ and $S = 3/2$ is possible for $\vec{B}_0 \perp \vec{B}_1$, we performed ESR measurements with this field configuration. Fig. 3.19 shows the raw transmission data at 7.58 GHz and 14.35 GHz. At both frequencies an inhomogeneously broadened line around $g = 2.01 \pm 0.01$ is observed. At 14.35 GHz (see inset) the width of the Gaussian fit was determined to be FWHM $= 0.039 \pm 0.001$ T. Around the expected level crossing field of the spin states $S = 1/2$ and $S = 3/2$ at 2.75 T, no absorption was observed. This indicates that either the sensitivity of the setup is too small to detect the transition, or that for perpendicular fields the mixing of the levels cannot be detected.

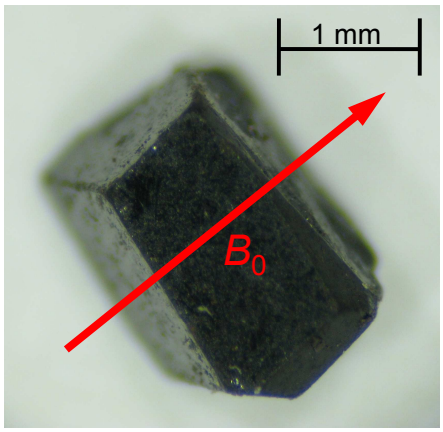

Figure 3.18: V_{15} crystal. The direction of the external magnetic field $\vec{B}_0$ in the measurements is indicated by the red arrow.

3.4.2 Multifrequency ESR with $\vec{B}_0 \| \vec{B}_1$

To study the influence of a parallel field ($\vec{B}_0 \| \vec{B}_1$) on the transition between the spin states $S = 1/2$ and $S = 3/2$ in proximity to the crossing field (≈2.75 T), we performed multifrequency ESR measurements in this frequency range. The approximate ratio of $|\vec{B}_{1\perp}|$ compared to the stronger field $|\vec{B}_{1\parallel}|$ is ≈ 10 (value obtained from CST microwave studio field simulations). Because of this, the sensitivity of the setup for non-saturated lines is 10 times higher in the parallel configurations of the fields compared to the perpendicular configuration.

The raw transmission data for two frequencies is shown in Fig. 3.20. All measurements were performed at low temperature, to ensure maximum possible population difference between the lowest lying levels. On the left, for the measurement at 10.82 GHz, two clear absorption lines centered around 2.75 T can be seen, with an absorption of about 0.3%, relative to the transmission at 5 T. Moreover, the ground state transition close to $g = 2$ can be observed, with a relative intensity of about 1%. The background absorption of the setup shows the strongest signal, which has a relative absorption of about 3.7% at 0.13 T. In the proximity of the level crossing at 2.75 T, the background was approximated by a polynomial function of second order. This allows to analyze a background-corrected signal in detail (see below). On the right of Fig. 3.20, the measured data at 4.79 GHz is shown. Here, the background absorption is much stronger than in any other measurement. This we assign to the silicon used as a dielectric at this particu-

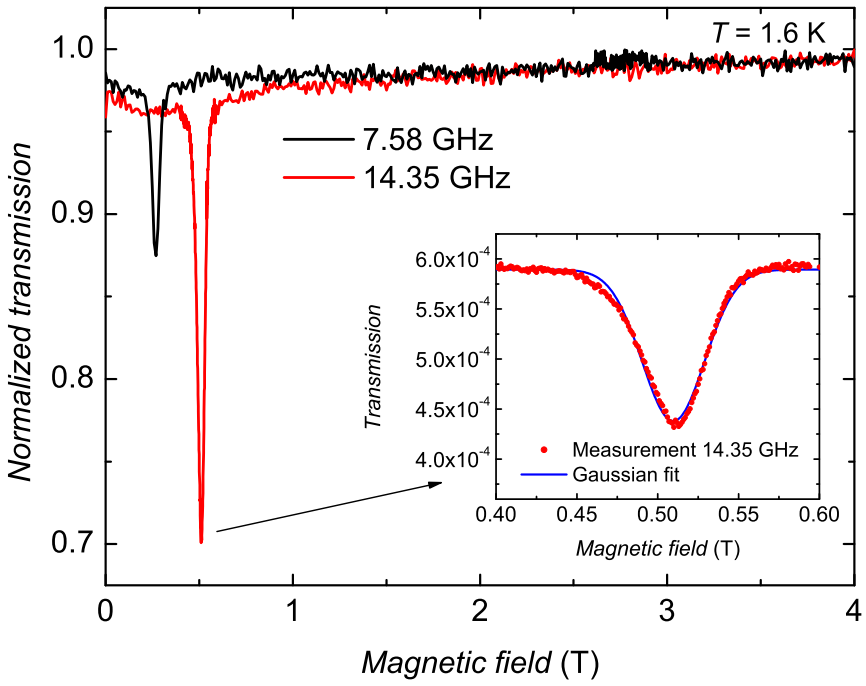

Figure 3.19: ESR measurement at two frequencies for $\vec{B}_0 \perp \vec{B}_1$ showing the field-dependent transmission through the cavity. The inset enlarges the field region in proximity of the resonance field at 7.58 GHz.

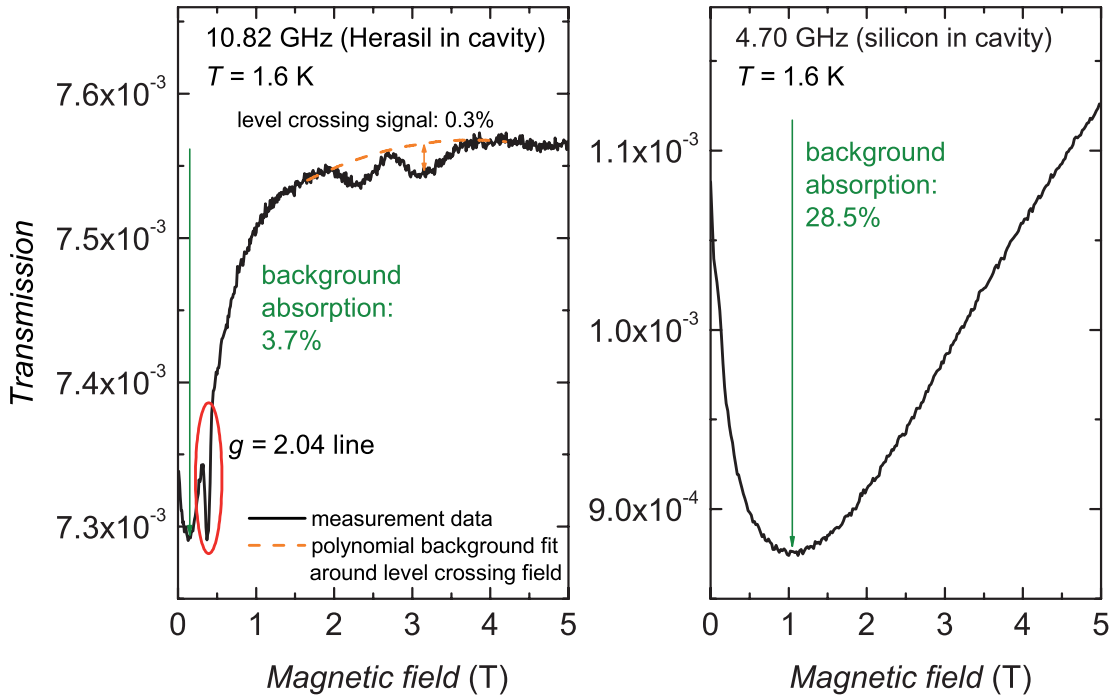

Figure 3.20: Raw transmission of V_{15} data for two frequencies. At 10.82 GHz the background absorption, the $g = 2$ line and two forbidden transitions close to the level crossing are visible. An approximation of the background to determine the absorption due to the level crossing is given by the dashed orange line. At 4.70 GHz, only a broad background absorption, presumably due to magnetic impurities of the used dielectric can be seen.

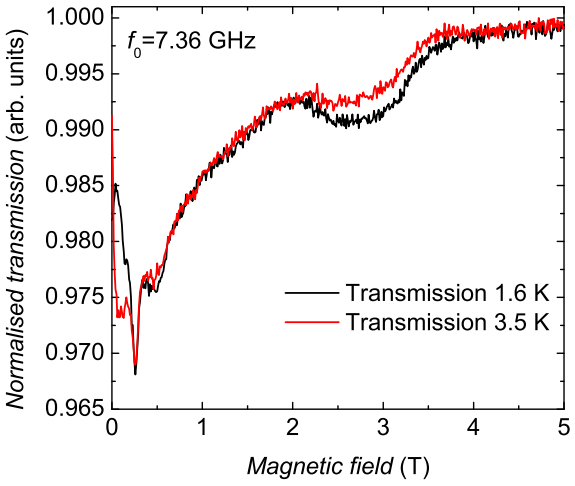

Figure 3.21: Raw transmission data of V_{15} in parallel field at 1.6 K and 3.5 K at 7.36 GHz.

lar frequency. The quality factor is about 3,800 at zero field for this frequency. The expected Q-factor according to Eq. 3.5 assuming the same loss tangent as in Herasil would be about 11,000. Therefore, a much higher loss tangent of the used silicon compared to Herasil leads is mainly responsible for the low Q-factor. No evidence of an absorption due to the sample, neither at $g \approx 2$ or around the level crossing field was found. The data is dominated by the strong background absorption of up to 28.5 % (at $\approx$ 1 T), which we assign to magnetic impurities in the silicon. This shows that in this case the sensitivity of the setup is too low for the measurement of the weak absorption close to the level crossing field. In consequence, no absorption data points below the lowest frequency accessible with Herasil (7.2 GHz, see Fig. 3.4) could be determined.

Fig. 3.21 shows the transmission data of V_{15} in parallel field at 1.6 K and 3.5 K. At 3.5 K, a significant reduction of the intensity of the signal around 2.75 T can be observed. A detailed analysis of this measurement was not performed, because the background signal is not exactly known. Further temperature dependent measurements at 14.26 GHz did not show any significant absorption close to the level crossing field at 10 K and 20 K (not shown here).

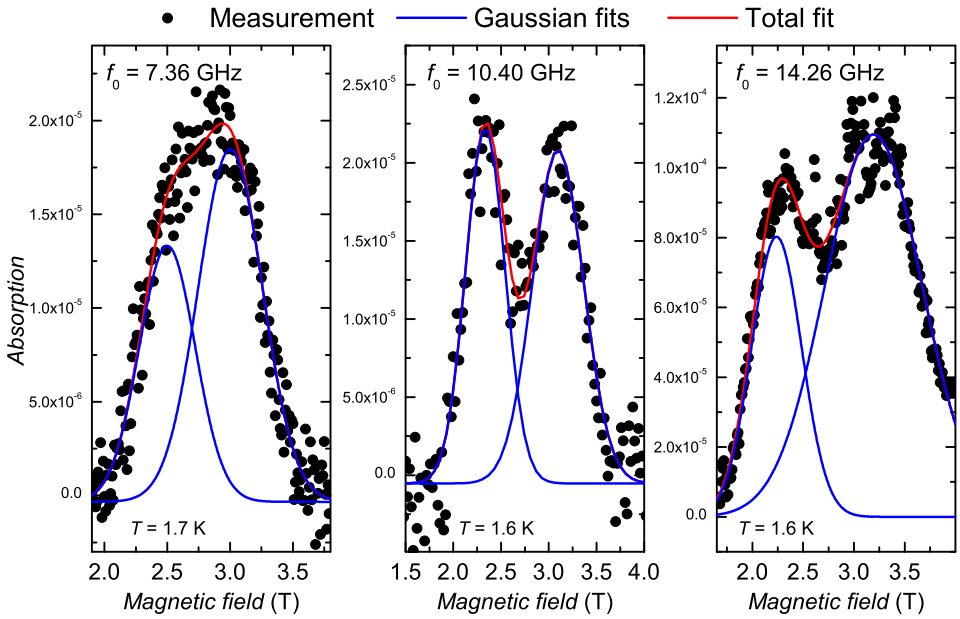

Figure 3.22: Absorption data around the level crossing field after background correction for three frequencies.

Analysis. To gain quantitative information about the frequency dependence of the observed absorption close to 2.75 T, we performed fits of the background-corrected data. The correction was performed assuming a polynomial shape (see orange dashed line in Fig. 3.20) of the transmission signal in a range of about 1.8-4.4 T. Corrected absorption data of three different frequencies is shown in Fig. 3.22. The experimental data was fitted using the superposition of two Gaussian peak functions. The absolute absorption of different measurements is not comparable, because of the different coupling at different frequencies, the different Q, which is also influenced by dielectric losses in the Herasil used, and the different crystal sizes which were studied. Due to thermal cycling, two single crystals broke during measurements and could not be used for further measurements. Moreover, the background approximation influences the peak height, as well as the ratio of the height of two peaks. It was possible to determine the center fields of the Gaussian lineshapes for each of the three frequencies. The center fields of the two lines approach going to lower frequency, from 0.93 ± 0.06 T at 14.26 GHz over 0.76 ± 0.06 T at 10.40 GHz to 0.49 ± 0.06 T at 7.36 GHz. The width of the peaks was between 0.3 T and 0.9 T. These large linewidths show that for frequencies well below the used 7.36 GHz it will not be possible any more to resolve the two lines. But at energies below the splitting energy the absorption will disappear.

To gain insight into the topography of the spin levels in proximity of the level crossing, we performed measurements at numerous frequencies between 7.36 GHz and 14.26 GHz. Below 7.36 GHz it was not possible to observe any transition any more, which is due to the lack of a low-loss dielectric with $n > 3$ in the experiment. All data was analyzed the same way as done for the three frequencies shown in Fig. 3.22. The resulting values for the resonance absorption are plotted in Fig. 3.23, values for the width of the peaks are given in Table 3.1. The width of the Gaussians was in between 0.3 T and 0.9 T, most lines were about 0.5 T broad. We measured two orientations: 0° is the orientation of the crystal with respect to $\vec{B}_0$ and $\vec{B}_1$ shown in Fig. 3.18. 90° is the orientation where $\vec{B}_0$ and $\vec{B}_1$ are aligned parallel to the largest face of the crystal. For all data points, including the data at 0° and 90°, a linear fit was performed to approximate the shape of the levels in the measured range. No evidence for an avoided crossing was found so far, therefore the splitting at the crossing field must be smaller than the measured 7.36 GHz. In Fig. 3.23 the green dotted line indicates the hypothetical behavior of the levels in the case of a real level crossing, whereas the green dashed line indicates the hypothetical behavior of the levels in the case of an avoided level

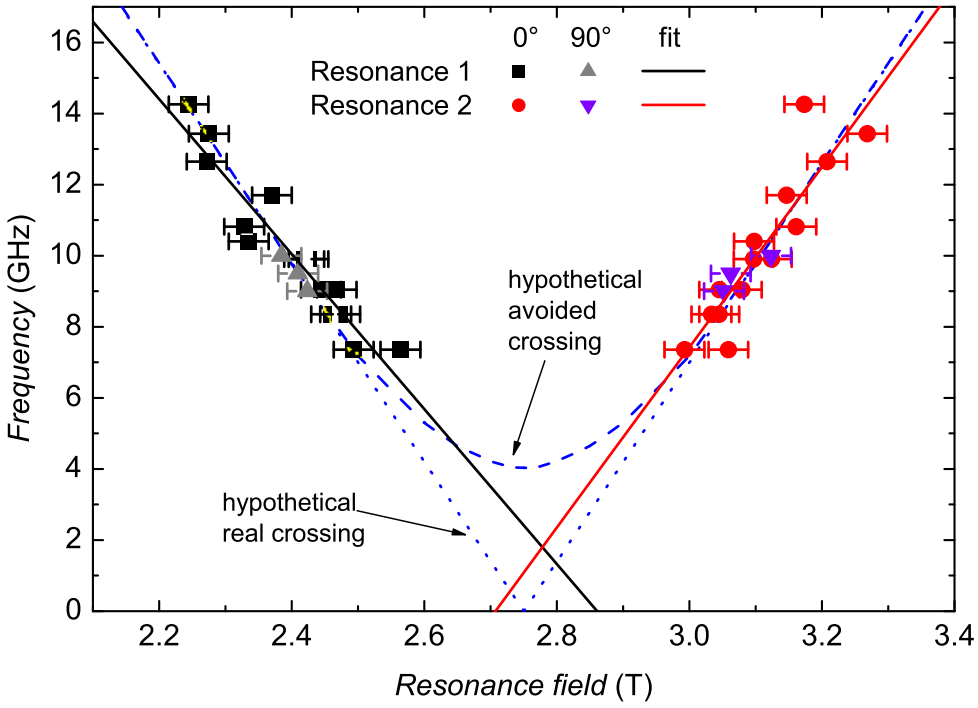

Figure 3.23: Frequency versus resonance field from fitting the absorption data with two Gaussian lineshapes. The data points for the Gaussians at high and low field were each fitted with a straight line, given in black and red. Blue dotted line: Hypothetical behavior of a system with a real crossing. Blue dashed line: Hypothetical behavior assuming an avoided crossing with a splitting of 4 MHz.

Table 3.1: Center fields and widths of transitions.

Frequency	Center Gaussian 1	FWHM 1	Center 2	FWHM 2
7.359 GHz	2.56 T	0.53 T	3.06 T	0.42 T
7.359 GHz	2.49 T	0.42 T	2.99 T	0.52 T
8.350 GHz	2.46 T	0.39 T	3.03 T	0.47 T
8.350 GHz	2.47 T	0.46 T	3.04 T	0.48 T
9.044 GHz	2.44 T	0.41 T	3.05 T	0.48 T
9.044 GHz	2.46 T	0.45 T	3.08 T	0.46 T
9.905 GHz	2.43 T	0.35 T	3.12 T	0.49 T
9.905 GHz	2.42 T	0.47 T	3.10 T	0.48 T
10.399 GHz	2.34 T	0.41 T	3.10 T	0.53 T
10.820 GHz	2.33 T	0.33 T	3.16 T	0.48 T
11.700 GHz	2.37 T	0.40 T	3.15 T	0.48 T
12.643 GHz	2.27 T	0.37 T	3.21 T	0.38 T
13.434 GHz	2.27 T	0.25 T	3.27 T	0.38 T
14.529 GHz	2.24 T	0.45 T	3.17 T	0.96 T

crossing with a splitting of 4 GHz. The available experimental data alone cannot distinguish between the two cases.

Discussion. Both Dzyaloshinskii-Moriya (DM) interactions $\left(H = \sum_{i,k} \mathbf{D}_{ij} \cdot [\mathbf{S}_i \times \mathbf{S}_k]\right)$, and hyperfine interaction between the electron spin and the $I = 7/2$ nuclear spin of ^{51}V $\left(H = A \sum_{i=1}^{3} \mathbf{I}_i \mathbf{S}_j\right)$ can mix the $S = 1/2$ and $S = 3/2$ spin multiplets. Therefore, the non-negligible transition probability in between these to multiplets shows, that at least one of these interactions must be present. No evidence for a strong deviation from a real crossing behavior of the levels was found in the presented measurement data. Therefore, the splitting at the crossing field has to be smaller than the measured 7.36 GHz. In consequence, no quantitative analysis of the influence of DM or hyperfine interactions can be performed.

It was possible to observe a quantitative dependence of the energy difference of the $S = 1/2$ and $S = 3/2$ in the crossing region. This result is analogous to the results of del Barco *et al.* [7], discussed in Chapter 3.1, whereas in the case of [7] the levels were mixed applying a rather strong perturbation to the system by the application of a strong transverse field, whereas the mixing between the spin

multiplets presented here is a property of the system which has not to be tuned by an external parameter.

3.5 Summary and Perspectives

We successfully developed a high-sensitivity broadband ESR setup for the frequency range of 5-40 GHz. It is optimized for broad absorption lines, due to the very wide field range (0-10 T) and the possibility to sweep the magnet with a high rate. In future, it will be useful to investigate the use of high ϵ dielectrics for the extension of the frequency to the lower end. Also for other compounds, where single frequency ESR normally leads to complicated spectra, like in rare-earth systems, the in-situ multifrequency approach may be useful. Applications of the setup other than multifrequency ESR measurements include any field dependent absorption measurements in the accessible frequency range.

Performing measurements on V_{15} for lower frequencies than the used 7.36 GHz, it will be possible to gain detailed information about the level crossing. With the knowledge of the topography of the level crossing and the energy splitting Δ, it will be feasible to design an experiment to use pulsed microwave radiation to manipulate the superposition state coherently. The coherent manipulation of this superposition state is the prerequisite for any quantum computation operation in these systems.

Chapter 4

Quantum Coherence in the Antiferromagnetic Ring Cr_7Ni

Abstract. In this chapter, we present CW and pulsed W-Band ESR investigations on a $S = 1/2$ molecular magnet, the antiferromagnetic ring Cr_7Ni. We show that the ESR properties of Cr_7Ni are preserved in solution, which makes it possible to study its intrinsic coherence properties in dilute frozen solutions. Thereby we limit magnetic dipolar interactions which would lead to a fast decay of coherence. We report intrinsic spin-lattice and phase-coherence relaxation times of Cr_7Ni at an external field of $B = 3.85\,\mathrm{T}$. Moreover, we find dominating decoherence mechanism in the coupling of the electron spin to protons within the molecule by using pulsed ENDOR. Surprisingly, no coupling to ^{19}F nuclear spins was observed. These results broaden the knowledge about coherence processes in molecular magnets. This understanding is also a prerequisite for the deliberate design of magnetic molecules for quantum information processing applications.

4.1 Introduction

The world around us is classical, even though the fundamental laws of physics are based on quantum mechanics. The transition between the quantum and the classical world has drawn a lot of attention, recently (see Chapter 1.6). Molecular magnets are ideal systems to study this transition, because on the one hand in these systems quantum properties were observed quite early (see Chapter 1.3), but at the same time they consist of numerous atoms bringing them closer to a classical, i.e. mesoscopic system. While magnetization-relaxation in molecular magnets was extensively studied, only a few studies of coherence were reported: In iron-sulfur clusters, T_2 is several hundreds of nanoseconds [55] [56] [57]. In Cr_7Ni, $T_2 = 397\,\mathrm{ns}$ at $4.5\,\mathrm{K}$ and $0.4\,\mathrm{T}$; deuterated samples showed increased values of up to $T_2 = 3.8\,\mu\mathrm{s}$ at $1.8\,\mathrm{K}$ [3]. In an iron (III) trimer, T_2 was found to to be $2.6\,\mu\mathrm{s}$ at

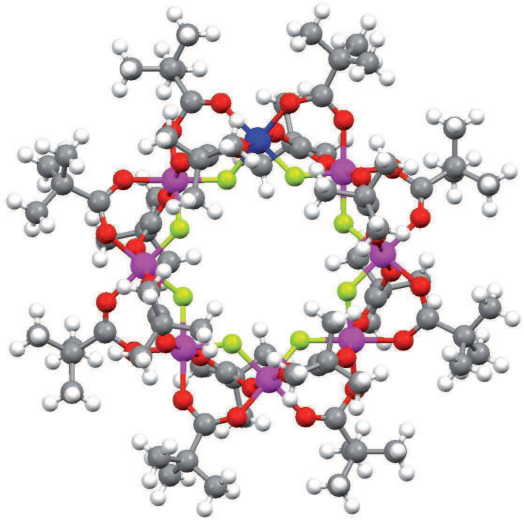

Figure 4.1: Cr_7Ni molecule as seen from the molecular c axis. Cr: purple, Ni: blue, F: green, O: red, C: grey, H: white.

0.35 T, and was temperature independent below 7 K [17]. In V_{15}, $T_2 = 0.8\,\mu$s for the ground state $S = 1/2$ and $T_2 = 0.34\,\mu$s for the excited $S = 3/2$ state, both values were determined at 4 K and $B_0 \approx 0.4$ T.

The molecular magnet studied in this chapter is the complex $[Cr_7NiF_8(O_2CCMe_3)_{16}]$, abbreviated Cr_7Ni. The transition metal ions Cr and Ni are coupled antiferromagnetically, this leads to a $S = 1/2$ ground state.

In addition to the mesoscopic properties of molecular magnets it is also interesting to take a look at potential applications. Cr_7Ni was proposed to be a suitable candidate for quantum information processing, because of the relative decoupling from the environment, the possibilities to change properties deliberately by supramolecular chemistry and the larger physical dimension of the system than in single-spin encodings. In the following, we will propose practical ways how to implement molecular magnets in this application. A broader overview is provided in the article of Affronte [58].

Troiani *et al.* [24] proposed to use a collection, e.g. a planar array, of coupled molecules, each representing a different qubit. The ground state ($S = 1/2$) being well separated ($\Delta \approx 13$ K) from excited states shows the suitability to use this two-level system as a qubit [24]. At the same time, the excited states can be used as resources for quantum gate implementation with one or more qubit. Moreover, the symmetries of the ground state of Cr_7Ni with its low S mixing suppress the

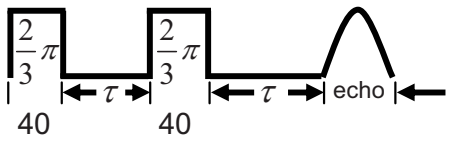

Figure 4.2: Applied primary Echo sequence with equal pulse lengths.

coupling to excited spin levels. If this coupling would not be suppressed, the transverse field necessary for quantum-gate implementations would lead to population loss (leakage). Recently, it was shown that two Cr_7Ni molecules can be chemically linked to each other and that the coupling between these two $S = 1/2$ systems can be tuned depending on the linker [25].

Here we show the first measurements of relaxation and coherence times in Cr_7Ni at W-band frequencies ($\approx 94.3\,\mathrm{GHz}$). It is important to identify the processes relevant for spin-lattice relaxation and decoherence. Some of these processes are frequency and field dependent; thus a study at about 10 times the frequency compared to the study [3] eludicates the origin of the relaxation processes. With the information gained, one can deliberately change molecular properties and choose experimental conditions suitable for quantum information operations.

4.2 Experimental Methods

4.2.1 Hahn Echo and Inversion Recovery

To determine the phase coherence time T_2^*, the primary echo sequence (Chapter 2.2.2) was used. Here, we applied a sequence with two equal pulse lengths (Fig. 4.2), which were optimized for maximum echo intensity. Because the normalized echo intensity I_{echo} of two pulses with arbitrary flip angle β is $I_{\mathrm{echo}} = |\sin(\beta)| \sin^2(\beta/2)$ [9], I_{echo} is maximum for $\beta = 2/3\pi$, the experimental pulse length corresponds to a $2/3\pi$-pulse. The $2/3\pi$-pulse lengths varied from $40-60\,\mathrm{ns}$, dependent on microwave cavity coupling and sample.

4.2.2 Mims ENDOR

To be able to observe a pulsed ENDOR signal in dilute solution with short relaxation times, different parameters have to be optimized.

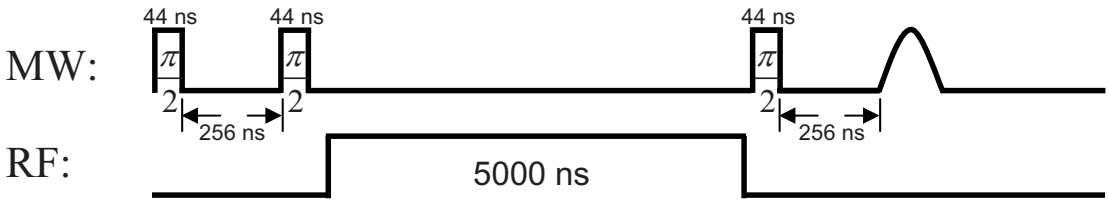

Figure 4.3: Applied Mims-ENDOR sequence including optimized pulse lengths.

Because T_1 was found to be $T_1 \approx 3\,\mu$s in Cr_7Ni at 4.5 K (see Chapter 4.3.2), the Mims-ENDOR sequence cannot be used with a RF π-pulse length of $\pi \approx 30\,\mu$s, which would be advantageous to reach a maximum difference in echo signal in the case of resonance. Therefore the RF pulse length was shortened. Applying a RF pulse with a length of only $\pi/6$ ($5\,\mu$s) reduces the change in echo due to polarization transfer at the proton Larmor frequency tremendously. Compared to the maximum possible difference in echo signal (Equation 2.10), the observed difference in echo signal is $\frac{V_{\pi/6}}{V_0} = \frac{2-\sqrt{3}}{4} \approx 6.7\%$.

To be able to perform a significant number of shots, but at the same time to exclude heating effects playing a role, we decreased the shot repetition time τ_{rep} until no change in echo intensity was visible any more. This was the case for $\tau_{\text{rep}} \geq 15\,$ms, therefore this time was used in the measurement. The pulse separation τ (see Fig. 2.3) was reduced to a value which led to negligible influences of the last pulse and allowed to integrate solely the echo intensity. Applying the optimized parameters for RF pulse length, repetition time and pulse separation τ, a MIMS ENDOR measurement was possible in a timescale in which the setup stayed sufficiently stable. The optimized pulse sequence is shown in Fig. 4.3.

4.3 Results and Discussion

4.3.1 CW and Echo Detected W-Band ESR Measurements

To ensure, that subsequent pulsed measurements quantify properties of the sample itself, we will compare the field-dependence of the CW spectrum with the echo-detected one. By that, one can deduce whether the same species was excited both in CW and pulsed measurements.

We performed CW W-Band ESR on Cr_7Ni in toluene (concentration: 1 mg/ml) from 0-4.5 T. Besides the signal of paramagnetic impurities around $g = 2$ an ESR signal, which we assign to the sample, was found around 3.84 T; this signal is

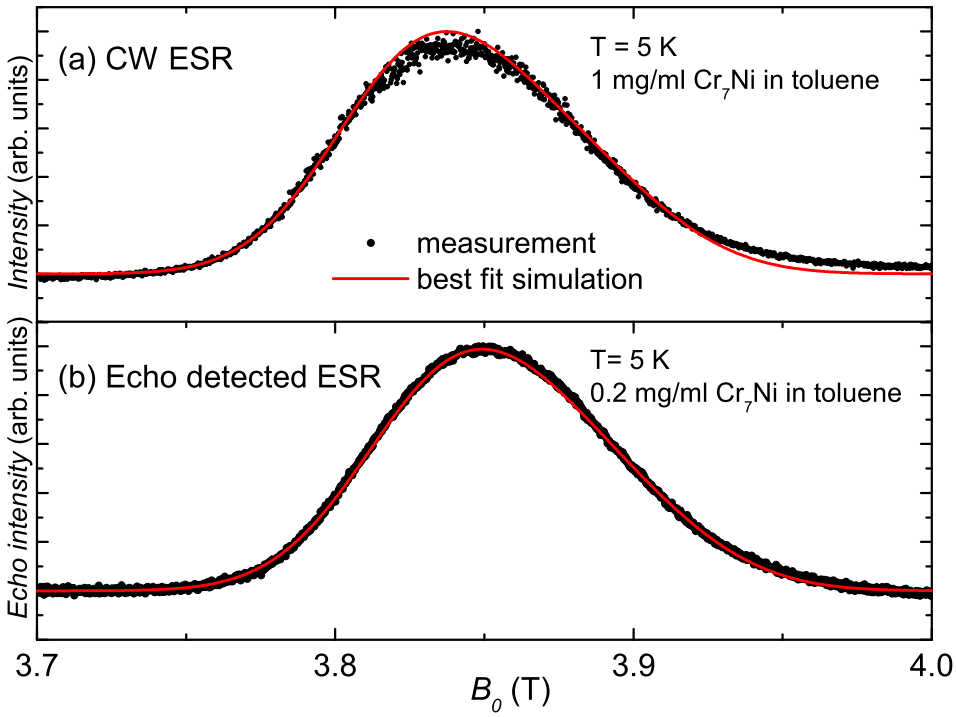

Figure 4.4: Echo detected ESR and CW ESR on solutions of Cr_7Ni. Both measurements were simulated using easyspin. The slight difference in the line positions is due to different experimental frequencies (see text).

shown in Fig. 4.4(a). The experimental parameters were: Microwave frequency $f = 94.238\,\mathrm{GHz}$, maximum microwave power (200 mW) and 1 G modulation amplitude. We observe a slightly asymmetric line centered around 3.84 T.

Echo detected ESR measurements were performed using a $2/3\pi - \tau - 2/3\pi - \tau -$ echo ($2/3\pi$-pulse length: 40 ns) sequence (Fig. 4.4(b)) at 94.269 GHz.

Analysis. The CW-ESR data was simulated using the easyspin package [59]. Here, we fitted an easyspin simulation to the experimental spectra using the function esfit, which includes least-square fitting techniques. For the simulation we assumed a Gaussian distribution of g-values and a $S = 1/2$ spin system. Surprisingly, the experimental CW-ESR spectrum shows the shape of an absorption spectrum, despite the fact that field modulation was applied. We assign this to a phase offset in the ESR measurement. Therefore the simulation was performed using the 0th harmonic. The best-fit parameters for the simulation were a linewidth of 66.5 mT and an anisotropic g-value of $g_x = g_y = 1.764$ and $g_z = 1.723$. The g-value anisotropy is necessary to account for the asymmetric lineshape of the spectrum. Comparing the obtained data to values of powder samples from literature ([60] and [61]: $g_{xy} = 1.781$ and $g_z = 1.740$) shows the same ratio $g_{xy}/g_z \approx 1.02$, but a slightly different absolute value. In the presented measurement the magnetic field was not calibrated, which explains the deviation in absolute value and the, at the same time, correctly determined ratio. The reproduced g-values in solution show, that also the vector coupling approach presented in [60] can be used to explain the low g-value.

Fitting the echo-detected ESR data with the same procedure as for the CW-data, we obtained a linewidth of 70.0 mT and an anisotropic g-value of $g_x = g_y = 1.759$ and $g_z = 1.722$. Because the XEPR software does not correct the field reading for the current, which bypasses the superconducting magnet by the normal conducting switch heater in an echo detected measurement, the field reading does not correspond to the exact actual field. Therefore the B_0 axis is shifted, dependent on sweep speed. In consequence, the obtained values have an offset which is higher than for the CW data.

The CW and echo detected ESR spectra of Cr_7Ni in solution show the same lineshape within the error. Therefore, we conclude that in the following pulsed measurements around 3.85 T we truly study the coherent properties of Cr_7Ni in solution. Moreover, we can conclude from the similar lineshape, that T_2 remains virtually constant over the whole linewidth, which supports the observation of [3] that no variation of T_2 dependent on excited subpopulation is observed.

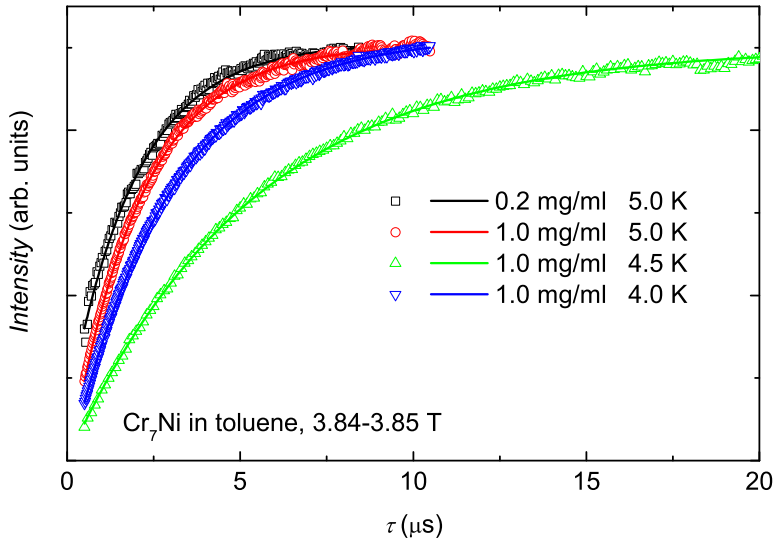

Figure 4.5: Inversion recovery measurements on Cr_7Ni in toluene at different temperatures and concentrations. The experimental data (symbols) were fitted monoexponentially (lines).

4.3.2 Relaxation and Coherence Measurements

Previous estimates of T_1 of exchange coupled clusters [62] from the direct spin-phonon process lead to a dependence on ESR frequency f of $T_1 \propto 1/f^3$. To investigate if this estimation holds for Cr_7Ni, we performed inversion recovery measurements to determine T_1 at 94.3 GHz. Fig. 4.5 shows the integrated echo intensity after a $\pi - \tau - 2/3\pi - \tau_{\text{fixed}} - 2/3\pi - \tau_{\text{fixed}} -$ echo sequence for different temperatures (4.0, 4.5 and 5.0 K) and different concentrations (0.2 mg/ml and 1.0 mg/ml). Even though only temperatures in a narrow range were chosen, the inversion recovers much more slowly for lower temperatures (see analysis below). To investigate if coherence times of Cr_7Ni at 3.84 T (W-Band ESR) are comparable to the ones at 0.4 T (X-Band ESR) [3], a Hahn echo measurement was performed (Fig. 4.6). We employed the sequence $2/3\pi - \tau - 2/3\pi - \tau -$ echo (Chapter 4.2.1) at a temperature of 5.0 K on a frozen solution of Cr_7Ni in toluene with a concentration of 0.2 mg/ml. Below this dilution results were concentration independent [3].

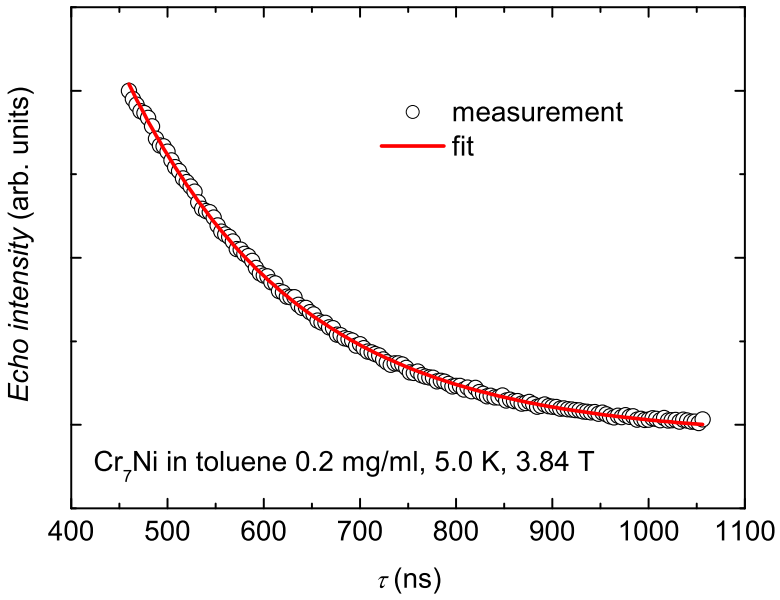

Figure 4.6: Integrated echo intensity for Cr_7Ni in toluene. The experimental data (symbols) were fitted monoexponentially (line).

Temperature	Concentration	T_1
$5.0 \pm 0.1\,\mathrm{K}$	$0.2\,\mathrm{mg/ml}$	$2.0 \pm 0.1\,\mu\mathrm{s}$
$4.0 \pm 0.2\,\mathrm{K}$	$1.0\,\mathrm{mg/ml}$	$5.3 \pm 0.2\,\mu\mathrm{s}$
$4.5 \pm 0.1\,\mathrm{K}$	$1.0\,\mathrm{mg/ml}$	$2.9 \pm 0.1\,\mu\mathrm{s}$
$5.0 \pm 0.1\,\mathrm{K}$	$1.0\,\mathrm{mg/ml}$	$2.0 \pm 0.1\,\mu\mathrm{s}$

Table 4.1: T_1 values of Cr_7Ni at different concentrations and temperatures.

Analysis. To determine relaxation times T_1, all inversion recovery datasets were fitted with an exponential decay function $1-e^{-\tau/T_1}$. The resulting relaxation times are shown in Table 4.1. The relaxation times for the concentrations 0.2 mg/ml and 1.0 mg/ml were the same, that means that for T_1 the dipole-dipole interaction does not play any role in this dilution. Going from 5.0 K to lower temperatures, T_1 of Cr_7Ni in toluene increases dramatically. The values obtained in this study at 94.3 GHz are close to the ones obtained by Ardavan *et al.* at 9.8 GHz (from [3]: 3.6 K: $T_1 \approx 4\,\mu$s, 4.5 K: $T_1 \approx 3\,\mu$s). This means that the direct process suggested for spin-lattice relaxation [62] is not dominant at the measured temperatures and frequencies. Both the two-phonon Orbach and Raman processes are independent of frequency [63] [13], and could therefore explain the observed relaxation times. To distinguish these two processes, a study of the temperature dependence of T_1 is necessary. Here, we cannot perform this study, because exciting different parts in the spectrum reveals a variation of a factor of about two in T_1 at low temperatures [3].

The echo decay data were fitted with an exponential decay function $Ae^{-2\tau/T_2^*} + B$, which led to a T_2^* of 357 ± 10 ns. This coherence time is close to literature values [3] obtained at 0.4 T, where a coherence time of 379 ns at 4.5 K was found. The dominant decoherence path is most likely the coupling of the electron spin to the nuclear spins in the surrounding [3]. Upon polarization of the nuclear spins by an external magnetic field, spontaneous spin flip-flop processes inducing coherence are suppressed. Still, similar coherence times at 0.4 T and 3.85 T are not surprising, because the polarization of the nuclear spin bath is negligible for the applied fields. This is analogous to the situation in Chapter 6.3.1, where also protons are the reason for spin-bath decoherence. Moreover, a limitation of T_2^* by T_1 can also be excluded because the relaxation time is about one order of magnitude longer than the coherence time.

No significant modulation in echo amplitude was observed in the Hahn echo,

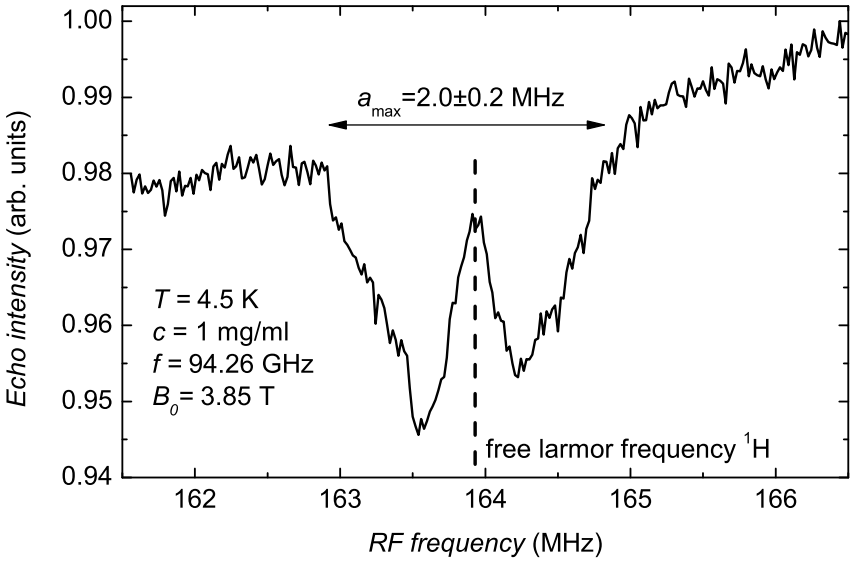

Figure 4.7: Mims-ENDOR of Cr_7Ni.

like it could be expected for electron spins in the vicinity of nuclear spins due to ESEEM (Chapter 2.2.4). This is due to the low modulation depth at high magnetic fields. Therefore ENDOR measurements (see Chapter 4.3.3) were performed to determine electron-nuclear couplings.

4.3.3 Mims ENDOR Measurements

To determine and quantify couplings of the electron spin system to the nuclear spins, we performed pulsed ENDOR measurements. The echo amplitude after a Mims ENDOR sequence (Fig. 2.3) with a $\pi/2$-pulse length of 44 ns in a frequency range of 161.5-166.5 MHz is shown in Fig. 4.7. To increase the low echo intensity, a concentration of 1 mg/ml was used.
Measurements at other RF frequencies, particularly around the free Larmor frequency of ^{19}F, did not show any detectable ENDOR intensity.

Analysis. The observed spectrum shows the expected two lines for a $S = 1/2$ coupled to an $I = 1/2$ (see Chapter 2.2.5), centered around the free Larmor frequency of protons at 3.85 T (163.92 MHz). Thus, we observe the weak hyperfine

coupling of the coupled electron spin system to surrounding protons. The broad ENDOR lines indicate many, different hyperfine couplings. We assign this to the nonequivalent bound protons in the pivalate, which are located at different distances to the electron spin system.

To verify the observed coupling to protons, we performed a second measurement at 3.885 T, which is still within the ESR linewidth. The observed ENDOR signal was now centered around 165.4 MHz, so it shifted due to the increased external magnetic field. This verifies the nature of the ENDOR line being the signature of the coupling of the electron spin to ^{1}H nuclear spins.

A quantitative analysis of the ENDOR spectra was performed by simulating the ENDOR spectrum using the easyspin package [59]. To do so, ENDOR intensity was corrected for a background, assuming a polynomial (second order) background for the measured range. In the simulation, the parameters a (isotropic hyperfine coupling) and the linewidth $\mathrm{FWHM_{ENDOR}}$ were varied. The best agreement between simulation and measurement (Fig. 4.8) was achieved for $a = -0.8 \pm 0.05\,\mathrm{MHz}$ and $\mathrm{FWHM_{ENDOR}} = 0.55 \pm 0.05\,\mathrm{MHz}$, not accounting for temperature-dependent effects. When these are accounted for by using a Boltzmann population of the levels as for the experimental temperature of 4.5 K, the two lines do not show the same intensity any more. The resulting intensity ratio between the high and low frequency peaks is much lower than in the experimental results. Because the lineshape does not exactly follow a Gaussian distribution (again not considering temperature-dependent effects), therefore we analyze the hyperfine interaction in detail:

For a dipolar nature we can calculate the isotropic hyperfine interaction using [64]

$$a(\theta) = g_e \mu_e g_n \mu_n (3\cos^2\theta - 1) d^{-3} h^{-1}.$$

Herein g_e and g_n are the g-factors of the electron spin and the nuclei, respectively, and μ_e and μ_n the Bohr magneton and the nuclear magneton, respectively. θ is the angle between the magnetic field and the electron-nuclear spin connection axis, and d is the distance between the spins.

In the following we will estimate the maximum a which can be expected for electron spin to proton dipolar coupling in Cr_7Ni. To do so, we determined the closest proton to the one paramagnetic center (see Fig. 4.9), which is about 0.404 nm. We expect a statistical distribution of angles, because the measurement was performed on a frozen solution. Therefore, the maximum coupling is expected for $\theta = 0$. In this case, $a_{\max} \approx 2.1\,\mathrm{MHz}$. This value fits well to the experimentally

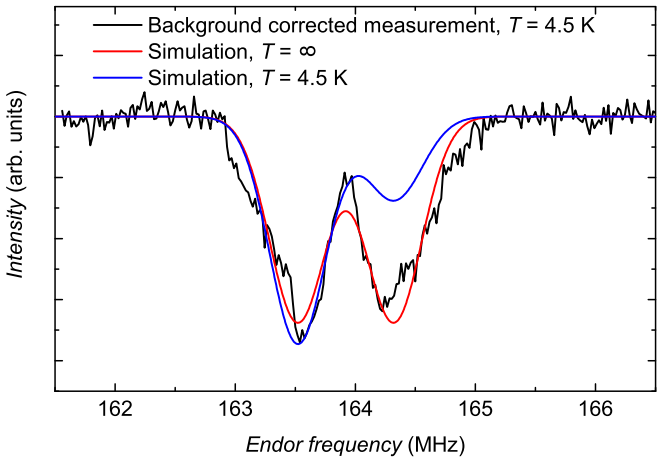

Figure 4.8: Simulation of background corrected ENDOR intensity using easyspin.

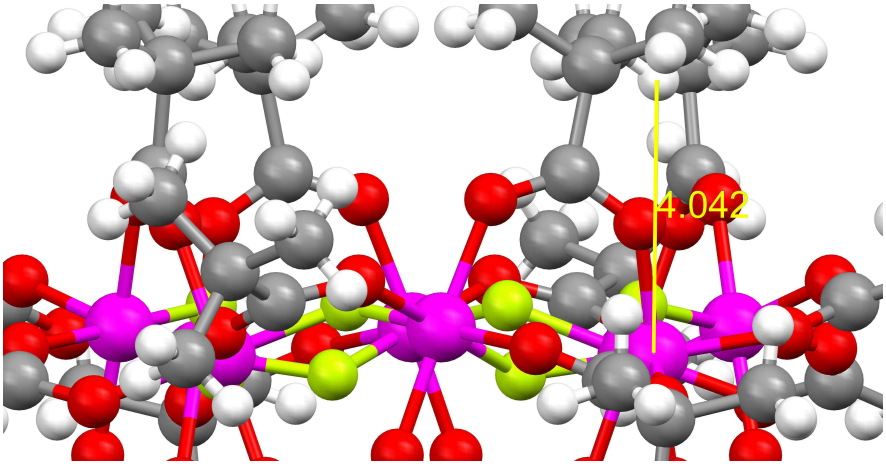

Figure 4.9: Determination of shortest Cr-H distance for calculation of dipolar hyperfine interaction.

observed $a_{\max} \approx 2.0 \pm 0.2\,\mathrm{MHz}$ (see Fig. 4.7). For longer distances statistically there are more protons, which leads to higher ENDOR intensities for frequencies closer to the proton Larmor frequency.

Surprisingly, at the nuclear Larmor frequency of ^{19}F, no hyperfine coupling in a comparable coupling strength to the one of ^{1}H was detected. If a a broad distribution of strong coupling strengths would be present, it would be not possible to detect the signal. The molecular structure shows, that the distance from the ^{19}F atoms to the electron spin system is comparable for all ^{19}F atoms. Thus, no broad distribution is expected. Studies on the decoherence times by Ardavan *et al.* [3] showed, that decoherence times increased significantly for deuterated samples compared to nondeuterated ones. This shows, that the nuclear spins of F do not crucially limit the decoherence times. The hyperfine coupling to ^{14}N could not be investigated, due to experimental limitations of the ENDOR frequency.

4.4 Conclusion

We were able to determine that the main decoherence path is the hyperfine coupling to intramolecular protons. Therefore polyoxometalates, which can principally be nuclear spin free, can provide a way to reach much longer coherence times. The presented results show that T_2^* is not limited by T_1 in Cr_7Ni, but deliberately synthesizing molecules with fewer nuclear spins could lead to an upper limit for T_2^*. To understand the influence of the phononic bath provides a first step to overcome this limitation.

ENDOR proved to be a suitable method to reveal electro-nuclear couplings for Cr_7Ni. Moreover, in the future ENDOR techniques could be used also for coherent manipulation in the case of quantum information processing: It could be possible to prepare pseudoentangled states of the coupled spin system. For the practical realization of this task narrower linewidths, that means single crystal samples with nuclear couplings to specific sites, would be desirable. Including the nuclear spin in quantum information processing opens the possibility to store information in the nuclear spin system, which possesses much longer coherence times in many cases.

Chapter 5

Magnetic Properties of Two Fe_4 Single-Molecule Magnets

Abstract. We present comprehensive studies of the magnetic properties of two new Fe_4 single-molecule magnets ($S = 5$). We determined exchange coupling constants between the single ions using DC susceptibility measurement. Slow relaxation of magnetization was observed by AC susceptibility measurements. Moreover, single-molecule magnet properties are found to be preserved in solution, as determined by AC susceptibility measurements. Interestingly, we observed an enhancement of the effective energy barrier in frozen solution. This change in axial zero-field splitting supports the crucial dependence of the magnetic anisotropy in Fe_4 clusters on structure. In solution the local environment is changed, which also is expected to induce local distortions in the molecules. Magnetic resonance methods enabled us to quantify zero-field splitting parameters with a high precision.

5.1 Introduction

The goal of the investigations presented in this chapter is the comprehensive study of the magnetic properties of two new Fe_4 compounds in both powder and solution, to determine how much the magnetic properties are determined by the surrounding. The compounds are $[Fe_4^{III}(acac)_6(Br\text{-}mp)_2]$ **(1)** and $[Fe_4^{III}(acac)_6(tmp)_2]$ **(2)**, both of which have a propeller-like structure (see Fig. 5.1). The synthesis of these two exchange coupled clusters is described in [65].

Studies on molecular magnets in solution or in polymer matrices are rare, and most of them deal with manganese based SMMs [66] [67] [68]. Nevertheless, investigations on SMMs in solution are interesting for several reasons: First, in solution, single-molecule magnet properties show to advantage, because they are properties of the single molecules rather than the ones of an ensemble [16]. There-

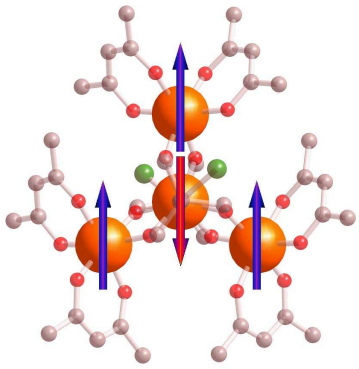

Figure 5.1: Molecular structure of $[Fe_4^{III}(acac)_6(Br\text{-}mp)_2]$ **(1)** with iron atoms depicted as large orange spheres. The arrows denote the relative orientation of the mangetic moments of each iron ion in the $S = 5$ ground state.

fore, even if molecules are not arranged in a single crystal structure, comparable magnetic properties can be observed. Surprisingly, for two Mn_{12} derivatives, the magnetization relaxation times changed significantly [69] [70], whereas for Mn_{12}Piv relaxation times were comparable in powder and solution [66]. Second, the influence of dipolar interactions can be studied by the concentration, and thus the intermolecular distance. Normally, dipolar interactions are neglected as a first approximation for the description of magnetic properties of molecular magnets. Moreover, it is interesting to study the dependence of the anisotropy on the surrounding and the resultant structural parameters.

To our knowledge this is the first study on solutions of members of the Fe_4 family. For other Fe_4 compounds it was shown, that the helical pitch plays a crucial rule for the value of the axial zero-field splitting parameter D. In solution, the molecular structure may be distorted, this distortion then could be seen in a change in D. It is interesting to study the magnetic properties, in oder to gain information of how much the magnetic properties are influenced by the surrounding. Other studies of Fe_4 molecules in different surroundings were not able to study magnetic properties in detail: Magneto-optical studies in different polymeric environments were published by [71]. Recently efforts in anchoring Fe_4 compounds were successful [72] [73], in monolayers magnetic hysteresis could be shown [73].

A broad variety of techniques, namely frequency domain magnetic resonance spectroscopy (FDMRS), continuous wave (CW) W-Band ESR and DC and AC

susceptibility measurements, were applied to study the magnetic properties of **(1)** and **(2)**. Hereby DC suscpeptibility measurements allow to quantify exchange coupling constants in between the single ions in the compounds. Additionally effects of zero-field splitting can be observed. AC susceptibility measurements can reveal information about the effective energy barrier and can help to determine whether quantum tunneling plays a role in the relaxation process. FDMRS is an elaborate technique to study systems with a high zero-field splitting. It allows us to study magnetic transitions in a range of 30-1500 GHz, which is the relevant energy range for magnetic transitions of exchange coupled high-spin systems. Zero-field splitting (ZFS) parameters can be determined directly, in contrast to conventional field-swept high-field ESR, where this is only possible by extrapolation from finite magnetic fields. CW W-Band ESR operates at 94 GHz, therefore it is possible to observe the ground state transition of $S = 5$ systems with an axial zero-field splitting with values of D up to -0.35 cm^{-1}. The high sensitivity of the setup enables us to perform measurements on diluted solutions.

5.2 Experimental Methods

5.2.1 Susceptibility Measurements

For susceptibility measurements on powders in the SQUID (Quantum Design MPMS-XL 7), the crushed powder sample was wrapped in teflon tape. Afterward it was pressed to obtain a rugged cylindrical disc with a diameter of 5 mm. For the preparation of frozen dilute solutions the mass of crushed powder of **(1)** brought into small glass containers was weighed. The appropriate amount of solvent needed for the desired concentration was given into the container using adjustable pipettes from Eppendorf. Solutions with concentrations of 0.5 mg/ml and 5.0 mg/ml were prepared. Then the glass container was agitated until no powder was visible any more (less than one minute). This shows that all concentrations chosen were clearly below the saturation concentration of Fe_4 in these solvents at room temperature. The solutions were filled into gel capsules and sealed with cyanacrylate glue. Directly after preparation the solution was inserted into the magnetometer and thermally quenched to 4.2 K. AC susceptibility measurements

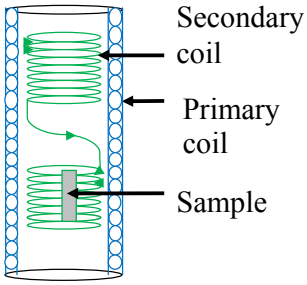

Figure 5.2: Arrangement of coils in a typical AC susceptometer (from [74]).

at ultra-low temperatures were performed in the setup described in Chapter 5.2.2. Here powder sample was brought into the sample holder using grease.

Susceptibility data obtained in the commercial Quantum Design MPMS-XL 7 SQUID and the PPMS (Physical Properties Measurement System) were used for discussion without data processing. For the DC susceptibility measurements the magnetic data were corrected for the diamagnetic contribution calculated from Pascal's constants. In contrast, for measurements in the non-commercial AC susceptometer used for the measurements at ultra-low temperatures (general characteristics were described in Chapter 5.2.2), the following data processing procedure was performed:

The setup exhibits an intrinsic phase shift. This phase shift was first measured for each frequency by directly connecting the sine out (50 mV) to the lock-in input. The obtained values for the phase shift were used to calculate phase corrected values for χ' and χ''. After this, the data was normalized for each frequency. To do so, the data for χ' at high temperatures, where a linear behavior is expected, was compared to reference data. Absolute data obtained from SQUID and PPMS measurements at the same frequencies was used to provide the reference. This procedure does not only allow us to obtain values which have the right order of magnitude in absolute values, at the same time it corrects for the frequency dependent ($\propto f$) sensitivity of the setup.

5.2.2 AC Susceptometer at Low Temperatures

To measure the magnetic susceptibility of a material, and thus for example to determine the barrier against magnetization reversal, an AC susceptometer can be used. In the following, we will discuss the principle of such a susceptometer on basis of the setup used in Chapter 5. Applying an altering current $I = I_0 e^{i\omega t}$

to a primary coil (see Fig. 5.2) leads to a small altering magnetic field inside. Because the secondary coil is located within the primary coil, the magnetic flux Φ through both is the same. The secondary coil changes the winding direction at half the length of the coil. The sample (with relative permeability μ_r) is inserted in only one section, which we call section (a), in contrast to section (b) in which no sample is introduced. The voltage induced in the secondary coil U_{total} is:

$$\begin{aligned} U_{\text{total}} &= U_a + U_b && (5.1)\\ &= -L_a \frac{\partial I(T)}{\partial t} + L_b \frac{\partial I(T)}{\partial t} && (5.2)\\ &= -(L_a - L_b)\mathrm{i}\omega I_0 e^{\mathrm{i}\omega t} && (5.3)\\ &= -(\mu_r - 1)\mu_0 n^2 A/l(\mathrm{i}\omega I_0 e^{\mathrm{i}\omega t}) && (5.4)\\ &= -\chi\mu_0 n^2 A/l(\mathrm{i}\omega I_0 e^{\mathrm{i}\omega t}) && (5.5) \end{aligned}$$

We used the formula for the inductance of a long coil ($L = n^2\mu_0\mu A/l$) with n being the number of windings, μ_0 and μ_r being the vaccum and relative permeability, respectively, A being the cross section, and l the length of the coil. Moreover, the relationship between susceptibility χ and relative magnetic permeability μ_r ($\chi = \mu_r - 1$) was employed.

The calculation shows, that the measured induced voltage is directly proportional to the susceptibility. The prefactor includes $\mathrm{i}\omega$, which means that the recorded signal is phase shifted by $\pi/2$ (the real part of the measured voltage is $\propto \chi''$, and vice versa), and that the intensity is $\propto \omega$.

In the measurements presented in Chapter 5, a non-commercial setup at the University of Zaragoza was used. This setup is incorporated in a dilution refrigerator, making it possible to study the AC susceptibility from 0.1 K upwards. Above the transition temperature from superconducting to normal conducting state for the AC coil material, the signal is not comparable to the low-temperature signal anymore. This sets an upper limit of the usable temperature range at about 2-3 K. In principle a broad range of frequencies can be set. To low frequencies, the signal intensity being $\propto \omega$ limits the practical frequency range, to high frequencies resonances and radiative losses give the frequency limit.

5.2.3 FDMRS and W-Band ESR

For FDMRS measurements (Chapter 2.3.3) powder of **(1)** and **(2)** was pressed into plane parallel samples as follows: The powder was crushed and then mixed

with eicosane ($C_{20}H_{42}$). The eicosane was added to obtain a less brittle sample and therefore to avoid fractures. Eicosane does not show any noteworthy absorption in the FDMRS frequency range of 30-1500 GHz. 59.8 mg of **(1)** were mixed with 24.4 mg of eicosane, whereas 33.8 mg of **(2)** were mixed with 25.3 mg of eicosane. Then, mixtures were pressed into plane parallel pellets with a diameter of 10 mm and thicknesses of 0.85 mm **(1)** and 0.67 mm **(2)**. The used pressure was about 0.5 GPa. At this order of magnitude of pressure the distortions in the molecule may lead to a small variation of D in SMMs ([75]: <4% variation in D for Mn_4Br and Mn_{12}-acetate), and changes in the coupling scheme are not expected. Moreover, upon release of the pressure the distortions are expected to vanish.
For W-Band ESR measurements (Chapter 2.4) crushed powder was put directly into quartz sample tubes with beaded bottom, having an outer diameter of 0.9 mm and an inner one of 0.5 mm.
Solutions of **(1)** and **(2)** were prepared according to the procedure described in Chapter 5.2.1. Using a quartz capillary the solution was transferred immediately into W-Band sample tubes. These were flame-sealed to avoid solvent evaporation, due to the low pressures inside the cryostat, during the cooldown procedure. After sealing, the tubes were inserted into the precooled cryostat and cooled down to the desired temperature.

In ESR measurements, the field range from 0 T up to 4 T was covered by sweeping the superconducting magnet. The magnetic field step size was 0.33 mT and the field modulation amplitude 0.1 mT. Coupling of the cavity was only possible for a very small fraction of the sample being present in the cavity, otherwise microwave absorption led to a low quality factor of the cavity.

5.3 Results and Discussion

5.3.1 DC and AC Susceptibility

Using DC and AC susceptibility measurements it is possible to quantify the effective energy barrier against magnetization reversal and to identify relaxation paths in powder samples and in solution. AC susceptibility measurements will enable us to evaluate whether the SMM properties of **(1)** are preserved in solution.

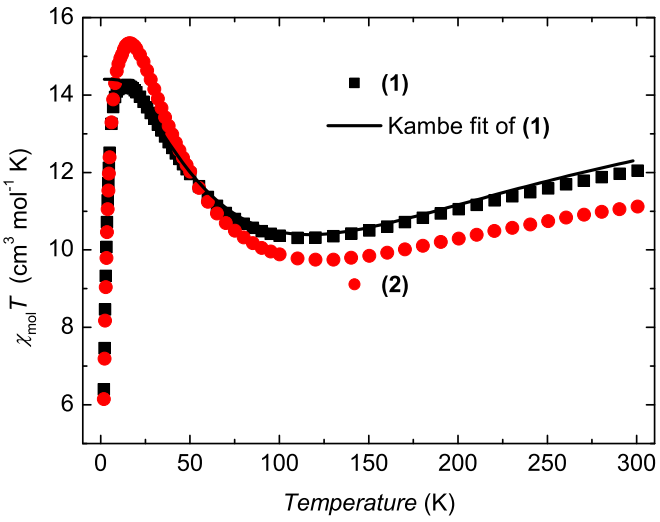

Figure 5.3: Plot of measured DC susceptibility and Kambe fit (only for $[Fe_4^{III}(acac)_6(Br\text{-}mp)_2]$ **(1)**) $\chi_{mol}T$ vs. temperature of powder samples of $[Fe_4^{III}(acac)_6(Br\text{-}mp)_2]$ **(1)** and $[Fe_4^{III}(acac)_6(tmp)_2]$ **(2)** at an applied field of 0.1 T.

DC Susceptibility Measurements on Powder

DC susceptibility measurements were performed in a temperature range from 1.8 K up to room temperature in an external magnetic field of 0.1 T. The product of magnetic susceptibility and temperature ($\chi_{mol}T$) as function of temperature is shown in Fig. 5.3.

For **(1)** $\chi_{mol}T$ steadily decreases from 12.0 $cm^3mol^{-1}K$ at 300 K to a minimum of 10.3 $cm^3mol^{-1}K$ at 110 K, before strongly increasing to 14.3 $cm^3mol^{-1}K$ at 14 K, followed by a drop to 6.4 $cm^3mol^{-1}K$ at 1.8 K. For **(2)** $\chi_{mol}T$ steadily decreases from 11.1 $cm^3mol^{-1}K$ at 300 K to a minimum of 9.7 $cm^3mol^{-1}K$ at 120 K, before strongly increasing to 15.3 $cm^3mol^{-1}K$ at 16 K, followed by a drop to 6.2 $cm^3mol^{-1}K$ at 1.8 K.

Analysis. For both **(1)** and **(2)**, the decrease of $\chi_{mol}T$ is followed by an increase which is indicative of antiferromagnetic exchange with a non-zero spin ground state. For the four Fe(III) atoms this leads to a spin ground state of $S = 5$ for both **(1)** and **(2)**. The susceptibility of **(1)** was fitted using the Kambe

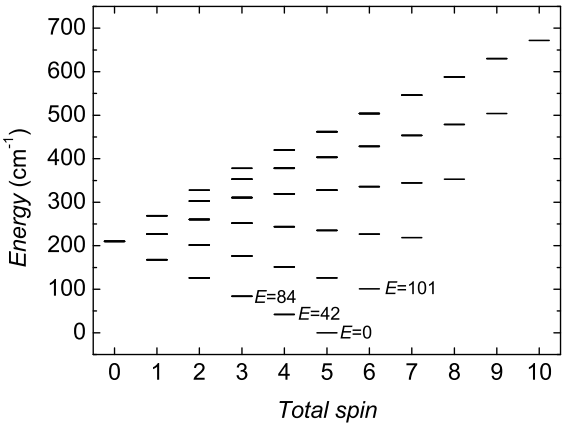

Figure 5.4: Energy level spectrum resulting from the Kambe fit of the experimental magnetic susceptibility, showing the $S = 5$ ground state for $[Fe_4^{III}(acac)_6(Br\text{-}mp)_2]$ **(1)**.

model. This model is applicable when the interacting spins can be divided into two groups where all members of one group have the same exchange interactions with all members of the other group [76]. In this case group one is the central iron spin, and group two the three peripheral spins. The spin Hamiltonian and corresponding energies are:

$$H = -2J(\hat{S}_1 + \hat{S}_2 + \hat{S}_3) \cdot \hat{S}_4 = J(\hat{S}_{123} - \hat{S}_T + \hat{S}_4) \tag{5.6}$$

$$E = J\left[S_{123}(S_{123}+1) - S_T(S_T+1) + S_4(S_4+1)\right] \tag{5.7}$$

For **(1)** the fit gives $J = (-8.2 \pm 0.2)\,\mathrm{cm}^{-1}$, with $g = 1.96 \pm 0.02$. The decrease in $\chi_{\mathrm{mol}}T$ at the lowest measurement temperatures is due to zero-field splitting and is not reproduced, because it is not taken into account in the Kambe model. The resulting energy spectrum is shown in Fig. 5.4. The Kambe procedure did not result in an acceptable fit for **(2)**, presumably due to the presence of more than one exchange interaction. The value for J is of the same order of magnitude as for other Fe_4 clusters, as it can be seen from literature.

Parameters relevant for putting results obtained in this chapter into context are shown in Table 5.1. Antiferromagnetic coupling of a central iron(III) with

Table 5.1: Measured parameters from literature of different Fe_4 compounds. If different species were present in the sample only the D or Δ-values which were the highest are given.

Compound	D (cm^{-1})	Δ (K)	J_1 (K)	Δ_{eff} (K)	τ_0 (ns)
$[Fe_4(OMe)_6(dpm)_6]$ [4]	-0.21	7.4	-10.6	3.5	1100
$[Fe_4(L^1)_2(dpm)_6]$ [4]	-0.445	16.0	-8.3	17.0	21
$[Fe_4(L^2)_2(dpm)_6]$ [4]	-0.432	15.5	-8.4	16.6	10
$[Fe_4(L^3)_2(dpm)_6]$ [4]	-0.42	15.0	-8.2	15.6	19
$[Fe_4(OEt)_3(L^4)(dpm)_6]$ [4]	-0.27	9.6	-10.7	6.0	460
$[Fe^{III}[Fe^{III}(L^1)_2]_3]$ [77]	-0.40	14.25	-7.5	N/A	N/A
$[Fe_4(thme)_2(dpm)_6]$ [70]	-0.445	16.0	-8.3	15.6	34
$[Fe_4(thme)_2(C_3H_7OH)_6Cl_6]$ [78]	-0.33	11.9	-7.2	8.5	37

D: Axial zero-field splitting parameter from high-frequency ESR.

Δ: Energy barrier from $(|D|/k_B)S^2$.

J_1: Nearest-neighbor exchange coupling constant from DC susceptibility measurements. The values are given in the definition of the Hamiltonian in Eq. (5.6)

Δ_{eff}: Effective energy barrier against magnetization reversal from AC susceptibility measurements.

τ_0: Attempt relaxation time from AC susceptibility measurements.

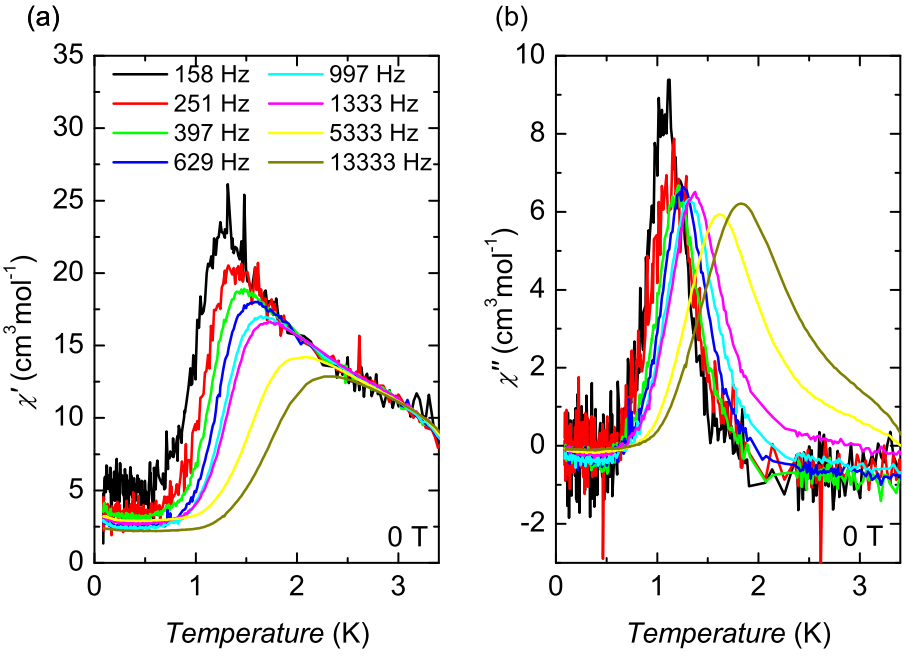

Figure 5.5: Measured AC susceptibility χ' (a) and χ'' (b) versus temperature of a powder sample of $[Fe_4^{III}(acac)_6(Br\text{-}mp)_2]$ **(1)** at 0 T. The measurement was performed in an AC susceptometer in a temperature range of 0.09-3.5 K.

three peripheral Fe(III) ions leads to a high-spin ground state of $S = 5$ for all compounds shown in the table. Both $|D|$ and the effective energy barrier Δ_{eff} are found to increase with higher helical pitch of the core [4]. $|D|$ values in a range of about 0.2 up to 0.45 cm^{-1} were observed. This shows that Fe_4 compounds are suitable systems to tune the anisotropy by exchanging ligands.

AC Susceptibility Measurements on Powder

To shed light on the magnetization dynamics of **(1)** and **(2)** we performed AC susceptibility measurements using the SQUID magnetometer for temperatures

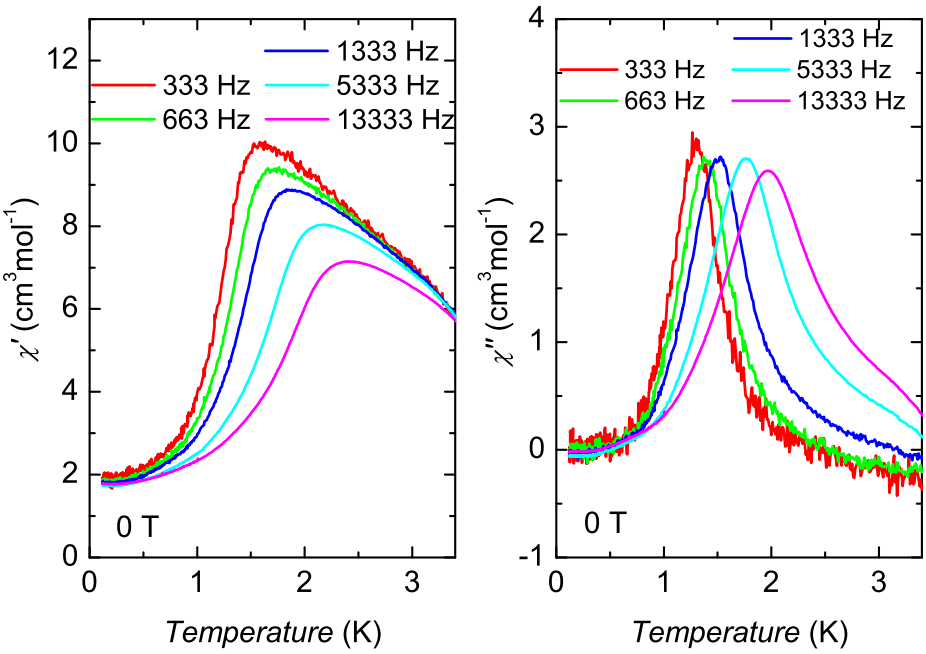

Figure 5.6: Measured AC susceptibility χ' (a) and χ'' (b) versus temperature of a powder sample of $[Fe_4^{III}(acac)_6(tmp)_2]$ **(2)** at 0 T. The measurement was performed in an AC susceptometer in a temperature range of 0.09-3.5 K.

$> 1.8\,\mathrm{K}$. Below these temperatures down to 0.09 K the AC susceptometer (described in Chapter 5.2.2) was used. Additional data for measurements at high AC frequencies were obtained with the PPMS. In powder measurements on samples of **(1)** and **(2)** in the SQUID, χ'' increases for low temperatures and is frequency dependent (data not shown here), but no peak could be observed in the experimental temperature range down to 1.8 K. Therefore the maximum in χ'' was expected at even lower temperatures, which were accessible by using the AC susceptometer incorporated in a dilution cryostat (Chapter 5.2.2).

Fig. 5.5 shows the in-phase component χ' (a) and the out-of-phase component χ'' (b) of the AC susceptibility for **(1)** dependent on temperature for different frequencies in a range from 158 Hz to 13333 Hz. Lower frequencies were not accessible due to limited sensitivity. The data was processed according to the procedure described in Chapter 5.2.1. χ' is small and constant for low temperature, then strongly increases to values in between $12.9\,\mathrm{cm^3mol^{-1}}$ (for 13333 Hz) and $22.8\,\mathrm{cm^3mol^{-1}}$ (for 158 Hz). The increase starts at lowest temperature for lowest frequency and occurs in ascending order in ways of temperature dependent on frequency. The measurement shows a strong out-of phase component χ'', where the position of the maxima is clearly temperature dependent (1.098 K for 158 Hz up to 2.30 K for 13333 Hz).

To study the influence of magnetic tunneling on the dynamic magnetization in **(1)**, the degeneracy of the lowest lying energy levels was lifted in the following experiments by applying an external magnetic field of 0.1 T. The data are not shown here, only the frequency dependence of the maxima of χ'' will be analyzed further.

Fig. 5.6 shows the in-phase component χ' (a) and the out-of-phase component χ'' (b) of the AC susceptibility for **(2)** dependent on temperature for different frequencies in a range from 333 Hz to 13333 Hz. The data was processed according to the procedure described in Chapter 5.2.1. χ' is small and constant for low temperature, then strongly increases to values in between $7.1\,\mathrm{cm^3mol^{-1}}$ (for 13333 Hz) and $10.0\,\mathrm{cm^3mol^{-1}}$ (for 333 Hz). The increase starts at lowest temperature for lowest frequency and occurs in ascending order in ways of temperature dependent on frequency. The measurement shows a strong out-of phase component χ'', where the position of the maxima is clearly temperature dependent (1.137 K for 133 Hz up to 1.976 K for 13333 Hz).

Analysis. The clear observation of out-of-phase components shows the slow relaxation dynamics in both **(1)** and **(2)**. Additionally, the clear temperature

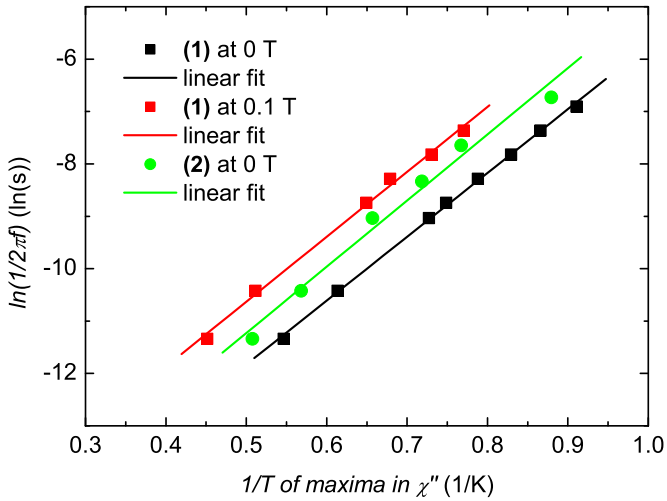

Figure 5.7: Positions of maxima of χ'' in an Arrhenius plot $\ln(\tau)$ versus $1/T$ for $[Fe_4^{III}(acac)_6(Br\text{-}mp)_2]$ **(1)** at 0 T and 0.1 T and for $[Fe_4^{III}(acac)_6(tmp)_2]$ **(2)** at 0 T. Lines show the fits with the Arrhenius law.

Table 5.2: Fit parameters obtained from Arrhenius plots of **(1)** and **(2)**.

sample	B_0	Δ_{eff}/k_B in K	τ_0 in ns
$Fe_4^{III}(acac)_6(Br\text{-}mp)_2$ **(1)**	0 T	12.2±0.2	17±3
$Fe_4^{III}(acac)_6(Br\text{-}mp)_2$ **(1)**	0.1 T	12.4±0.4	47^{+16}_{-9}
$Fe_4^{III}(acac)_6(tmp)_2$ **(2)**	0 T	12.6±0.8	24^{+18}_{-10}

dependency in the maxima of the out-of-phase signal rules out the possibility of long-range magnetic order, which would lead to maxima at the same temperature. To compare the effective energy barrier from AC susceptibility measurements with the barrier expected from spectroscopic measurements, an analysis with the Arrhenius law [79] was performed. For that the maxima in χ'' were determined at low and noisy frequencies (<1000 Hz) by fitting with a Lorentzian lineshape, whereas for high frequencies (>1000 Hz), where the lines are not symmetric any more, simply the maximum values were taken. The asymmetry for high temperatures is due to the loss of superconductivity in the AC coils.

The maxima in χ'' were plotted in Arrhenius plots $\ln(\tau)$ versus $1/T$ in Fig. 5.7 for **(1)** and **(2)**. The range in $1/T$ is limited. To lower temperatures of maximum χ'' this is due to the insufficient sensitivity of the setup at lower frequencies. To higher temperatures of maximum χ'', the AC susceptometer is not suitable, because the AC coil leads lose their superconductivity. The SQUID and PPMS setups do not allow to apply higher AC frequencies, where maxima in χ'' are expected to be located at accessible temperatures.

The data in the Arrhenius plots were fitted with an Arrhenius equation $\tau = \tau_0 e^{-\Delta_{\text{eff}}/(k_B T)}$, where Δ_{eff} is the effective energy barrier. The resulting fit parameters are shown in Table 5.2. The fit was performed without assuming a constant Δ_{eff} or fixed τ_0.

In zero field ground state tunneling may reduce the effective barrier height, as the spin has an additional path than the thermal relaxation barrier to relax. In an applied field the degeneracy of the ground state levels is lifted, therefore tunneling is expected to be suppressed. An influence of an external magnetic field on the prefactor τ_0 is not expected.

The thermal relaxation barrier expected from the zero-field splitting parameters determined in CW W-Band ESR measurements on powder of **(1)** is $\Delta_{\text{eff}}/k_B = DS^2 = (12.33 \pm 0.02)\,\text{K}$, plus there is a distribution in D-values (Section 5.3.3). Therefore the observed energy barriers show that there is no or negligible ground

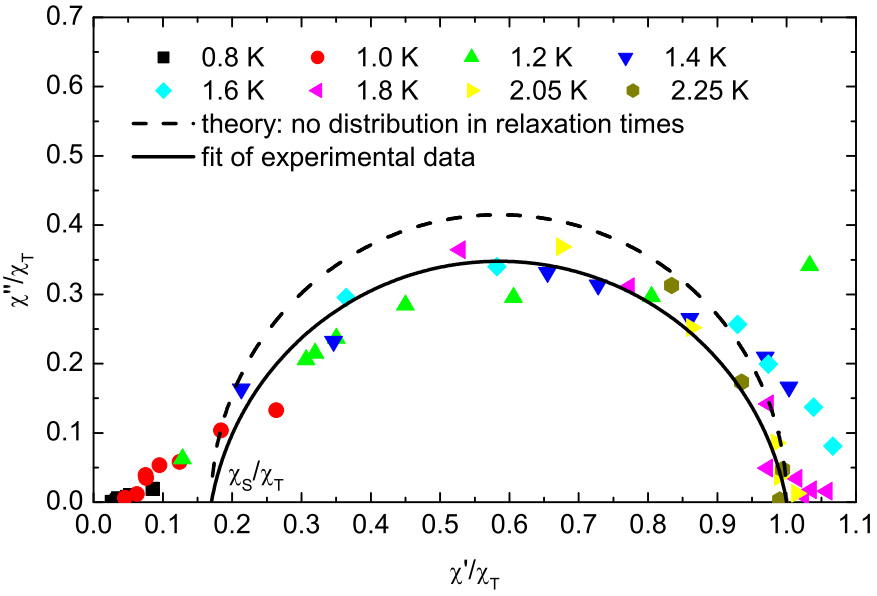

Figure 5.8: Argand plot for powder of $[Fe_4^{III}(acac)_6(Br\text{-}mp)_2]$ **(1)**. Broken line: No distribution in relaxation time. Solid line: Fit for experimental data with a distribution in τ.

state tunneling. This result is supported by the fact that the barrier does not decrease in an applied magnetic field of 0.1 T. A similar energy barrier comparing the value from DS^2 and from AC susceptibility measurements was also observed for other Fe_4 compounds (see table 5.1).
The attempt relaxation time τ_0 found for **(1)** and **(2)** at 0 T is comparable to the ones found for other Fe_4 compounds (see table 5.1), particularly to the one of the complexes $[Fe_4(L^n)_2(dpm)_6]$ [4]. Interestingly, the prefactor τ_0 is different in a comparison of the Arrhenius fit of 0 T and 0.1 T in the case of **(1)**. The increase of τ_0 can be understood by considering the limiting process for τ_0: The transition in between the highest lying energy levels ($m_S = \pm 1 \rightarrow 0$) limits the relaxation for high temperatures, because the energy splitting, $\Delta E = hf$, in between these levels is the smallest. τ_0 increases, because these spin levels approach for an applied field below the field of the first level crossing, and this narrowing leads to a reduced transition probability. The transition probability is proportional to $(hf)^3$ for direct processes ([16], p. 174), which is considered to be the most important relaxation process. The first level crossing is at about 0.36 T.

To investigate the relaxation processes involved, we plotted χ'' versus χ' (Fig. 5.8). This representation is called Cole-Cole plot (for dielectrics [80]) or Argand plot (in magnetism [81]). In an Argand plot the experimental data transforms to a semi-circle for a single relaxation process. For this single process susceptibility data can be described with $\chi(\omega) = \chi_S + \frac{\chi_T - \chi_S}{1+i\omega\tau}$, where χ_S is the adiabatic susceptibility and χ_T is the isothermal one [82]. If there is a distribution of relaxation times the description is extended with a parameter α: $\chi(\omega) = \chi_S + \frac{\chi_T - \chi_S}{1+(i\omega\tau)^{1-\alpha}}$ [80]. The broader the distribution in relaxation times the larger is α, up to a maximum of 1. At the same time the center of the circle in the Argand plot shifts to lower χ''.
The fit of the experimental data with a distribution of relaxation times led to an adiabatic susceptibility $\chi_S/\chi_T = 0.17$ and to $\alpha = 0.11$. This means that there is a distribution in relaxation times. Additionally, for small χ' another semicircle or semicircles can be observed. This implies that different components of the magnetization relax with different processes. The parameter α is < 0.1 for $Mn_{12}Ac$ [16], which means that here the distribution of relaxation times is narrower. For another Fe_4 complex $(PhC(CH_2O)_3)_2(dpm)_6)$, α was found to be 0.21 ([83], supplementary information), which shows a broader distribution of relaxation times. A temperature dependent analysis of the Argand plot was not performed due to the noisy susceptibility data.

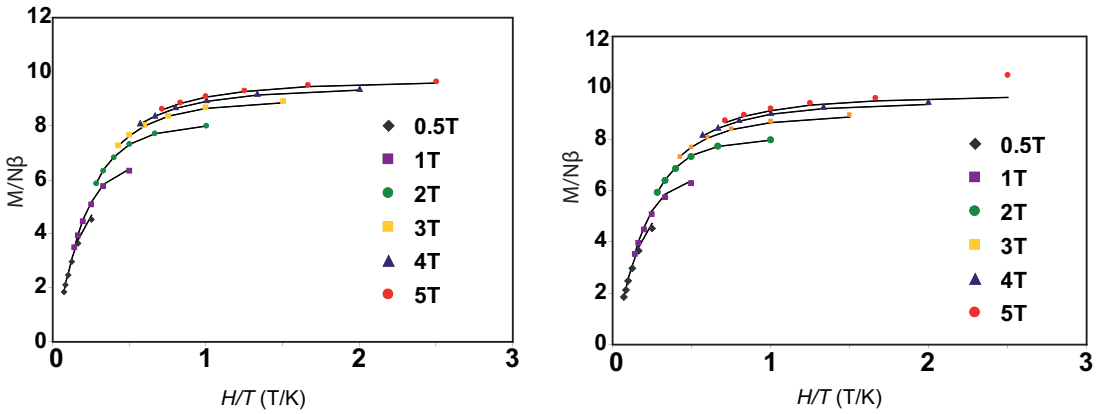

Figure 5.9: Reduced-magnetization measurements from [84]. Given is the magnetization divided by $N\beta$ versus the magnetic field divided by the temperature. Hereby N is Avogadro's number and β is the Bohr magneton. The data was fitted with a spin Hamiltonian with an uniaxial anisotropy.

In the case of **(2)** the barrier is $\Delta/k_B = DS^2 = (12.55 \pm 0.07)\,\mathrm{K}$ from FDMRS measurements (Chapter 5.3.2). This value is the same as the effective energy barrier Δ_{eff} determined by AC susceptibility measurements (Table 5.2), which shows that also for **(2)** there is no or negligible ground state tunneling. In literature in some cases the effective energy barrier observed in AC susceptibility measurements corresponds to the one from $\Delta = (|D|/k_B)S^2$, in some cases it is significantly smaller (see table 5.1).

The findings of this section support the results of the CW W-Band ESR spectra of **(1)** (Chapter 5.3.3), where no E parameter was necessary to obtain a good fit. A nonzero E would mix the levels in zero field and lead to ground state tunneling.

From reduced-magnetization measurements (Fig. 5.9) as a function of the ratio of field over temperature, a first estimate of the axial zero-field splitting tensor D was obtained [84]: $D = -0.337\,\mathrm{cm}^{-1}$ for **(1)**, $D = -0.354\,\mathrm{cm}^{-1}$ for **(2)**, and a spin ground state of $S = 5$ for both compounds.

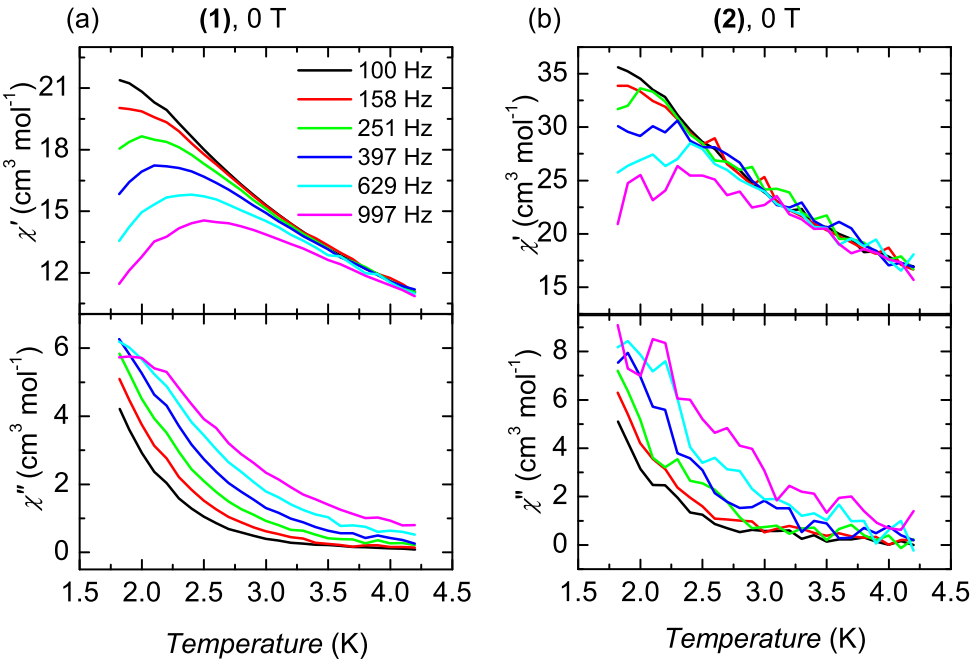

Figure 5.10: Measured AC susceptibility versus temperature for $[Fe_4^{III}(acac)_6(Br\text{-}mp)_2]$ **(1)** (left) and $[Fe_4^{III}(acac)_6(tmp)_2]$ **(2)** (right) in toluene at 0 T. The measurement was performed in a SQUID. The concentrations were 5 mg/ml for **(1)** and 0.5 mg/ml for **(2)**.

AC Susceptibility Measurements on Solutions

We performed AC susceptibility measurements to study the slow relaxation dynamics of **(1)** and **(2)** in solution. This is important, because all quantum coherence studies on **(1)** (Chapter 6) were performed on diluted solutions, and we wanted to make sure that we observe still a SMM. Both long-range ordering and spin glass behavior will not be observed in solution, whereas SMM behavior will most likely be preserved.

AC susceptibility measurements on **(1)** and **(2)** in toluene were performed in a Quantum Design MPMS-XL 7 SQUID magnetometer (Fig. 5.10). It turns out that in solution the maxima in χ'' shift to higher temperatures. This enables us to observe these maxima, even though measurements in the AC susceptometer

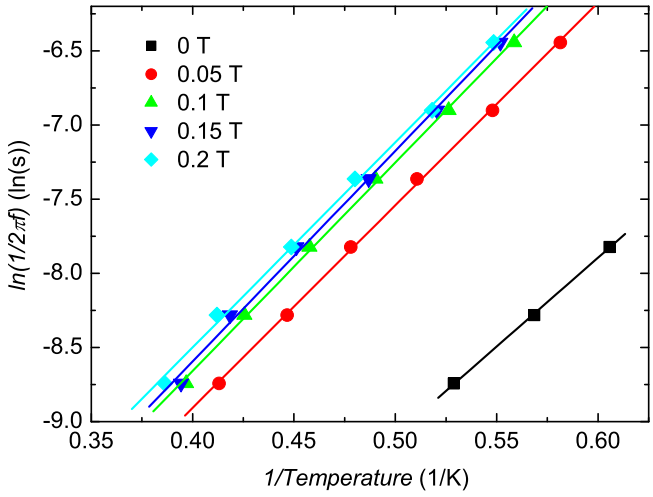

Figure 5.11: Positions of maxima of χ'' in an Arrhenius plot $\ln(\tau)$ versus $1/T$ for $[Fe_4^{III}(acac)_6(Br\text{-}mp)_2]$ **(1)** in toluene at different fields. Lines show the fits with the Arrhenius law.

in the dilution fridge are not possible due to the limited sensitivity of this setup. The noise level of the measurement of **(2)** is significantly higher due to the 10 times smaller concentration.
Additional measurements (not shown here) were performed on **(1)** in toluene at static magnetic fields of 0.05 T, 0.1 T, 0.15 T and 0.2 T to study the influence of tunneling on the relaxation rate. In the analysis we will present the maxima in χ'' from these measurements.

Analysis. The clear observation of out-of-phase components shows the slow relaxation dynamics for both **(1)** and **(2)** in toluene. Therefore this measurement shows that in solution these compounds behave like a single-molecule magnet.

Maxima of χ'' were determined by fitting with a Lorentzian lineshape. The maxima in χ'' were plotted in Arrhenius plots $\ln(\tau)$ versus $1/T$ in Fig. 5.11 for **(1)** in toluene at the measured fields. The measurements were limited to low temperatures by the temperature range of the VTI of the SQUID. To the other end the range was limited by the maximum frequency which can be applied in

B_0	Δ_{eff}/k_B in K	τ_0 in ns
0.00 T	12.0±0.3	280±40
0.05 T	13.7±0.2	570±50
0.10 T	14.1±0.3	630±70
0.15 T	14.2±0.4	630±120
0.20 T	13.8±0.4	800±130

Table 5.3: Fit parameters obtained from Arrhenius plots of $[Fe_4^{III}(acac)_6(Br\text{-}mp)_2]$ **(1)** in toluene at different fields.

the SQUID. The data was fitted linearly, fit parameters are given in table 5.3. The effective energy barrier Δ_{eff} is (12.0 ± 0.3) K in zero field and rises to about 14 K for all other fields, where within the error Δ_{eff} is constant. This increase in barrier height dependent on field is not certain, because for the fit of 0 T only three data points were available. But comparing the average, effective barrier at nonzero field to the barrier obtained from measurements on powder at 0.1 T in the previous section, we can conclude that the effective energy barrier increased by about 10%. This means that the axial zero field splitting parameter D of **(1)** in solution is enhanced, because tunneling is negligible at nonzero field.
τ_0 increases clearly from (280 ± 40) ns at zero field up to (800 ± 130) ns at 0.2 T. The increase of τ_0 is presumably due to approaching spin levels which limit the relaxation at high temperatures, analogous to the process described for the powder measurements. Again the applied magnetic fields are lower than the first crossing field, which is a prerequisite for approaching spin levels and the subsequent slower relaxation over the barrier.
Compared to the values of τ_0 in powder from the previous section a significant increase can be identified. A change in τ_0 can be understood considering the different speed of sound (v_t) of a solid state sample and frozen solution. The residual relaxation rate Γ_0 is strongly dependent on the speed of sound, for the direct process $\Gamma_0 \propto v_t^{-5}$.

5.3.2 Frequency Domain Magnetic Resonance Spectroscopy

Frequency domain magnetic resonance spectroscopy (FDMRS) provides a way to characterize the magnetic anisotropy in SMMs [38], and will be used in the following to study the zero field splitting (ZFS) in the two exchange coupled

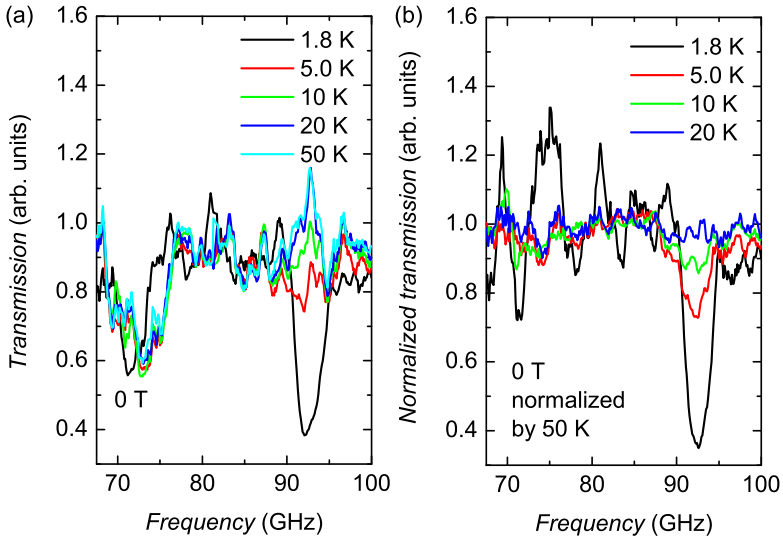

Figure 5.12: (a) Raw transmission data of temperature dependent measurement of $[Fe_4^{III}(acac)_6(Br\text{-}mp)_2]$ **(1)** in transmission at 0 T.
(b) All data were divided by the measurement at 50 K to eliminate standing wave related artifacts.

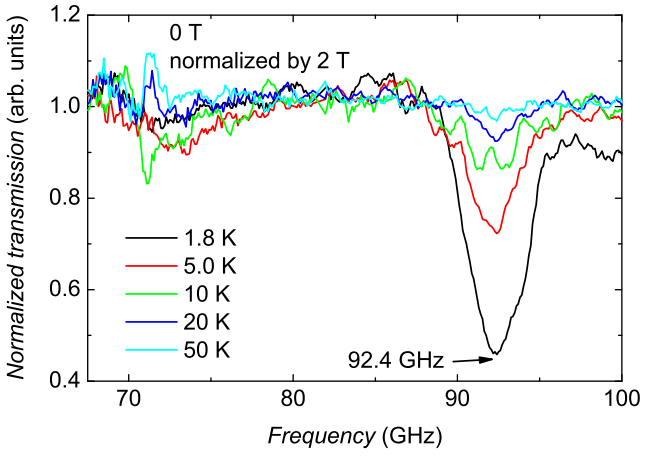

Figure 5.13: All data from Fig. 5.12(a) were divided by the data recorded at 2 T at the same temperature to eliminate artifacts due to liquid helium in the sample space.

clusters. The ground state transition for a $S = 5$ system with $D \approx 0.34\,\mathrm{cm}^{-1}$ (Chapter 5.3.1) is expected at $f \approx 90\,\mathrm{GHz}$. FDMRS, in contrast to W-Band ESR, is also suitable to observe transitions with an energy larger than 94 GHz, so that even if D was larger than expected the full spectrum could be observed.

Fig. 5.12(a) shows the raw transmission data of **(1)** in the temperature range from 1.8 K to 50 K and in a frequency range of 67-100 GHz. The sample was prepared according to the procedure described in Chapter 5.2.3. Below a modulation amplitude for the BWO high voltage of $U_{\mathrm{mod}} = 10\,\mathrm{V}$, the signal did not show any difference in lineshape anymore (see Chapter 2.3.3), so this modulation voltage was used, for all experiments described in this chapter. One can observe reduced transmission for all temperatures around 72.7 GHz. Around 92.0 GHz one can observe a minimum in transmission at 1.8 K, and a difference in signal for other temperatures.

Standing waves introduced by the plane parallel sample compared to the reference measurement can be eliminated by dividing the spectra by the spectrum at highest temperature. At this temperature, in this case 50 K, the small population difference of the levels will lead to a negligible magnetic resonance absorption. The result of this data processing is shown in Fig. 5.12(b). Here the noisy data points at 81.5 GHz were omitted. The division by the highest temperature data clearly reduces the standing wave background for 5.0 K-20 K. At 1.8 K apparently a different standing wave pattern was present, which we assign to liquid helium present in the sample space. The minimum in transmission at lowest temperature is centered at 92.6 GHz, the relative transmission at this frequency is 0.35. The absorption at this frequency clearly decreases with increasing temperature. In an external magnetic field the magnetic sublevels split and therefore the absorption peaks shift. To clearly assign the observed absorption to a magnetic transition, a measurement with a magnetic field of 2 T was performed. This field leads to a shift of magnetic transitions with $\Delta m_S = 1$ of $\Delta f \approx 56\,\mathrm{GHz}$ to higher frequencies (using the Zeeman splitting of a $g = 2$ species with $B_0 \| z$). This means that all transitions observed in the previous measurement at 0 T would be outside of the shown frequency range.

The data of Fig. 5.12(a) at 0 T was divided by data recorded at 2 T at the same temperatures; the resulting spectra are shown in Fig. 5.13. The standing wave pattern at 1.8 K is eliminated much better in this case than in the normalization by 50 K. One can clearly observe the temperature dependent absorption centered around 92.4 GHz. At other temperatures the spectra are similar, except around 72 GHz. Here an absorption is visible for 10 K; for 20 K and 50 K moreover a

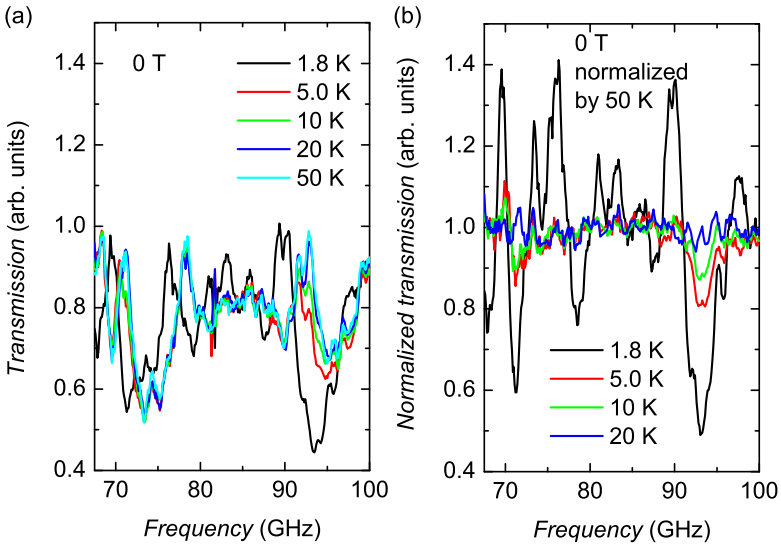

Figure 5.14: (a) Raw transmission data of temperature dependent measurement of $[Fe_4^{III}(acac)_6(tmp)_2]$ **(2)** in transmission at 0 T.
(b) All data were divided by the measurement at 50 K to eliminate standing wave related artefacts.

slightly enhanced transmission in respect to the measurement at 2 T is detectable.

The same spectra were recorded and analyzed the same way for **(2)**. Fig. 5.14(a) shows the raw transmission data of **(2)** in a temperature range from 1.8 K to 50 K and in a frequency range of 67-100 GHz. Without normalization the only strong difference between the measurements is a reduced transmission around 93.3 GHz for the measurement at lowest temperature compared to the other temperatures. Again, the transmission of the measurement on **(2)** at 1.8 K deviates strongly from the measurements at other temperatures. To eliminate background oscillations the spectra were divided by the spectrum at highest temperature, the result can be seen in Fig. 5.14(b). The division by the highest temperature data clearly reduces a standing wave background for 5.0 K-20 K. The minimum in transmission at lowest temperature is centered at 93.0 GHz, the relative transmission at this frequency is 0.49. The absorption at this frequency clearly decreases with increasing temperature. Additionally, there is a slight minimum in transmission visible comparing the values at 5.0 K and 10 K with the other temperatures at 71.4 GHz.

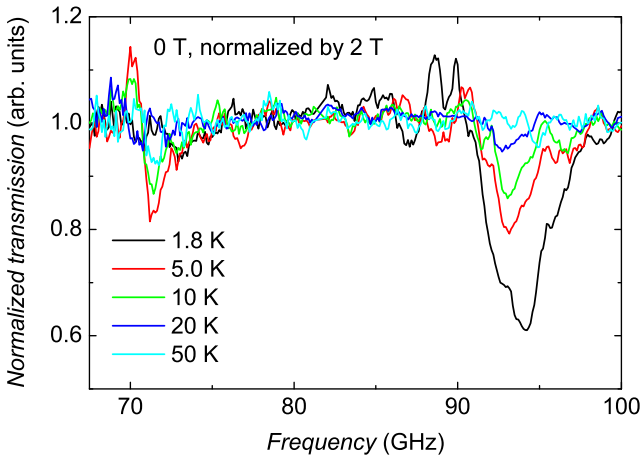

Figure 5.15: All data from Fig. 5.14(a) were divided by the data recorded at 2 T at same temperature to eliminate artefacts due to liquid helium in the sample space.

To be able to eliminate the standing wave pattern as well in the measurement at 1.8 K, the data of Fig. 5.14(a) at 0 T was divided by the data in recorded at an external magnetic field of 2 T at the same temperatures; the resulting spectra are shown in Fig. 5.15. The standing wave pattern at 1.8 K is eliminated much better in this case. One can clearly observe the temperature dependent absorption centered around 94.2 GHz. The relative transmission at lowest temperature is 0.61. A shoulder in the absorption is visible at 93.1 GHz in the measurement at 1.8 K which merges with the main absorption at higher temperatures. The measurement at 50 K does not show any relevant absorption at this frequency. At 71.4 GHz another, less pronounced, absorption line is visible: Here the absorption is strongest for 5.0 K and reduced for 10 K and 50 K; at 1.8 K and 20 K the absorption is negligible.

Analysis. It was possible to observe at least one magnetic transition in the studied frequency range. Having in mind the estimates of $D = -0.337\,\mathrm{cm}^{-1}$ for **(1)** and $D = -0.354\,\mathrm{cm}^{-1}$ for **(2)** (Chapter 5.3.1) we expect to observe in the case of $S = 5$ SMMs the $-5 \rightarrow -4$ transition around 90.9 GHz (for **(1)**) and 95.5 GHz (for **(2)**). The observed absorption lines at lowest temperature at

92.4 GHz and 94.2 GHz fit to the expected values. The intensity of the transition decreases strongly for increasing temperature, this supports the assumption that we observe a ground state transition. Within the error the intensity ratio of the transition at different temperatures follows the Boltzmann distribution. The complex standing wave pattern owed to the frequency range of interest reduces the effective sensitivity of the FDMRS method. At higher frequencies standing wave patterns can be modeled by assuming a plane parallel dielectric, and therefore absorption lines can be distinguished from the oscillatory standing wave pattern. This procedure is not possible in the frequency range of interest.
Assuming an $S = 5$ axial high spin system we expect to observe the first excited transition at $\frac{f_{m_S=-4\rightarrow-3}}{f_{m_S=-5\rightarrow-4}} = \frac{D(2m_S-1)}{D(2m_S-1)} = \frac{7}{9}$ of the ground state transition frequency. Therefore, the absorption observed around 71 GHz in both **(1)** and **(2)** we can tentatively assign to this excited state transition.

Using the frequencies of the strongest absorption from the measurement normalized by data at 2 T, and assigning it to the ground state transition of an axial $S = 5$ high spin system, we obtain the following values of the axial zero field splitting D:
For **(1)**: $f = (92.4 \pm 0.3)\,\mathrm{GHz}$, $D = \frac{f_{m_S=-5\rightarrow-4}}{(2m_S-1)} = (-0.342 \pm 0.005)\,\mathrm{GHz}$.
For **(2)**: $f = (94.2 \pm 0.3)\,\mathrm{GHz}$, $D = \frac{f_{m_S=-5\rightarrow-4}}{(2m_S-1)} = (-0.349 \pm 0.005)\,\mathrm{GHz}$.
We did not perform a fit for the complete spectrum, because the assignment of the $-4 \rightarrow -3$ transition is not clear, and because even in the normalized spectra the background is still strong.

The magnetic transitions below the operating frequency of the W-Band spectrometer of 94.3 GHz show that it is expected that all transitions can be observed in W-Band. The ground state transition will therefore occur close to zero external magnetic field in W-Band. This is in contrast to other Fe_4 compounds which were thoroughly investigated [4], where zero-field splittings are either significantly larger or smaller than in this case. Being able to study ground state transitions in W-Band, because then also pulsed W-Band measurements are possible (see Chapter 6) and coherenct properties can be determined.

5.3.3 CW W-Band ESR

Measurement on a Powder Sample

In order to characterize the zero-field splitting of **(1)** in more detail, we performed continuous wave (CW) ESR measurements on a powder sample at 4.3 K. The

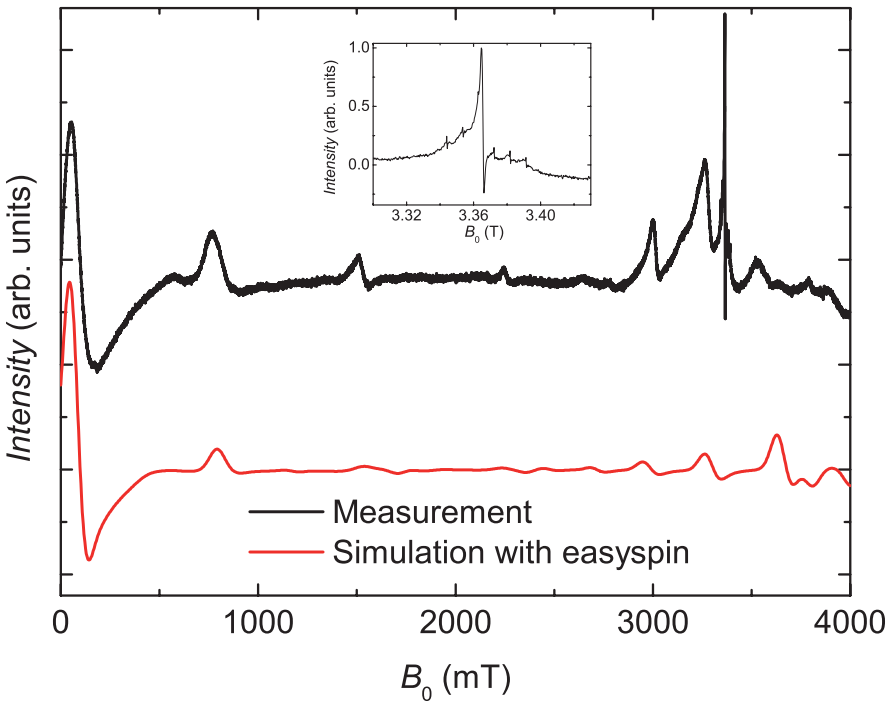

Figure 5.16: Experimental W-Band ESR spectrum and easyspin simulation of $[Fe_4^{III}(acac)_6(Br\text{-}mp)_2]$ **(1)** with the following parameters: $S = 5$, $T = 4.3\,K$, $g = 2.00$, $f = 94.22\,GHz$, first derivative spectrum, $D = -0.3429\,cm^{-1}$, $E = 0$, Lorentzian broadening: $90\,mT$, $D_{strain} = 70\,mT$.

measurement data are shown in Fig. 5.16. The inset shows the field range from 3.30 GHz to 3.43 GHz, because in this field range structures are not resolved in the overview plot.

Analysis. Equally spaced absorptions are expected for parallel transitions in a high spin system. Considering the found D-value from FDMRS we expect to see the ground state transition close to zero external magnetic field. Therefore we assign the clearly visible equally spaced transitions as follows: 0.06 T: $m_S = -5 \rightarrow -4$, 0.77 T: $m_S = -4 \rightarrow -3$, 1.51 T: $m_S = -3 \rightarrow -2$, 2.25 T: $m_S = -2 \rightarrow -1$. Only the maxima in ESR intensity were given; the powder spectrum leads to a spectrum which does not show clear inflection points.
For fields > 2.5 T we see the superposition of the transitions of the molecules with $B_0 \perp z$ and the impurities of the cavity around 3.36 T (see inset of Fig. 5.16). These impurities were also observed in measurements on solutions, and in measurement without any sample. The strong signal of the impurities in the cavity compared to the one of the spin systems is due to the large widths of the lines of the sample and the distribution of orientations, which reduces the absolute peak heights of the ESR signal of **(1)**. Simulations with the Hamiltonian given in Chapter 1.2 were performed using the Matlab package easyspin [59]. Hereby the experimental parameters ($T = 4.3$ K and $f = 94.22$ GHz, first derivative spectrum) were kept constant. In addition the total spin $S = 5$ was kept fixed, attributed to the known coupling scheme for other Fe_4 compounds [4]. D, E, the Lorentzian broadening and the distribution in D tensor values (D_{strain}) were varied. Best fit results were obtained for an axial spin system with $D = (-0.3429 \pm 0.0005)\,\text{cm}^{-1}$, all other fit parameters are given in the caption of Fig. 5.16. Introducing off-diagonal elements in the Hamiltonian ($E \neq 0$) did not improve the fit. The error is given by the confidence interval of the simulation plus the error in the field reading (3 mT).

The value for D is the same as in the FDMRS results ($D = (0.343 \pm 0.005)\,\text{cm}^{-1}$), but could be determined with a much higher precision. The other peaks in the spectrum are also well reproduced. Comparing the peaks of the four lowest lying parallel transitions the error is < 0.05 T in between measurement and simulation. To illustrate the parallel and perpendicular transitions, the spin levels were plotted using easyspin, using the found ZFS parameters (see Fig. 5.17). Moreover, the value of D is within the expected range from literature (compare with values shown in table 5.1).

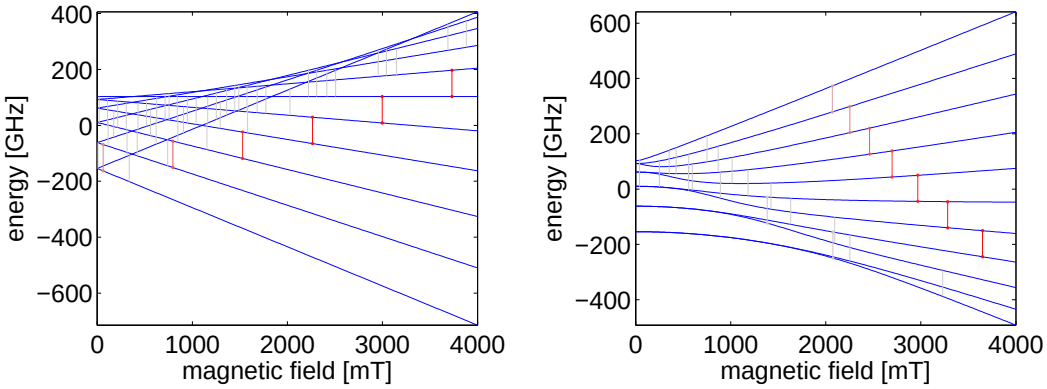

Figure 5.17: Spin levels for parallel ($B_0 \| z$, left figure) and perpendicular ($B_0 \perp z$, right figure) orientation of $[Fe_4^{III}(acac)_6(Br\text{-}mp)_2]$ **(1)** calculated with easyspin using the found ZFS parameters. The allowed microwave transitions are given by red lines, gray lines indicate forbidden ones.

Measurements on Frozen Solutions

To study magnetic properties of **(1)** in solution, CW W-Band ESR spectra in different solvents were recorded at $4.3-4.5\,K$ (Fig. 5.18). For comparision also the spectrum of a mixture of dichloromethane with toluene (without Fe_4 compounds) in the ratio 1:1 is included in the plot. The same microwave power and comparable temperatures were used in all measurements. Only at low fields $< 0.8\,T$ significant ESR intensity can be observed.

Analysis. The ESR measurement of **(1)** in toluene shows a broad signal centered at $(0.34 \pm 0.02)\,T$. Additional shoulders are visible for higher fields. The measurement in toluene-d_8 shows the same lineshape with smaller intensity. Additionally, at $0.45\,T$ a signal is observable in the measurements of **(1)** in toluene and toluene-d_8, which we assign to molecular oxygen [85] (see analysis of the solvent-only measurement below). The spectrum of Fe_4 in toluene was simulated with the following parameters: $D = -0.349\,cm^{-1}$, linewidth $0.537\,T$, $D_{strain} = 0$, first derivative spectrum. This shows that D is virtually unchanged in solution, compared to the powder spectrum (where $D = -0.3429\,cm^{-1}$, but the linewidth is significantly larger than in powder. The increased linewidth we assign to nonequivalent cluster environments in the solution, which lead to a broad distribution of D-values. The different intensities of the ESR signal of **(1)** and molecular oxygen can have two

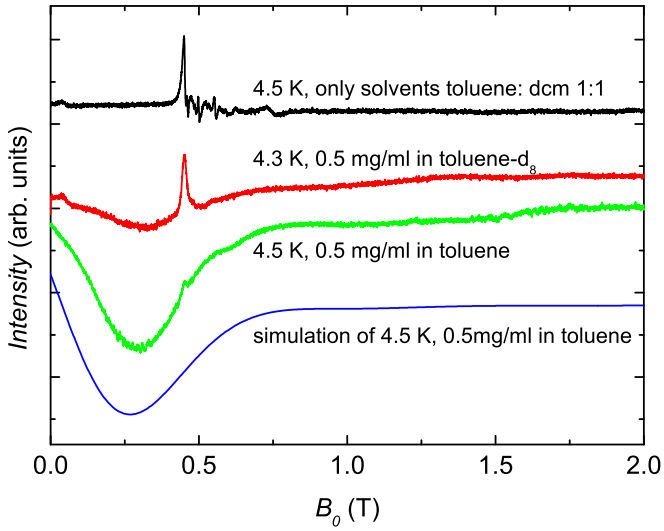

Figure 5.18: CW W-Band ESR measurement on $[Fe_4^{III}(acac)_6(Br\text{-}mp)_2]$ **(1)** in different solvents at low temperatures. The black trace shows the solvent-only signal. The blue trace shows a simulation of the measurement with easyspin.

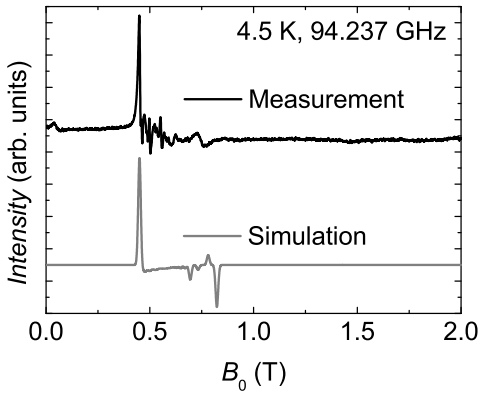

Figure 5.19: CW W-Band measurement on a mixture of dichloromethane and toluene and easyspin simulation of a $S = 1$ molecular oxygen spectrum.

reasons: First, the depth of insertion into the cavity influences the ESR signal strength. Second, dependent on the time needed for sample preparation a different fraction of the compound has decomposed, and at the same time a different amount of oxygen can be dissolved.

In the solvent-only measurement two significant signals can be observed: First at 0.45 T, which we assign to dissolved molecular oxygen [85]. A simulation with easyspin [59] assuming a $S = 1$ spin system leads to a satisfactory fit (see Fig. 5.19) for the following parameters: $D = 3.564\,\mathrm{cm}^{-1}$ (from [85]): $D = 3.572\,\mathrm{cm}^{-1}$ and a Lorentzian linewidth of 15 mT. The signal around $g = 2$ (not shown) is assigned to paramagnetic impurities in the microwave cavity.

5.4 Conclusions

The properties of the two new Fe_4 compounds presented in this chapter underline the possibility of tuning the magnetic anisotropy by choosing the ligands.
In solution we observed magnetic properties which varied from the ones of powder samples, nevertheless the single-molecule magnet behavior was preserved. This is a crucial result for the study of quantum coherence in **(1)** (Chapter 6), where diluted solutions are necessary to delimit magnetic dipolar interactions to increase coherence times.
The change of the local environment in solution, and the subsequent change in

anisotropy show that in possible application of SMMs in storage or quantum information processing devices one has to bear in mind that SMMs properties are not unperturbed by the surroundings. Nevertheless this study emphasizes that the general SMM properties are preserved without having an ensemble of SMMs, this encourages the study of SMMs on surfaces or even in experiments on single molecules.

Chapter 6

Quantum Coherence in the Single-Molecule Magnet $[Fe_4^{III}(acac)_6(Br\text{-}mp)_2]$

Abstract. In this chapter, we present the first direct observation of quantum coherence in a single molecule magnet.
One of the compounds introduced and magnetically characterized in Chapter 5, $[Fe_4^{III}(acac)_6(Br\text{-}mp)_2]$, was studied using pulsed ESR. We observed quantum coherence with coherence times up to $T_2^* = 1270 \pm 40$ ns in a diluted frozen solution. Measurements in different solvents revealed that nuclear spins in the solvent represent an important decoherence pathway. It was possible to increase decoherence times by eliminating the nuclear spins in the solvent. Furthermore we observed coupling of the electron spin to intramolecular protons.

The additional observation of Rabi oscillations proves that it is possible to coherently manipulate spin states. In spin systems of this size, in this case consisting of 20 coupled electron spins, longliving quantum coherence is not expected.

6.1 Introduction

The classical behavior of our everydays world is an emergent property of quantum systems. The interaction with the environment is responsible for the process of decoherence, which induces the transition from a quantum to a classical system. Recently this transition has drawn a lot of attention (see Chapter 1.6). Furthermore, investigating decoherence processes is a keystone in the proposed application of molecular magnets in quantum information devices. Studying the influence of the environment on coherence in addition to the quantification of coherence times is crucial, because this influence determines the difference in perspective in which a mesoscopic system is described. Molecular magnets are very promising both to be utilized as qubits and as a model system to study the quantum-to-classical transition. Furthermore, high-spin systems have several

magnetic sublevels. With this larger number of spin projections complex spin superpositions are possible, and more quantum information can be processed at the same time [5]. For single-molecule magnets, integer high-spin systems with an anisotropy barrier, the zero-split states allow to reach an important criterion for scalability of qubits at zero external magnetic field (see Chapter 1.6).

Pulsed electron spin resonance is a well established technique to study relaxation and coherence in a broad range of systems. In some cases ESR can reveal and quantify electron-nuclear couplings, which were found to be important decoherence pathways for several quantum systems under investigation (references). In pulsed ESR experiments quantum states are normally manipulated to obtain intrinsic information about the molecules. Interestingly, the pulsed microwave radiation used in these experiments provides the straightforward way for spin manipulation in applications, particularly quantum information processing. In Chapter 4 we showed evidence for sizable quantum coherence in the antiferromagnetic ring Cr_7Ni by pulsed ESR and mentioned other $S = 1/2$ systems studied in literature. In the following, we will describe the two single-molecule magnets where quantum coherence was probed experimentally by pulsed ESR. In 2008, de Loubens [62] studied the single molecule magnet Ni_4 in a diluted solution with 130 GHz ESR at 5.5 K. No echo, that means no quantum coherence was observed. The experiments set an upper bound to the coherence time of $T_2 < 50$ ns.

Dipolar interactions limiting decoherence in non-diluted samples are reduced at lower temperatures. A study taking advantage of this fact was performed by Takahashi *et al.* [20] published in 2009, where pulsed ESR experiments at 240 GHz were performed on single crystal samples $S = 10$ Fe_8 single-molecule magnets. In this case not only very low temperatures down to 1.3 K were applied, the spins were also polarized by an applied external magnetic field of $B = 4.6$ T. In consequence, decoherence times were in an experimentally accessible timescale, e.g. $T_2 = 712 \pm 15$ ns at 1.27 K. Takahashi *et al.* described the temperature dependence of coherence times quantitatively, they assume a residual coherence rate at zero temperature which corresponds to the coherence time expected in diluted samples.

Here we show the first direct experimental evidence for long-lasting quantum coherence and quantum oscillations in a single molecule magnet, by using pulsed ESR spectroscopy [86]. At the date of publication no other group had observed quantum coherence in single-molecule magnets directly. For the studied molecule, $[Fe_4^{III}(acac)_6(Br\text{-}mp)_2]$ **(1)**, the abbreviation Fe_4 will be used, because only this derivate is dealt with in this chapter.

In the previous chapter, we presented magnetization data which proves that Fe_4 is a single-molecule magnet both in the solid state and in solution. The frequency of the W-Band ESR spectrometer of 94.3 GHz is only slightly larger than the energy distance of the two lowest zero-field split magnetic sublevels, as shown in Chapter 5.3.3 by CW W-Band ESR. It allows us to excite the ground state transition $m_S = -5 \rightarrow -4$ at low magnetic fields. Therefore pulsed W-Band ESR constitutes the ideal method to study relaxation and coherence of this single-molecule magnet. The zero-field splitting of single molecule magnets exhibits an advantage for eventual practical applications: Even without an applied external magnetic field the energy splitting between magnetic sublevels may be larger than the thermal energy at liquid helium temperature. This is a prerequisite to avoid the exponential decrease in the readout step of the quantum operation with increasing qubit number.

The chapter is organized as follows: First we describe experimental methods and sample preparation. Second we show a range of coherence and relaxation studies which reveal dependencies on temperature, field and solvent. Then we present data of echo-detected ESR measurements. Finally we show the measurement of Rabi oscillations.

6.2 Experimental Methods

To limit decoherence due to magnetic dipolar interactions the molecules were diluted into a frozen solvent matrix. The solvents were chosen according to the following two criteria: First of all, the molecule has to be chemically stable in the solvent at room temperature for at least 30 minutes. This is the time which is needed from dissolving the complex until the sample is thermally quenched in the precooled cryostat to temperatures below 10 K. At these temperatures all used solvents are frozen. Secondly it is important that the solvent has low dielectric losses to avoid microwave absorption in the cavity.

Furthermore the nuclear spins in the solvents may have interactions with the electron spin. The natural abundances of isotopes with $I \neq 0$ are 1.07% for ^{13}C and 0.75% for ^{33}S, which makes CS_2 a practically nuclear spin free solvent.

6.2.1 Sample Preparation

The solvents used in the presented experiments were dichloromethane (DCM, CH_2Cl_2), toluene (C_7H_8), toluene-d_8 (C_7D_8), carbon disulfide (CS_2) and a mixture of dichloromethane and toluene in the ratio 1:1.

In addition to the ^{1}H-NMR measurements in Chapter 6.2.2 the CW ESR measurements (chapter 5.3.3) showed that for dichloromethane and the glassy solution of dichloromethane and toluene all Fe_4 was decomposed. Furthermore we checked for both solvents that no spin echo could be seen at different fields.

The mass of crushed powder of Fe_4 brought into small glass containers was weighed. The amount of solvent needed for the desired concentration was given into the container using adjustable pipettes from Eppendorf. Then the glass container was agitated until no powder was visible any more, which was the case after less than one minute. This shows that all concentrations chosen were clearly below the saturation concentration of Fe_4 at room temperature. Using a quartz capillary the solution was transferred immediately into W-Band sample tubes with beaded bottom. These tubes have an outer diameter of 0.9 mm and an inner one of 0.5 mm. The sample tubes were flame-sealed to avoid solvent evaporation, during the cooldown procedure. After sealing the tubes they were inserted in the precooled cryostat and cooled down to the desired temperature.

The average distance of the Fe_4 molecules in the solution can be calculated from the chosen concentration. Here it has to be kept in mind that the molecules will not arrange in a cubic lattice. For a random distribution, the arithmetic average of the distance of n molecules in a unit of volume is about $\frac{5}{9}\frac{1}{\sqrt[3]{n}}$ [87], hereby the molecules are considered to be point-like. For the used concentrations of Fe_4 in solution the values of the average distance is given in brackets. The molecular weight 1080.35 g/mol of Fe_4 was used for the calculation. This gives the following results: 1.0 mg/ml (6.8 nm), 0.5 mg/ml (8.5 nm) and 0.2 mg/ml (11.5 nm).

6.2.2 Stability of Fe_4 in Solution

The stability of Fe_4 in solution at room temperature was investigated with ^{1}H-NMR measurements. After certain periods of time after sample preparation the spectrum was recorded (Fig. 6.1). The spectrum changes in time and therefore decomposition of the molecules in solution takes place. The inset of Fig. 6.1 shows the range of 12-24 ppm chemical shift, whereas the measurement at $t = 0$ min was subtracted from other waiting times. The resonance intensity of the lines at 11

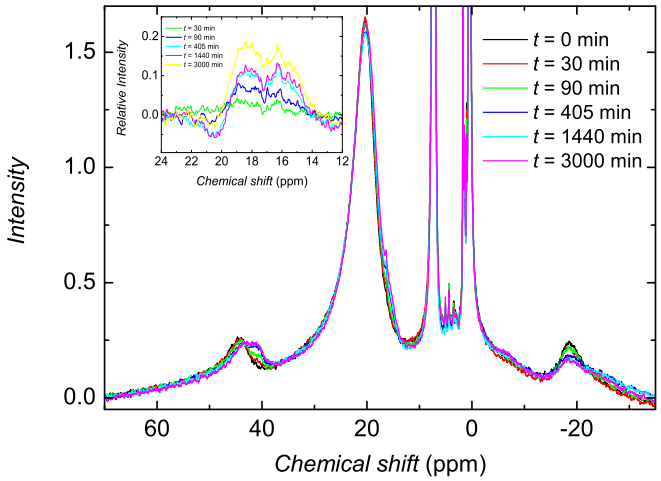

Figure 6.1: ^{1}H-NMR spectra of Fe_4 in benzene-d_6 at room temperature and given delay times. Inset: Immediate ($t = 0$ min) measurement intensity subtracted from the intensity of other time delays in the range of 12-24 ppm chemical shift.

and 18 ppm increase for longer delay times. At $t = 30$ min no significant difference compared to the initial measurement can be seen. The same behavior can also be observed for the resonances at 41 ppm and -19 ppm. We conclude that no significant decomposition of the molecules has taken place 30 min after solution preparation, because the stronger resonance around 17 ppm has to be interpreted as a decomposition product present in the solution. That means that at all pulsed W-Band measurements the dissolved and intact Fe_4 molecules were present.
Pulsed measurements on samples kept at room temperature for 24 hours showed no echo signal, proving the observed echoes are not due to small amounts of decomposition products.

6.2.3 Pulsed ESR

All ESR measurements presented here were performed in the Bruker W-Band ESR spectrometer described in Chapter 2.4. The resonance frequency of the cavity varies only slightly dependent on tuning and temperature. The frequencies used

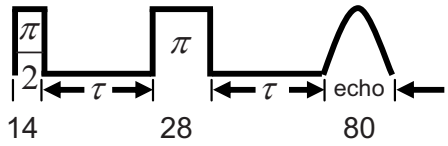

Figure 6.2: Illustration for the used pulse sequence notation. Typical lengths of $\pi/2$-, π-pulses and integration windows in ns are given.

in the experiments were in a range of 94.2-94.5 GHz. For most results presented here the exact frequency is irrelevant. If necessary for analysis, the frequency is given.

First a simple Hahn echo sequence was used to determine if Fe_4 powder samples have detectably long relaxation times. This test was performed at 4.3 K, because at the lowest temperature the relaxation times are expected to be longest. No spin echo could be observed with the chosen experimental parameters, which means that the coherence decayed too fast to be measured. All further experiments were performed in a frozen solvent matrix, because in diluted samples the smaller diploar interactions lead to sizable coherence times.

In all cases, the echo was recorded using an integration window to obtain maximum signal. Time delays given denote the time span between the end of the first pulse and the beginning of the next one (see Fig. 6.2).

The π pulse length was determined with a Hahn echo sequence ($\pi/2 - \tau - \pi - \tau -$ echo). To do so, the lengths of both pulses were varied, and the value of the pulse length for the first maximum in echo intensity was used for the subsequent experiments. In the majority of experiments, the maximum microwave power was used. The only exception is the power dependence in Chapter 6.3.3. Typical π pulse lengths were $t_p = 28 - 32$ ns. In the echo-detected ESR experiment the $\pi/2$-pulse length was 16 ns for Fe_4 in toluene-d_8 and CS_2 and 14 ns in toluene.

It has to be considered that for different spin packets which can be excited at different fields one can expect different π-pulse lengths. Therefore the pulse lengths may not correspond to exact π or $\pi/2$-pulses and in consequence lead to a reduced echo intensity.

6.3 Results and Discussion

The typical π pulse length of $t_p = 28 - 32$ ns corresponds to an excitation width of $\Gamma = \frac{2\pi}{t_p} \approx 0.2$ GHz. The powder ESR spectra (Chapter 5.3.3) exhibit a linewidth

due to different orientations, inhomogeneous broadening and D-strain of about 0.2 T, which corresponds to about 2.8 GHz. Due to additional distortions of the molecules in the frozen solution an additional D-strain is expected. Therefore all experiments here excite only a portion of molecules present in the sample. Which molecules are excited depends on the local environment (and therefore on the actual D-value) and the orientation of the molecule with respect to the external magnetic field [13].

6.3.1 Coherence and Relaxation Studies

In the context of quantum computing the longitudinal relaxation time, T_1, is crucial for the initialization of a qubit: The faster the decay of the magnetization, the faster is the possibility to initialize the system in a well defined state, e.g. by applying an external magnetic field in the case of a spin qubit. In consequence a new quantum operation can be started sooner and the computation speed increases.

T_2, the phase coherence time, is a measure for the time available to perform quantum computational operations before decoherence sets in. Hence it is desirable to have long coherence times.

To quantify both T_1 and T_2 is a crucial step in the process of identifying suitable systems for quantum computation. Additionally we want to identify the processes which lead to decoherence to be able to extend decoherence times by modifying the system.

Temperature dependence of T_1 at 0 T

T_1 of a 0.5 mg/ml solution of Fe_4 in toluene was determined by using a standard inversion recovery sequence ($\pi - \tau - \pi/2 - \tau_{\text{fixed}} - \pi - \tau_{\text{fixed}} -$ echo, see Chapter 2.2.3) with an initial delay τ in between the inversion π-pulse and detection pulses of $\tau = 72$ ns and in a temperature range from 4.3 K to 11.0 K. The echo intensity versus delay time τ is plotted in Fig. 6.3. The fixed time delay of the detecting Hahn echo was 186 ns, which makes the distance in between the last pulse and the echo sufficiently long to suppress all effects of both the reflected pulses and the ringing of the cavity. The value of T_1 at 14.0 K and higher temperatures could not be determined due to insufficient intensity. Echo intensities were rescaled so that intensities at zero delay time would match and approach the same level for infinite delay time. The influence of the temperature dependence of T_2 and therefore an altered echo intensity of the Hahn echo was not considered in this rescaling. All

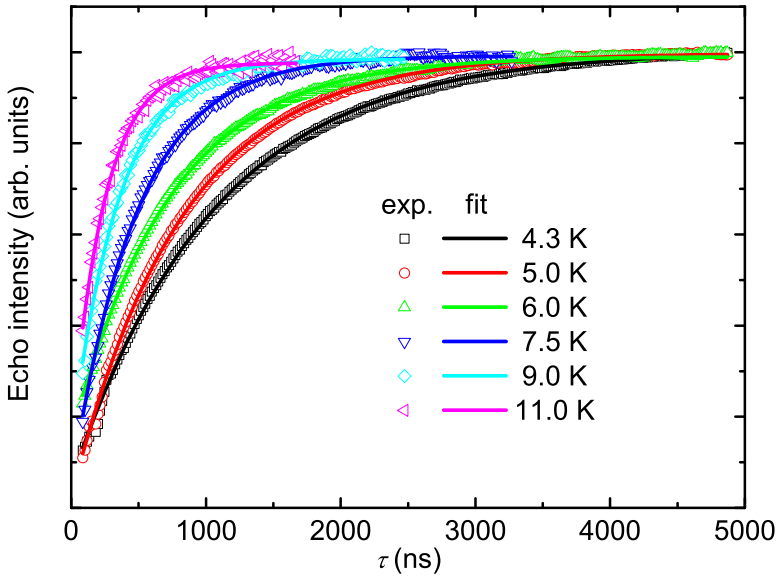

Figure 6.3: Integrated echo intensity after the inversion recovery sequence for Fe_4 in toluene. The data was rescaled so that intensities at zero delay time would match. The experimental data (symbols) was fitted monoexponentially (lines).

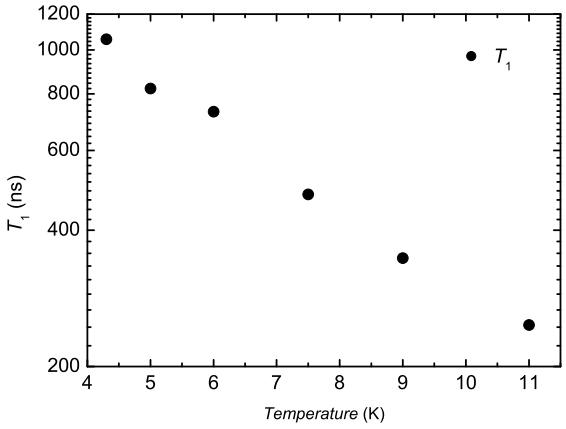

Figure 6.4: T_1 from monoexponential fit of inversion recovery data.

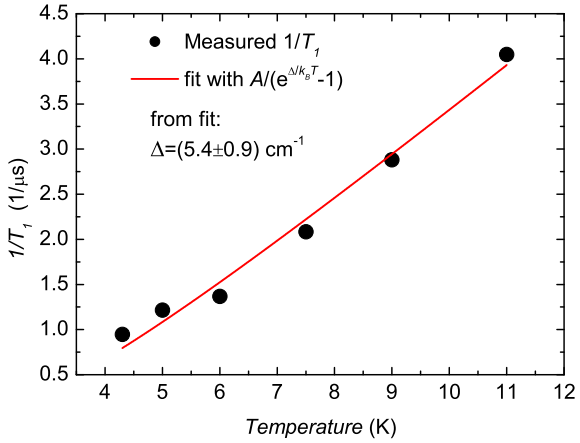

Figure 6.5: Orbach fit of measured values of T_1 for Fe_4 in toluene. Please note that the common Orbach plot ($\ln(1/T_1)$ versus $1/T$ fitted with a straight line) is not suitable as it uses an approximation (see text).

experimental datasets were fitted with an exponential decay function $1 - e^{-\tau/T_1}$.

The decay is clearly temperature dependent, for higher temperature the inversion is recovered in much shorter time. The quantitative dependence of T_1 from the fits is shown in Fig. 6.4. A logarithmic plot has been chosen because of the strong dependence on temperature.

Analysis. The found values for T_1 are comparable to the ones of Fe_8 [20], Cr_7Ni ([3] and Chapter 4.3.2) and V_{15} [49], but three orders of magnitude shorter than for Fe_3 [17] and a minor, slow-relaxation process in V_{15} [49]. The relaxation is monoexponential, indicating that spectral diffusion does play a minor role in the experiment.

The strong temperature dependence of T_1 demonstrates, that spin-lattice relaxation must occur through a two-phonon process, because the direct, one-phonon process is expected to be little temperature dependent [13]. The experimental data was fitted with both the temperature dependence for the Raman process ($1/T_1 \propto AT^n$) and the temperature dependence for the Orbach process ($1/T_1 \propto \frac{\Delta^3}{e^{\Delta/k_BT}-1}$) [13]. Both fits were satisfactory, and due to the limited temperature range we could not distinguish between Raman and Orbach processes. We feel it is an Orbach process, as in exchange-coupled clusters the spin-lattice

relaxation mechanism is often governed by this process. Here an excited spin state functions as the intermediate state. In Fig. 6.5 the Orbach fit is shown for the measured values of T_1 for Fe_4 in toluene. In the case shown here a common approximation for Orbach fits cannot be made: Often $\ln(1/T_1)$ versus $1/T$ is fitted with a straight line, which is an approximation for $kT \gg \Delta$, which is found not to be true here. Therefore in this case the fit was performed with $1/T_1 \propto \frac{\Delta^3}{e^{\Delta/k_BT}-1}$. This yields an energy gap of $\Delta = (5.4 \pm 0.9)\,\mathrm{cm}^{-1}$. This energy is clearly within the ground multiplet, as the first excited state was found to be at $42\,\mathrm{cm}^{-1}$ in Chapter 5.3.1. Therefore the m_S levels of the ground state, which are higher in energy, play a crucial role in the relaxation process. This could explain the strong difference of the absolute value of spin-lattice relaxation times of Fe_4 by three orders of magnitude compared to Fe_3 [17] and the slow relaxation process in V_{15}. In this antiferromagnetic iron(III) trimer ($S = 1/2$) there are no other m_S levels close to the ground state transitions, only higher excited states with a larger energy gap. In this study [17] the Orbach process was also found to be the dominant process for the observed temperature dependence of T_1, which supports our finding for the relaxation process.

Temperature dependence of T_2^* at 0 T in different solvents

In the previous section we investigated the temperature dependence of T_1. Now we want to focus on the phase coherence time T_2^*, which sets the time available for quantum computation operations before decoherence sets in.

The standard Hahn echo sequence ($\pi/2 - \tau - \pi - \tau -$ echo) with an initial delay of $\tau = 86\,\mathrm{ns}$ in between the pulses was employed in a temperature range from 4.3 K to 14.0 K on a 0.5 mg/ml solution of Fe_4 in toluene. The echo intensity versus delay time τ is plotted in Fig. 6.6. The echo intensities were rescaled so that intensities at zero delay time would match. The experimental data was fitted with an exponential decay function $Ae^{-2\tau/T_2^*} + B$ to determine T_2^*.
The decay constant T_2^* increases strongly with increasing temperature (Fig. 6.7).

To investigate the coupling to the nuclear spin bath of the matrix, we investigated Fe_4 samples in three different solvents.

The Hahn echo decay of Fe_4 in the solvents in which Fe_4 was found to be stable is shown in Fig. 6.8. In the case of toluene-d_8 two different concentrations (0.5 mg/ml and 0.2 mg/ml are shown to demonstrate the influence of dipolar interactions between the molecules. In other solvents coherence times were only measured at 0.5 mg/ml. The experimental data was fitted monoexponentially

with $Ae^{-2\tau/T_2^*}+B$. The coherence times T_2^* were 614±40 ns in toluene, 1116±40 ns for Fe_4 in carbondisulfide, 559±40 ns in toluene-d_8 at 0.5 mg/ml and 651±40 ns in toluene-d_8 at 0.2 mg/ml.

Analysis. The exponential fits do not exactly reproduce the echo decay data. Taking a closer look at the difference between echo decay and fit (not shown) we could identify a similar difference for the measurements at 4.3 K and 5.0 K. The addition of a second exponential is not sufficient to model this deviation, nor a superimposed oscillation with only one frequency. The second exponential would have meant the presence of two decoherence processes or two different derivatives of Fe_4 which are present. On the basis of our measured data there is no clear observation of a biexponential decay. The oscillations could have indicated a nuclear modulation effect in zero field ([88]) or at small finite field, for example the remanent field of the room temperature coils.

We additionally performed fits with a stretched exponential of the form $I = Ae^{-(2\tau/T_2^*)^\beta}+B$ (not shown here). The fits did lead to $0.76 \leq \beta \leq 1.19$, whereas β decreases for increasing temperature. A decrease of β to values of $\beta < 1.0$ would indicate the critical slowing down of the relaxation below a critical temperature. However, values of $\beta > 1.0$ are not expected in this picture, but definately necessary for a better fit, based on the curvature of the echo decay in a logarithmic plot. Therefore, a stretched exponential is not suitable to describe the observed echo decay.

To summarize we cannot assign the deviation from a monoexponential decay clearly to one of these mechanisms.

Measuring at zero field has the advantage of the virtual absence of ESEEM effects. This enables us to determine decoherence times with higher accuracy than at finite fields, without the disadvantage of long selective pulses, which could suppress ESEEM effects at finite fields.

A strong temperature dependence of T_2^* can have different reasons: First, the dependence can be due to dipolar interactions if the dilution limit is not reached yet [20]. In the case of non-negligible dipolar interactions temperature-dependent spin flip-flops lead to decoherence. Coherence times did not prolong significantly (see Fig. 6.8, $T_2^* = 651 \pm 20$ ns for 0.2 mg/ml compared to $T_2^* = 559 \pm 20$ ns for 0.5 mg/ml) for lower concentrations than the used 0.5 mg/ml in this study. This indicates that dipolar interactions are not the main decoherence pathway.

An additional decoherence process is the Fe_4 nuclear spin bath decoherence. Hyperfine contact interactions between the nuclear spins surrounding the elec-

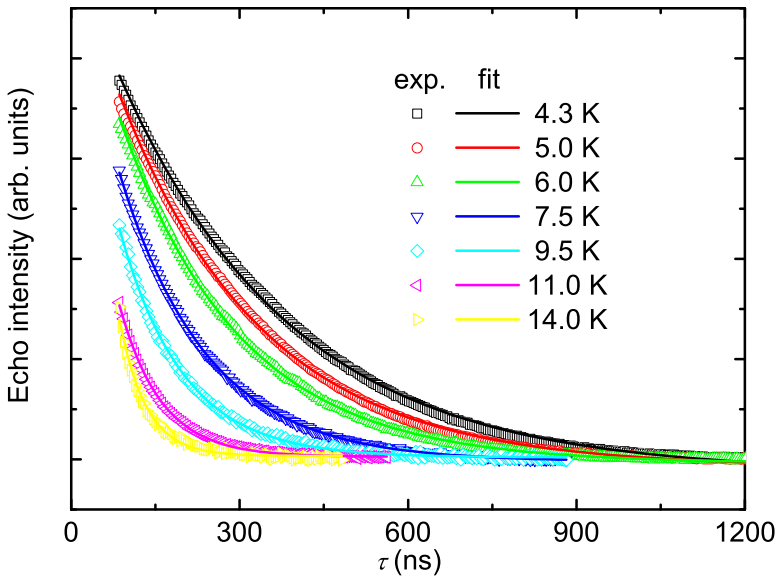

Figure 6.6: Integrated Hahn echo intensity for Fe_4 in toluene. The data were rescaled so that intensities at zero delay time would match. The experimental data (symbols) were fitted monoexponentially (lines).

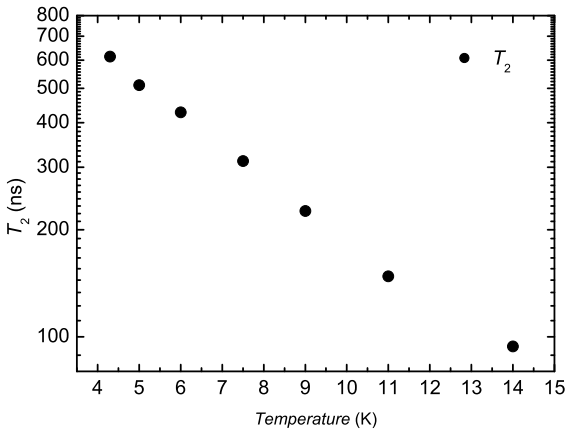

Figure 6.7: Temperature dependence of T_2^* from monoexponential fit

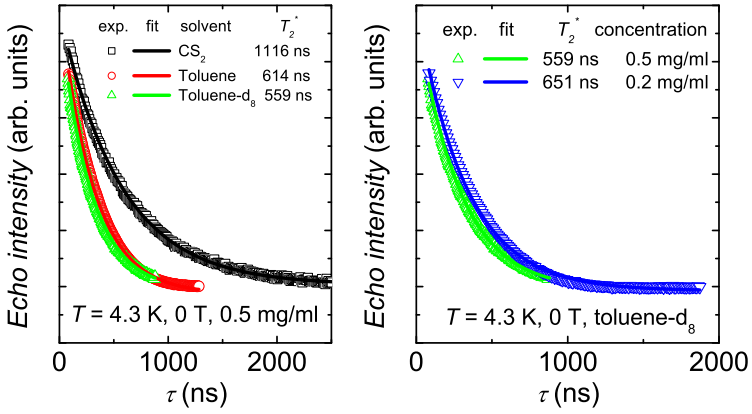

Figure 6.8: Echo intensity after a Hahn echo sequence for three different solvents (left) and two different concentrations (right) at 0 T and 4.3 K. The data were rescaled so that intensities at zero time would match. The experimental data (symbols) was fitted monoexponentially (lines) which gives the time constants T_2^* shown in the legend.

tron spin lead to spontaneous spin-flip processes [21]. The decoherence modeled by a spin bath is a complex problem, and the temperature dependences of decoherence rates are not easily obtained. Therefore the temperature dependence of decoherence rates is not studied in detail here. Nevertheless the ESEEM study in the next section shows coupling to the nuclear spin bath, in this case represented by the solvent molecules, is indeed the main decoherence process.
In a spin echo experiment the fast decoherence due to the inhomogeneity in the effective nuclear field (Overhauser field) is suppressed due to the refocusing which is induced from the echo. These fast relaxation processes therefore do not play any role in the relaxation observed in our experiments.

A higher dilution leads to a slightly higher coherence time, comparing the measurements in toluene-d_8 at 0.5 mg/ml and 0.2mg/ml. Considering the expected factor of 0.4 in magnetic dipole-dipole interaction (the energy is proportional to $\propto 1/r^3$ whereas the distance r of the molecule depends on the concentration c with $r \propto \sqrt[3]{1/c}$) and the errors in relaxation time and temperature, this shows that measurements at 0.5 mg/ml can already be considered to be in the high dilution limit.

The echo decay of Fe_4 in deuterated toluene compared to the measurement in non-deuterated toluene does not show a significant difference in relaxation time, whereas choosing a solvent with virtually no nuclear spins (CS_2, see Chapter 6.2) leads to a spin-spin relaxation time enhancement by about a factor of two.

The ratio T_2^*/T_1 is almost constant over the measured temperature range ($0.58 \leq T_2^*/T_1 \leq 0.65$). The general limitation $T_2^* \leq 2T_1$ [9] is not violated by this ratio. Nevertheless the found constant ratio suggests that T_2^* is limited by T_1. However the field dependence of T_2^* and T_1 shows that there is no direct relation between T_2^* and T_1 (see Chapter 6.3.1 and Chapter 6.3.1).

Electron Spin Echo Envelope Modulation (ESEEM)

To observe an ESEEM signal a two-pulse Hahn echo sequence was used. In nonzero field the nuclear spin levels split and the coupling of the electron spin to the nuclear spin leads to a modulation of the echo signal (Chapter 2.2.4). We recorded ESEEM curves at fields between 0 T and 4 T. At fields > 0.5 T the modulation depth was too small for the determination of the ESEEM frequency. At low fields the splitting of the nuclear spin levels is small and therefore the modulation frequency is low. In consequence it is not possible to determine the ESEEM frequencies because the echo is decayed before a full modulation period has passed. We studied the modulation of the echo in toluene, toluene-d_8 and carbondisulfide (CS_2) at 0.373 T at a concentration of 0.5 mg/ml at 4.3 K. The field at 0.373 T provides a good compromise between a significant modulation amplitude and the possibility to observe a full oscillation period.

The echo decay (Fig. 6.9(a)) was fitted with a monoexponential decay which is subtracted to gain the ESEEM intensity in Fig. 6.9(b). To be able to quantitatively analyze the ESEEM frequencies a fast Fourier transformation (FFT) was applied to the ESEEM intensity which is shown in Fig. 6.9(c). The echo decay itself shows weak oscillations for the solvents toluene and toluene-d_8. Surprisingly, a different oscillation period is clearly visible. For the measurement with CS_2 only for the first nanoseconds a dip in echo intensity is visible.

The subtraction of the monoexponential decay now clearly reveals the different oscillation frequencies in toluene and toluene-d_8. The dip in CS_2 turns out to match the first half of the oscillation period in toluene. The echo decay of all measurements turns out to be not purely monoexponential, this can be seen in the background which is still visible also for long time delays. This background seems to be particularly strong for the measurement in CS_2, but please note the

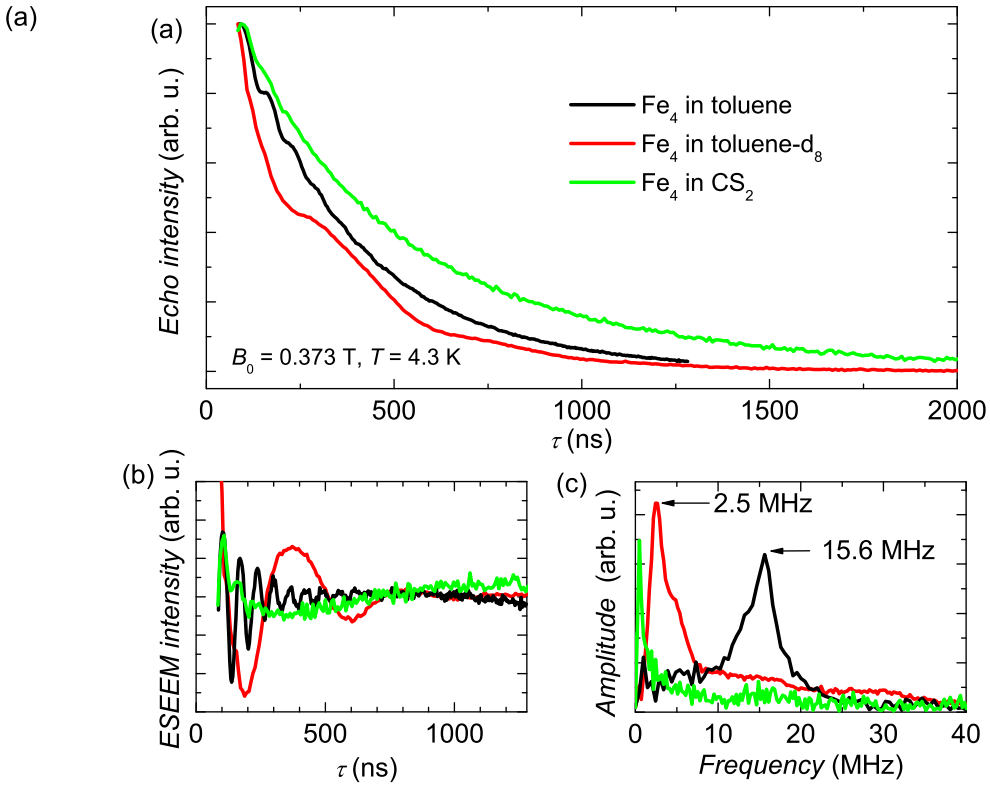

Figure 6.9: (a) Echo decay for Fe_4 in different solvents at 4.3 K.
(b) ESEEM intensity after subtraction of exponential decay.
(c) ESEEM frequencies from FFT of the ESEEM intensity.

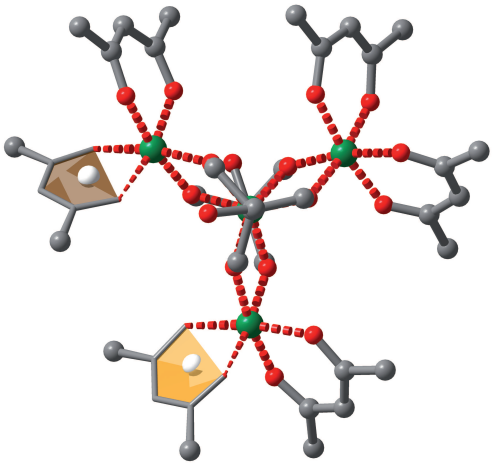

Figure 6.10: Fe_4 with Fe atoms in green. Two acetylacetate ligand planes are emphasized to visualize the possible π-stacking of aromatic solvent molecules in between these ligans.

arbitrary scaling of the ESEEM intensity, which enlarges the relative intensity in the case of CS_2.

In the Fourier transformed signal (Fig. 6.9(c)), the dominant ESEEM frequency in toluene turns out to be (15.6±0.3) MHz, whereas the one in toluene-d_8 is (2.5±0.2) MHz. For the measurement in CS_2 the FFT only shows a maximum at very low frequency, which is due to the background due to the non-monoexponential behavior of the echo decay. The first half-oscillation leads to an easily overlooked shoulder around 15.6 MHz.

Analysis. In the case of Fe_4 in toluene the observed frequency matches the free Larmor frequency of protons at 0.373 T (15.9 MHz). For Fe_4 in toluene-d_8, the dominant frequency in the measurement corresponds to the free Larmor frequency of deuterons (2.4 MHz) at this field.
Interestingly, this means that we observe that the electron spin is coupled to the nuclear spin of the solvent rather than to the 58 protons of the Fe_4 molecule itself. In CS_2, the dip indicates that a small coupling to the intramolecular protons is present as well.

Exchange interactions are not expected for non-covalent bonds between electron spin and nuclear spins of the solvent. It is possible for aromatic molecules like toluene to π-stack between two acetyl acetonate ligands (see Fig. 6.10). These ligands have a distance of about 7 Å, which is sufficient for π-stacking. If π-

stacking takes place, the Fe atoms are close to the hydrogen or deuterium atoms of toluene and toluene-d_8, which can induce significant dipolar interactions between electron spin and nuclear spins of the solvent.

This is the first time to our knowledge that a coupling to the surrounding solvent nuclear spins was observed for SMMs.

Field Dependence of T_1

To gain insight into the field dependence of the relaxation time, T_1 was measured in CS_2 at several fields between 0 T and 4 T at 4.3 K. The reason for performing field dependent measurements is the negligible ESEEM intensity superimposed to the echo signal, if CS_2 is used as a solvent. This improves the accurancy of the determined values of T_1 significantly. Again a standard inversion recovery sequence ($\pi - \tau - \pi/2 - \tau_{\text{fixed}} - \pi - \tau_{\text{fixed}} -$echo) was used. The obtained exponential decay was fitted with the monoexponential function $1 - e^{-\tau/T_1}$. The obtained values for T_1 are plotted in Fig. 6.11. The echo decay plots themselves are not shown here.

Analysis. The relaxation time is almost constant (average relaxation time: 940±20 ns) for fields between 0 T and 1 T. For higher fields, the relaxation time increases, here both excited levels of the ground multiplet and perpendicular transitions are excited. The reason for the increase in T_1 is not clear. The error in T_1 also increases for fields $B_0 > 1$ T due to a decreasing absolute echo signal at higher fields (see section 6.3.2).

It was possible to study the dependence of spin-lattice relaxation times T_1 over a broad field range, this was due to the orientation distribution of molecules in the frozen solution. For low fields (<0.6 T) we expect only to excite the ground state transition m_S=-5→-4, whereas for higher fields one expects to excite both excited state and ground state transitions. No echo signal is expected if the relaxation time of the excited state transition is too short. In other experiments ([20], [62]) no echo signal was observed for excited spin states, which indicates shorter relaxation times for excited states. In consequence, we assign all relaxation times up to 2 T being from Fe_4 molecules. At fields around 3.36 T decomposition products are expected to be present and to dominate the echo signal. Therefore the relaxation times obtained at these fields are assigned to decomposed Fe(III) ions.

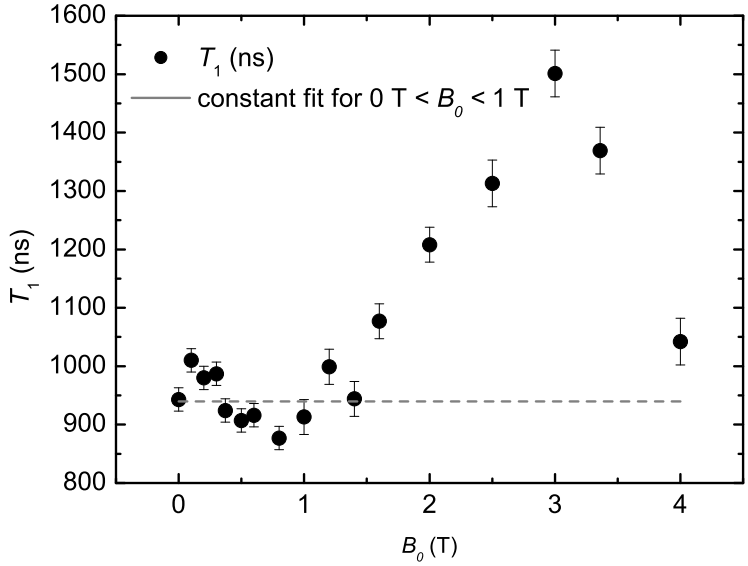

Figure 6.11: T_1 of Fe_4 at different fields in CS_2 at 4.3 K. For fields higher than 1 T the error increases due to decreased echo intensity.

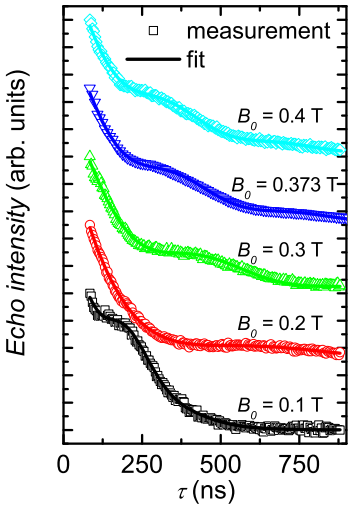

Figure 6.12: Experimental Hahn echo intensities (symbols) and fits (drawn lines) as a function of delay time for Fe_4 in toluene-d_8 at different magnetic fields as indicated. See text for further details.

Field Dependence of T_2^*

The coherence time T_2^* of Fe_4 was measured at different fields from 0-4 T (in CS_2) and from 0-2 T in toluene-d_8 at 4.3 K. We applied a standard Hahn echo sequence ($\pi/2 - \tau - \pi - \tau -$ echo) with an initial time delay of 86 ns. For both solvents the same concentration (0.5 mg/ml) was used. The data was fitted with the monoexponential decay function $Ae^{-2\tau/T_2^*} + B$. For nonzero fields we observe ESEEM modulation of the echo signal. For the measurements in toluene-d_8 at low, but nonzero fields (0.100 T, 0.200 T, 0.300 T, 0.373 T, 0.400 T) the ESEEM modulation complicates the determination of the decay time. A superimposed decaying sine function was used for the fit: $e^{-2\tau/T_2^*}\,(A\sin(\omega_L\tau - \tau_0) + B)$, where ω_L is the free Larmor frequency of the ^{2}H nucleus. A and B are the amplitudes for the decaying sine function and the background echo decay, respectively. The reason for the application of this fit function is given in Chapter 2.2.4. For the measurement at 0.1 T fitting the experimental data did not lead to a satisfactory fit, therefore here also the modulation due to ^{1}H nuclei has been taken into account: $e^{-2\tau/T_2^*}\,(A\sin(\omega_{L1}\tau - \tau_0) + B\sin(\omega_{L2}\tau - \tau_0) + C)$, where ω_{L1} is the free Larmor frequency of ^{1}H and ω_{L2} is the free Larmor frequency of ^{2}H. All fits

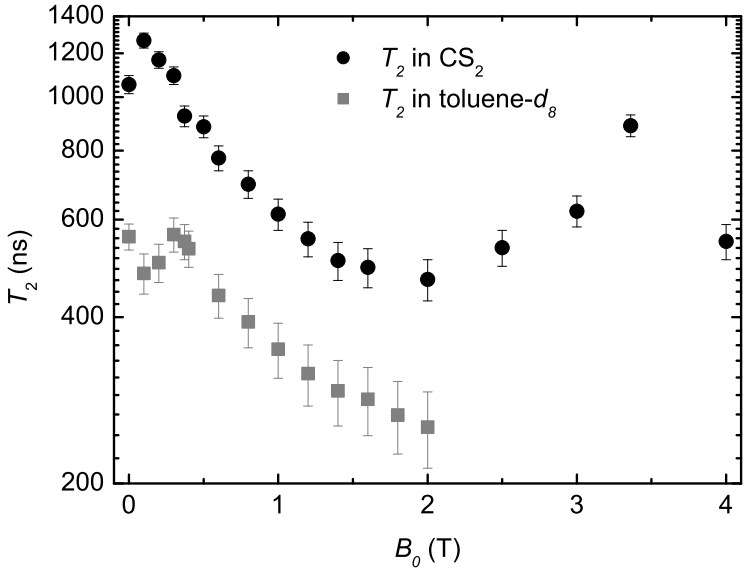

Figure 6.13: Field dependence of T_2^* in CS_2 and toluene-d_8 at 4.3 K.

with taking the ESEEM signal into account are shown here to demonstrate the accuracy of the fit (see Fig. 6.12). The obtained coherence times T_2^* are shown in Fig. 6.13. Coherence times in CS_2 are significantly higher than in toluene-d_8, the maximum value for T_2^* was determined to be 1270 ± 40 ns (for Fe_4 in CS_2 at 0.1 T). For $0 < B_0 < 0.3$ T T_2 is longer than T_1.

Analysis. At first sight, the decrease in T_2^* with field may seem surprising, given that the nuclear spin bath becomes increasingly polarized in higher fields. In more polarized spin bath nuclear spin-flip decoherence processes are suppressed. However, even at 2 T and 4.3 K the polarization of the nuclear spin bath is only 0.1%. [1] Therefore, the polarazation of the nuclear spin bath will be negligible.

[1] In our case of a highly diluted frozen solution, the spin bath is represented by intramolecular and solvent nuclear spins. In the following we will calculate the spin bath polarization for the case of proton nuclear spins at 4.3 K. To do so, we calculate the Boltzmann population ratio $N_{I=-1/2}/N_{I=1/2}$ of the two levels split by the external magnetic field B_0 by $\Delta E = \hbar\gamma B_0$. $N_{I=-1/2}/N_{I=1/2} = exp((\hbar\gamma B_0)(\mathrm{k}T) \approx exp(-4.75 \cdot 10^{-4} B_0/\mathrm{T}) \approx 1 - 4.75 \cdot 10^{-4} B_0/\mathrm{T}$. For a field of 2 T this leads to a population ratio of $N_{I=-1/2}/N_{I=1/2} \approx 0.999$, which corresponds

The suppression of decoherence by choosing a virtually nuclear spin free solvent (CS_2) was already shown in Chapter 6.3.1. All coherence times in CS_2 at different fields are about a factor of 1.75 higher than in toluene-d_8 for $B_0 < 2\,\mathrm{T}$. This supports the interpretation that removing the solvent nuclear spins leads to increased coherence times. We do not have any explanation for the decreasing coherence times for fields $0 \leq B_0 \leq 2\,\mathrm{T}$. The ratio T_1/T_2^* is not constant for all fields, which indicates that T_1 is not the only limiting mechanism for T_2^*.

6.3.2 Echo-detected ESR

To investigate the hyperfine coupling to nuclear spins more clearly, echo-detected ESR spectra were recorded at 4.3 K for Fe_4 in toluene, toluene-d_8 and CS_2. We used a standard Hahn echo sequence ($\pi/2 - \tau - \pi - \tau -$ echo) with a fixed time delay of 186 ns and an integration window of 80 ns.

Fig. 6.14 shows the normalized echo intensity recorded in the the range of 0-4 T (in toluene-d_8 and CS_2) and in the range of 0-2 T (in toluene). The data was recorded in two measurements for each solvent, which explains the different signal to noise ratio for 2-4 T in CS_2.

Over the whole field range measured a spin echo can be observed. The zero baselines cannot be given because all data was recorded without phase cycling, which causes a background signal to be present.

For all solvents, the echo intensity shows oscillations at low fields (<0.7 T), then a decrease of echo intensity up to about 2.5 T. The increase of echo intensity for fields higher than 2.5 T leads to a maximum at 3.39 T for the measurements in toluene-d_8 and CS_2. A smaller maximum (in CS_2) and a shoulder (in toluene-d_8) in echo intensity can be observed at 3.30 T. We assign the maxima in echo intensity around g=2 (3.36 T) to decomposition products present in the solution. The peaks around 1.7 T in the echo intensity of the measurement of the sample with Fe_4 in CS_2 we assign to stability problems in the measurement.

Analysis. The oscillation in echo intensity visible in all solvents for fields up to about 1 T is due to nuclear modulation effects. This effect can be understood quite easily: In echo decay measurements (time domain) the modulation leads to minima and maxima with the period of ω_n^{-1}. For field domain measurements maxima positions can be calculated as follows: With a fixed delay time τ the n-th

to a polarization of 0.1%.

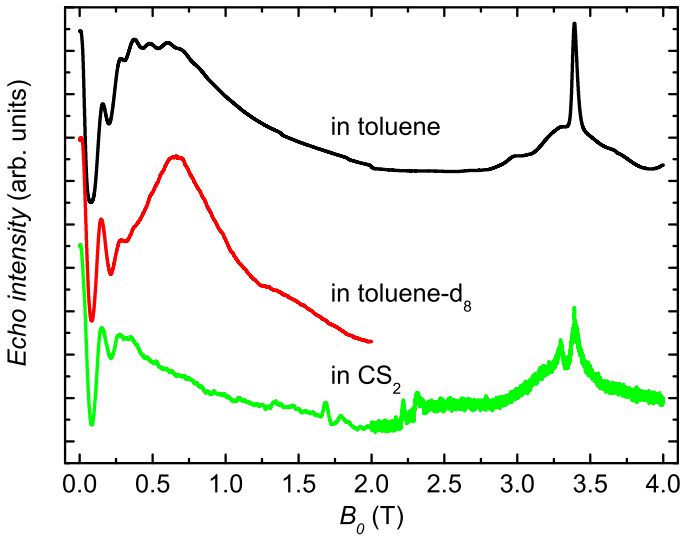

Figure 6.14: Echo detected ESR of Fe_4 in different solvents at 4.3 K. The data was rescaled and shifted for clarity.

maximum can be found at the field B_n: $B_n\gamma = \omega_n$, where γ is the gyromagnetic ratio of the nucleus coupled to the electron spin. Using $\omega_n = \frac{2\pi}{n\tau}$ we obtain $B_n = n\frac{2\pi}{\gamma\tau}$.

τ can not be given exactly because the pulse lengths are not infinitesimally short. With τ_{fixed}=200 ns (distance in between the beginning of the pulses) one obtains for ^{1}H $B_n = n \cdot 0.117\,\text{T}$ and for ^{2}H $B_n = n \cdot 0.885\,\text{T}$.

The exact positions of the maxima may be shifted by the overall shape of the echo amplitude over field. The theoretical fields of five maxima in the spectrum in toluene were determined and are represented by blue vertical lines in Fig. 6.15. The positions of the first two expected maxima are the same for all three solvents and correspond to the theoretical positions of protons. Interestingly, this indicates that a coupling to intramolecular protons is present because in both toluene-d_8 and CS_2 no solvent protons are present. For the measurement on Fe_4 in toluene as many as five maxima are visible. This completes the results from ESEEM measurements (Chapter 6.3.1), where the coupling to intramolecular protons could only be tentatively shown.

The decrease in intensity for $0.2 \leq B_0 \leq 0.65\,\text{T}$ in the spectrum of the toluene-

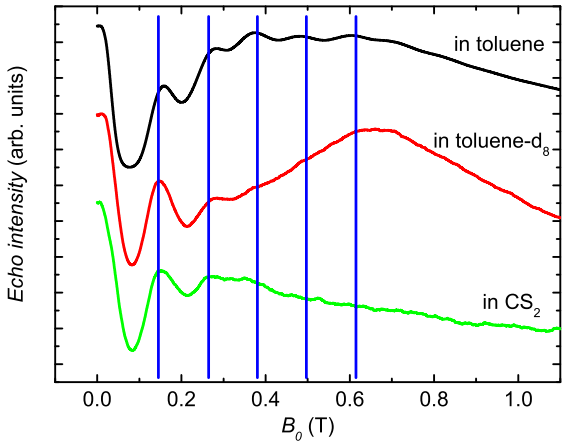

Figure 6.15: Echo detected ESR in the field range from 0 T to 1 T. Vertical blue lines indicate at which positions maxima in intensity for a nuclear modulation effect of ^{1}H are expected.

d_8 sample (Fig. 6.14) agrees with the expected echo intensity minimum due to coupling to ^{2}H nuclei at 0.41 T.

For higher fields all modulations disappear, because the nuclear modulation depth is proportional to B_0^{-2} [9].

The decreasing echo intensity for $B_0 > 0.4$ T is partly due to shorter coherence times for higher fields as shown in Chapter 6.3.1. The faster decoherence time at higher fields alone cannot explain the decrease in echo intensity with field, as it can be seen in Fig. 6.16. Therefore the number of molecules excited has to vary as well.

6.3.3 Rabi Oscillations

The observation of Rabi oscillation in a physical system demonstrates the coherent manipulation of the two levels [89]. For all measurements shown in this section the pulse sequence $a - \tau_{\text{fix}} - \pi -$ echo (see basics in Chapter 2.2.6) with phase cycling was used.

Other sequences capable of giving a direct measure of S_z after the nutation pulse a, like $a - T - \pi/2 - \tau_{\text{fix}} - \pi -$ echo with $T_1 \gg T \gg T_2$ were not applicable, because T_1 is in the order of T_2 for Fe_4 (see Chapter 6.3.1).

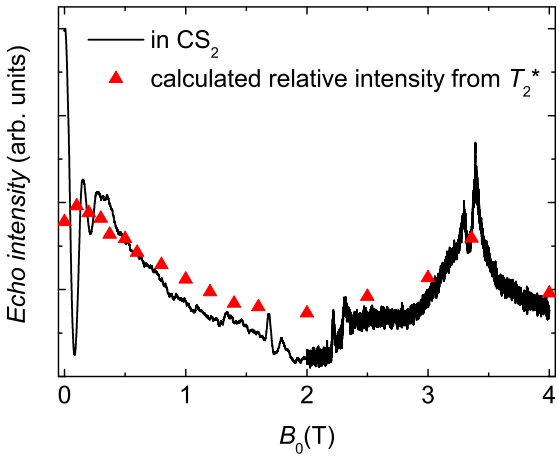

Figure 6.16: Field dependent echo intensity in CS_2 compared to calculated echo intensity from echo decay with T_2^* values from Chapter 6.3.1.

Data of measurements on different samples are not directly comparable, because the B_1 field strength depends on the coupling of the microwave cavity and dielectric absorption. Each plot in this section therefore only shows the data recorded on one particular sample with the same coupling.

Rabi Oscillations of Fe_4 in CS_2

Dependence on Magnetic Field. Fig. 6.17 shows the echo intensity recorded as a function of nutation pulse length at different external magnetic fields. The used sample was Fe_4 in CS_2 at a concentration of 0.5 mg/ml at 4.3 K. The π-pulse length was 32 ns. The data was rescaled so that the first oscillations (1) have the same amplitude, because the absolute amplitude depends on many experimental details, particularly it scales with the number of measurement cycles. All data are plotted in an overlapping manner to emphasize the similarities and differences. Except the echo intensity for B_0=3.36 T was reduced by a constant value for clarity. No subtraction of the background was possible because there were only few oscillations visible in these measurements.

The first extremum in echo amplitude (1) is at 22±2 ns for all fields except for 3.36 T, where $g = 2$. At this particular field the minimum is at 28±2 ns.

For the second extremum in echo amplitude (2) the intensities of the different

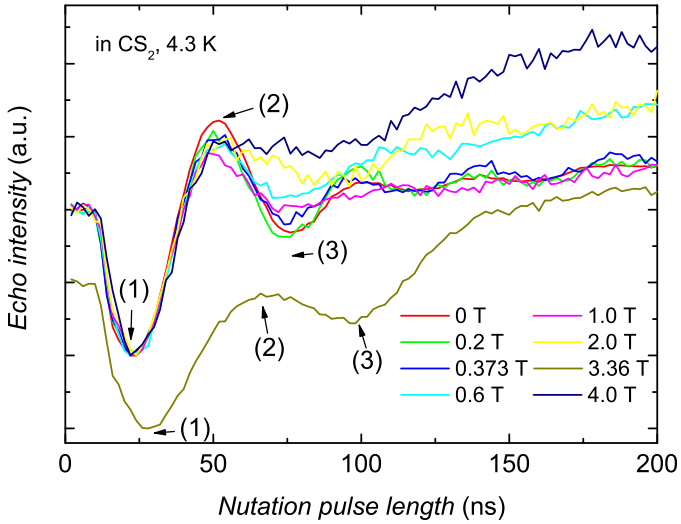

Figure 6.17: Rabi oscillations obtained by recording the echo intensity as a function of nutation pulse length in CS_2. The data was rescaled so that the first oscillations (1) have the same amplitude. The data for B_0=3.36 T was shifted by a constant value for clarity.

fields still match (at 52±2 ns). The only exception is the measurement at 3.36 T (68±2 ns for the maximum (2)) which has clearly a different Rabi period. The exact Rabi frequencies cannot be determined because with such a low number of Rabi oscillations a FFT is not suitable for analysis. Taking into account the distance of half a period (2)-(1) one obtains a Rabi frequency of 16.7±2 MHz for all fields expect for 3.36 T. Here the Rabi frequency is 12.5±2 MHz.

The third extremum reveals large differences in behavior at different fields: At low fields (<0.5 T) the extremum is pronounced and situated at 74±2 ns. At these fields further extrema can be observed for longer nutation pulse lengths. For higher fields the extremum is smeared out and shifted to longer nutation pulse lengths. The measurement at 3.36 T shows the extremum (3) at 96±2 ns.

Analysis. The fast decay of Rabi oscillations makes a detailed analysis impossible. Nevertheless we can gain different insights: The period of the Rabi oscillation depends on which transition is excited ([9], p. 429):

$$\omega_{\mathrm{Rabi}}(m_S, m_S+1) = A\sqrt{S(S+1) - m_S(m_S+1)}$$

Herein A is a prefactor, which includes the strength of the driving field B_1. As this field is not known, we have to compare the Rabi frequencies at the same B_1, to be able to make a statement about the transitions involved. From the measurement we can conclude that for all fields except 3.36 T we observe the same transition because the Rabi period does not vary strongly. The ratio of the frequencies of the transition from $-5 \rightarrow -4$ to $-4 \rightarrow -3$ would be $\frac{\omega_{-5\rightarrow-4}}{\omega_{-4\rightarrow-3}} = \sqrt{5/9} \approx 0.75$.

The differing Rabi period at 3.36 T indicates that different spins are excited at this field. This may be impurities in the cavity or Fe(III) ions in decomposition products. This supports the measurements of relaxation time and coherence time at 3.36 T, whose values differed strongly from neighboring fields.

We assign the fast decay of the Rabi oscillations to the distribution of zero-field splitting parameters (D strain) and the different orientations of the molecules. Therefore, at the same field, different molecules (with different D and different orientation) will be excited. This causes a superposition of Rabi cycles with different frequencies which then lead to a rapid decrease in Rabi amplitude for long delay times.

Dependence on Microwave Power. One important characteristics of Rabi oscillations is the linear microwave power dependence of the Rabi frequency. Three different driving field strengths were used by applying the tunable attenuator of the W-Band amplifier. This attenuator is controlled using an electrical current. Two different current values were used, corresponding to an attenuation of 1.5 dB and 3.0 dB. The driving field strength ratios $B_1/B_{\max}$ for this attenuations are 0.84 and 0.71, respectively. Due to the limited accuracy of the current set and the error in reading of the current-attenuation dependence the error of these values is given by ± 0.02.

The echo intensity as a function of nutation pulse length (pulse sequence as above) is shown in Fig. 6.18. As the field strengths of the π-pulses also vary it is clear that these pulse are shorter than an ideal π-pulse for the measurements with attenuator. The data has been processed as follows before plotting: First, the data points at short nutation pulse lengths which led to negligible echo intensity were eliminated, then a point reflection of the data at zero intensity, zero nutation pulse length has been performed. After that the background was determined by smoothing the data with a FFT filter with an appropriate smoothing constant (60 ns) to obtain an oscillation-free background. This background was subtracted, then the data was rescaled to match the echo intensities of the first oscillations. This data processing was useful to increase the quality of the FFT by reducing

effects of the negligible intensity points, which otherwise lead to a strong signal at low frequencies.

Analysis. The observed oscillations are clearly power dependent. For lower microwave field strength the periods increases. This is supported by the FFT of the processed data shown in the inset of Fig. 6.18. For higher driving field strength the dominant frequency is higher.

To obtain a quantitative picture in the limitation of only three different driving field strengths, the following analysis was carried out: Each FFT (shown in the inset of Fig. 6.18) was fitted with a Gaussian lineshape and the center frequency was taken do be the dominant Rabi frequency. The widths of the Gaussians were 8.6 GHz ($B_{\max}$), 7.2 GHz ($0.84B_{\max}$) and 5.7 GHz ($0.71B_{\max}$). Due to these very large linewidths the error of the dominant frequency is assumed to be 1.0 GHz. The dominant frequencies are plotted as a function of driving field strength in Fig. 6.19. The red line is a linear fit to the data points. Considering only the error in dominant frequency, the abscissa is (-3.1±4.2) MHz.

The main result of this measurement is that the Rabi frequency is power dependent. The data processing was necessary to obtain a quantitative picture. The results are consistent with a linear power dependence. Although the three data points can be fitted with a straight line and the abscissa of 0 lies within the error, many more different powers are necessary to prove a linear dependence. Additionally the pulse length of the second pulse would have to be adapted to keep the value $B_1 t_\pi$ constant, where t_π is the π pulse length.

Rabi Oscillations of Fe_4 in toluene

To study the influence of the solvent on the Rabi oscillations, similar measurements like in the previous section were performed on a 0.5 mg/ml Fe_4 in toluene-d_8 sample at 4.3 K. The echo intensity as a function of a variable nutation pulse length is shown in Fig. 6.20. In this case, only the echo intensity of the first oscillation was normalized, no further background correction was performed. Clearly visible are the first 8 ns with negligible echo intensity. We assign this behavior to the limited switching speed of the pin diodes which prepare the pulses. For both fields at 0 T and 0.373 T the first 5 oscillation periods are observable. It was possible to perform a FFT of the time-domain signals leading to a broad distributions of similar frequencies for both 0.0 T and 0.373 T.

The goal of the following measurement was to compare the Rabi oscillations

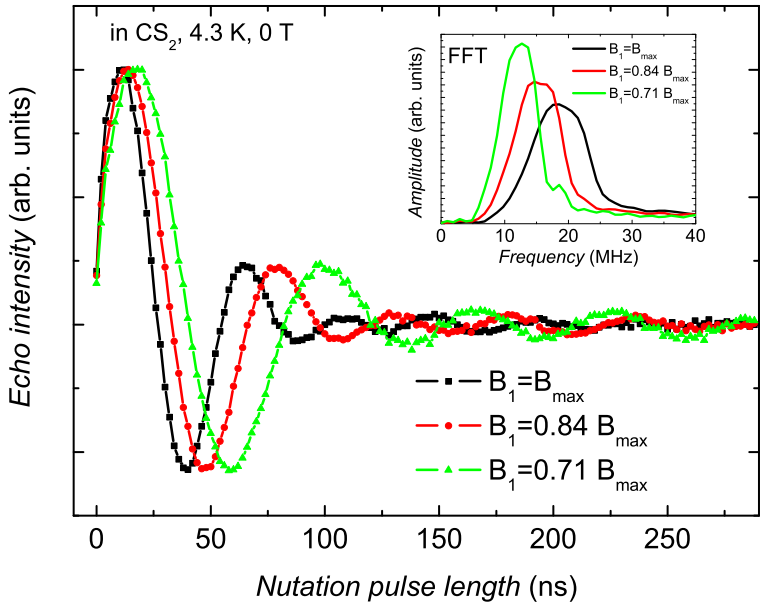

Figure 6.18: Rabi oscillations obtained with different driving field strengths B_1. The plot shows treated data according to the procedure described in the text.

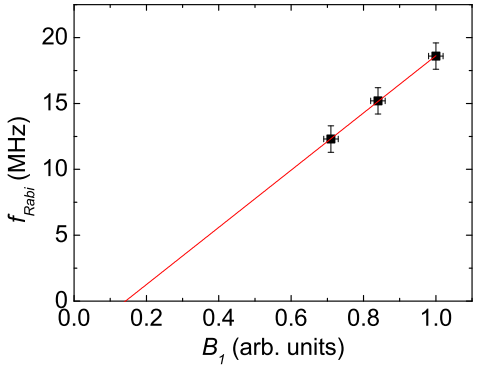

Figure 6.19: Dominant Rabi frequency dependent on driving field strength. The red line is a linear fit of the data points.

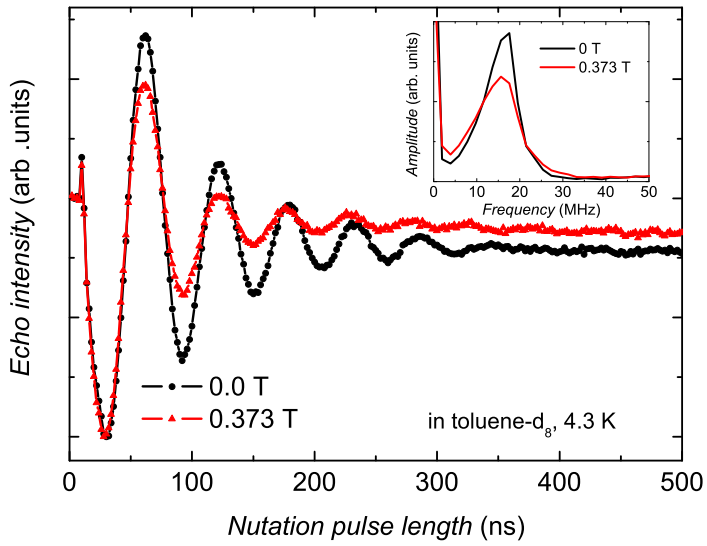

Figure 6.20: Rabi oscillations at different magnetic fields B_0 in toluene-d_8. The data was rescaled so that the maxima of the first oscillation match. Inset: FFT of the time domain data.

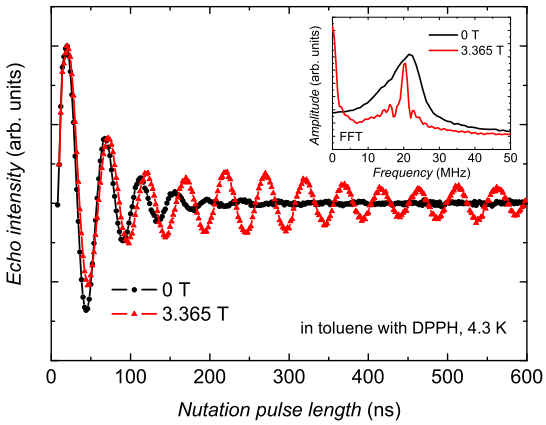

Figure 6.21: Rabi oscillations at different magnetic fields B_0 in toluene with added DPPH. The data were rescaled so that the maxima of the first oscillation match. Inset: FFT of the time domain data.

of Fe_4 with the one of the stable radical 2,2-diphenyl-1-picrylhydrazyl (DPPH) to determine the transition which is excited in the experiment. This radical is commonly used to determine the exact magnetic field in ESR spectrometers, because its g-value is known with high precision ($g = 2.0036$) and it has a small linewidth ($\approx$0.2 mT at room temperature at $\approx$100 GHz [90]). However, in solution the line broadens and exhibits a superimposed structure of hyperfine couplings ([90]). The measurements were done on a frozen solution with both Fe_4 (0.2 mg/ml) and DPPH from Aldrich (undetermined, but small concentration) in toluene. Both CW measurements and pulsed measurements close to g=2 did not show significant influence of the added DPPH compared to the background signal due to impurities in the cavity. This made it difficult to determine the field at which mainly DPPH spins are excited. Therefore the measurement at 3.365 T ($g = 2.0080$) shows the behavior of a spin ensemble of both impurities and DPPH spins. It has to be noted that with the used shot repetition time of 459 μs no influence of the proceeding pulse sequence will be present for Fe_4 but not necessarily for the impurities or DPPH. This is due to the T_1 of Fe_4 in the order of 1 μs, which is much smaller than the shot repetition time. For DPPH T_1 at 4.3 K was not determined. For impurities at 3.36 T, the spin-lattice relaxation time T_1

was determined in Chapter 6.3.1 and found to be in the same order of magnitude (1.35 μs) compared to the one of Fe_4. This means that also for impurities no effects of the proceeding pulse sequence can be expected.

Fig. 6.21 shows the echo intensity after a variable nutation pulse length at 0.0 T and 3.365 T of the described solution with added DPPH. The data was processed as follows before plotting: First the data points at short nutation pulse lengths which led to negligible echo intensity were taken off, then a point reflection of the data at 0 intensity, 0 nutation pulse length was performed. After that the background was determined by smoothing the data with a FFT filter with an appropriate smoothing constant (60 ns) to obtain an oscillation-free background. This background was subtracted, then the data was rescaled to match the echo intensity of the first oscillation.

At both fields for short nutation pulse length, a similar behavior can be observed. At longer nutation pulse length, the Rabi oscillations at 0.0 T decay fast, in contrary at 3.365 T significant oscillations for nutation pulse lengths persist longer than the maximum measured pulse length of 600 ns. The envelope of the oscillations for a nutation pulse length $n > 150$ ns indicates a beating; this would mean that two differing, but close frequencies are present. The inset of Fig. 6.21 shows the FFT of the intensity data. The measurement at 0 T shows a broad distribution of frequencies with a dominant frequency of 21.5±2 MHz. This broad distribution is also present at 3.365 T, but the dominant frequency of the longliving oscillations has a significantly smaller width and is centered at 20.5±0.5 MHz.

Analysis. The measurements of Fe_4 in toluene bring us to the following insights: First, the decay of the Rabi oscillations is slower than in the sample dissolved in CS_2 (see Chapter 6.3.3), despite the fact that the shorter coherence times in toluene give rise to the expectation that the oscillations should decay faster. We have no explanation for this behavior, but is shows that for the ability to coherently manipulate spins not solely the coherence time is crucial. Second, it was not possible to compare the Rabi frequency of Fe_4 with the one of DPPH. Still we demonstrated by the measurement at zero field and 3.365 T that we observe a different compound around 3.365 T. Rabi frequencies for different compounds are expected to differ, due to the different transitions probabilities. The observed equal frequencies are surprising.

6.4 Conclusions

The first direct observation of quantum coherence in a single-molecule magnet paves the way for further studies on the coherent properties of SMMs. The next step are the preparation of entangled quantum states, like the Greenberger-Horne-Zeilinger (GHZ) state, of coupled SMMs.

It can be expected that for lower temperatures than the accessible 4.3 K coherence times in Fe_4 can also be determined in single crystal samples, because the fluctuations of neighboring electron spins causing decoherence decrease for lower temperatures. Therefore pulsed ESR measurements at low temperatures and high fields (and therefore also higher microwave frequency) on single crystal samples of Fe_4 are promising.

The measured coherence times T_2 of Fe_4 in CS_2 are close to the limit $T_2 < 2T_1$. In consequence, a further reduction of electron-nuclear spin interaction will lead to a limitation of T_2 given by the relaxation time, this relaxation is governed by an Orbach process. This suggests a general restriction of coherence times in high-spin systems, which would make low temperatures ($< 5\,\mathrm{K}$) essential for practical applications.

Chapter 7

Summary and Conclusions

The aim of this thesis was to investigate the superposition of quantum states and coherent properties of molecular magnets. Quantum coherence, i.e. the ability of the wavefunctions of two objects to interfere one with another, requires a fixed phase relationship of the involved wavefunctions. In coherent systems, the superposition of states is possible, in which all basis states are simultaneously present. This concept is well known in quantum mechanics since its birth, and has great fundamental significance as it could be considered, in Schrödinger's words, the characteristic effect of quantum mechanics.

In addition to their fundamental interest such superposition states can be useful for quantum computing, a way of data processing that may be able to solve problems which cannot be solved with a classical computer. As the funding principles rely on different physics, some possibilities are open that are otherwise prohibited in classical computing. Algorithms of interest include the factoring of large numbers, and unbreakable quantum codes [91]. The first steps in the direction of quantum computing were made using NMR spectroscopy, entangled photons and Rydberg atoms. Anyway, it is likely that real steps forward will only be made if true solid-state quantum devices can be produced. The challenge is considerable, as any of these system exhibits coupling to the environment, leading to a loss of coherence within a relevant timescale, given by the decoherence time T_2 [21]. Because long coherence times are needed for quantum computing [1], it is necessary to study both the coherence times and the decoherence pathways that influence it. The latter are particularly interesting as they provide physical insight on the relative importance of several decoherence mechanisms present in different systems, and also allow determining how molecules can be tailored to enhance coherence.

This thesis can be inserted in this perspective. It considers the spectroscopic and coherent properties of a class of magnetic molecular compounds called molecular magnets, which are interesting model systems for quantum computation in

the solid state using electronic spins. In particular these magnetic molecules, being monodisperse and very well-described by a spin Hamiltonian approach, offer clean systems to study the physics of nanomagnets and phenomena associated to decoherence.

This thesis has had a multidisciplinary approach to the problem, comprising chemically-tailored systems that were investigated with a variety of techniques. To this aim new instrumentation and methodologies were expressly developed, so as to gain direct access to the magnetic energy level structure of molecular systems and probe the chemical and physical parameters affecting their magnetic properties.

Chapter 1 introduces the basic concepts in molecular magnetism, such as the spin Hamiltonian formalism, which is used to describe the physics of key phenomena like magnetic anisotropy and quantum tunneling of the magnetization.

In Chapter 2, besides introducing the basics of pulsed ESR, we describe the experimental setups used for ESR measurements. This background clarifies the motivation for the novel high-sensitivity broadband ESR setup built during this thesis, as described in Chapter 3, where we report its characteristics and the test measurements performed. By designing a cylindrical transmission cavity with tunable height, we could combine the high sensitivity of a resonant cavity setup (quality factor $Q > 1000$) with the frequency tunability of transmission setups ($Q = 1$). Broadband microwave elements, like coaxial transmission lines and a synthesized sweeper source in a network analyzer system, are necessary to measure in this frequency range. The setup can be operated at temperatures from 1.5–300 K and in a field range of 0-10 T. The upper working frequency range is limited to 40 GHz; by incorporating dielectrics in the cavity, we can extend the operating range of the setup to frequencies as low as 5 GHz. The unique possibilities of the technique were used to study the spin-forbidden transitions close to the avoided level crossing between two spin states of a molecular magnet. The V_{15} molecular magnet was used as a sample, as the physical origin of the avoided level crossing could not be unambigously assigned [2]. Tentative explanations include an assymetry in the molecular structure, assymetric exchange interaction and hyperfine interactions. By detecting the normally-forbidden transition between the $S = 1/2$ and $S = 3/2$ spin multiplets in a $\vec{B}_0 \| \vec{B}_1$ magnetic field configuration, we could plot the topography of the level crossing near the crossing field, and conclude that an interaction which mixes the different spin levels, like antisymmetric exchange interaction or hyperfine interactions, is necessarily involved in the observed transitions.

In Chapter 4, we present CW and pulsed W-Band ESR measurements on the $S = 1/2$ antiferromagnetic molecular ring Cr_7Ni. While the relaxation of the magnetization in molecular magnets was extensively studied, little is known about their coherent properties. These coherent properties, as mentioned above, are crucial both for the basic understanding of the quantum-to-classical transition and in quantum information processing applications. By comparing the obtained spin-lattice relaxation times at different fields in a diluted frozen solution of Cr_7Ni, we can exclude that a direct spin-phonon relaxation process is responsible for the spin-lattice relaxation. The phase memory time T_2^* was found to be (357 ± 10) ns at 5 K at W-Band frequency, which is comparable to the value found at X-Band frequency ((379 ± 10) ns at 4.5 K [3]). T_2^* sets a lower limit for T_2, because for the phase memory also other processes than spin-spin relaxation play a role. Using pulsed ENDOR spectroscopy, we could assign the main decoherence path to hyperfine coupling of the electron spin to intramolecular protons. Mims ENDOR measurements quantified the hyperfine coupling constant to $a_{\mathrm{iso}} = (-0.80 \pm 0.05)$ MHz, whereas the coupling strength shows a distribution (width: $\mathrm{FWHM_{ENDOR}} = 0.55 \pm 0.05$ MHz) due to the different distances of protons to the electron spin system in the molecule.

Chapters 5 and 6 deal with single-molecule magnets of the Fe_4 family. Single-molecule magnets are a special class of molecular magnets, showing slow relaxation of the magnetization at low temperatures, and thus exhibiting magnetic properties of purely molecular origin. First, we studied the magnetic properties of two Fe_4 derivatives in both powder and solution, determining the effect of the environment on the molecular magnetic properties. For a single-molecule magnet, the magnetic properties are usually treated as single-molecule properties, rather than properties of an ensemble, neglecting the influence of the surrounding. This can be a sound assumption at first, but when concerned with coherence and subtile quantum states, interactions with the environment can play an important role. For example, small distortions in the molecular structure, may lead to a different energy level structure, when the molecules are not arranged in a single crystal. The chemical possibilities of single-molecule magnets allowed using a chemical approach to study single-molecule magnets in frozen solutions, thus limiting intermolecular magnetic dipolar interactions.

We characterized two Fe_4 derivatives: $[Fe_4^{III}(acac)_6(Br\text{-}mp)_2]$ **(1)** and $[Fe_4^{III}(acac)_6(tmp)_2]$ **(2)**. AC susceptibility measurements show slow relaxation of the magnetization without long-range order and a variation of both the magnetization reversal barrier and the attempt frequency rate when the nanomag-

nets are dissolved. This could be assigned to distortions of the molecule in the frozen solvent matrix and to the different speed of sound in the two media, respectively. To determine the parameters of the spin Hamiltonian, which is important to describe the quantitative magnetic energy level structure of the molecule, we performed ESR measurements in the frequency and field domain. For **(1)**, simulating W-Band ESR data led to a negative uniaxial anisotropy with $D = (-0.3429 \pm 0.0005)\,\mathrm{cm}^{-1}$ using a $S = 5$ giant spin model; off-diagonal Hamiltonian elements were not necessary to reproduce the observed spectrum. Repetition of the procedures using W-Band ESR measurements on a frozen solution in different solvents indicated that the same spin Hamiltonian remained basically unvaried from the powder sample, with the axial anisotropy slightly increasing together with a significant increase of the linewidth. This result, on the one hand, confirms the validity of the ensemble-independent single cluster Hamiltonian used to describe the basic properties of single-molecule magnets, and, on the other hand opens the way for the measurement of the coherent properties, which are not directly described by the spin Hamiltonian and are strongly affected by ensemble effects. Moreover the obtained parameters, together with literature values from other Fe_4 compounds [4], stress the advantages of the chemical tunability of these compounds and the possibility of tuning the magnetic anisotropy by an appropriate ligand choice.

In Chapter 6, we present the first direct observation of quantum coherence in a single-molecule magnet. Single-molecule magnets are promising systems to be used as qubits, because the coherent manipulation in zero external field is possible, which simplifies any practical application. Moreover, in high-spin system the different magnetic sublevels can be used to implement improved algorithms, otherwise unapplicable on two-state qubits [5]. Coherence times, were expected to be in the order of 10 ns [6] [7] [8]. We could directly access the phase memory time by using pulsed W-Band ESR and we showed how, by deliberately changing the surrounding, coherence can be significantly enhanced. The phase memory time T_2^* of a high-spin cluster was obtained for **(1)** for the first time and was determined to be $T_2^* = 614\,\mathrm{ns}$ at 4.3 K in toluene. This value was obtained at a concentration where magnetodipolar interactions as a source of decoherence are negligible. Using the virtually nuclear-spin free solvent CS_2, we could further increase the phase memory time up to $1.27\,\mu\mathrm{s}$. We then went on examining the main decoherence mechanism in the system. By ESEEM (electron spin echo envelope modulation) spectroscopy and echo-detected ESR measurements it could be shown, that the electron spin is coupled to the nuclear spins of the solvent as

well as to protons within the molecule. The unique chemical composition of the molecular magnets also allowed identifying the reason of the strong coupling to the nuclear spins of the solvent, as the latter can form π-stacking structures between two ligands of the Fe_4 molecule. Analysis of the temperature dependence of the spin-lattice relaxation time T_1 reveals the importance of an Orbach process, which is a two-phonon process. Finally we could show that coherent electron-spin oscillations, also known as Rabi oscillations, can be induced in the system. The observation of such oscillations is a proof-of-principle for the viability of preparing a superposition state in the system, which is a prerequisite to perform quantum logic operations.

For Fe_4 dissolved in CS_2 at 4.3 K, T_1 and T_2^* have about the same value. If the intramolecular protons were to be replaced by a nuclear spin free ion in a gedankenexperiment, we would expect T_2^* to be limited by T_1 (because $T_2 < 2T_1$ [9]). Because excited spin states are most likely responsible for the Orbach process dominating the spin-lattice relaxation in high-spin systems, we can conclude that this is a general limitation for T_2 in SMMs. Therefore it is likely that long coherence times in single-molecule magnets will remain accessible only at cryogenic temperatures.

The observation of sizable coherence times in single-molecule magnets opens up new horizons. First of all, it will constitute the founding ground for the determination of the decoherence mechanisms active in single-molecule magnets, and their suppression by chemical and physical means. Further studies of coherence times in other high-spin molecules, or in Fe_4 at lower temperature in a crystalline sample, now look feasible and promising. In addition, the identification of the main decoherence processes hints at the path to be followed to chemically engineer these systems. One promising way could be the use of polyoxometalate-based molecular magnets, as these systems can be synthesized as nuclear spin free clusters. The next step ahead, i.e. the preparation of molecular-based systems with commutable interactions, can now be foreseen for the preparation of entangled quantum states. The observation, that the magnetic properties of SMMs can be retained in solution and coherence can also be enhanced, encourages further studies of SMMs in different environments. It also indicates that, while most studies will need to be performed on ensembles of molecular magnets due to sensitivity reasons, nevertheless the properties of the systems are directly accessible. This will then allow addressing the question of what happens in solution or on surfaces, and will also possibly give hints at what is to be expected in experiments probing magnetic properties of single molecules.

Bibliography

[1] S. L. Braunstein (ed.): *Quantum Computing*: WILEY-VCH, Weinheim, Germany (1999)

[2] B. Tsukerblat, A. Tarantul, A. Müller: Low Temperature EPR Spectra of the Mesoscopic Cluster V_{15}: The Role of Antisymmetric Exchange: *J. Chem. Phys.* **125** (2006) 054714

[3] A. Ardavan, O. Rival, J. L. M. Morton, S. J. Blundell, A. M. Tyryshkin, G. A. Timco, R. E. P. Winpenny: Will Spin-Relaxation Times in Molecular Magnets Permit Quantum Information Processing?: *Phys. Rev. Lett.* **98** (2007) 057201

[4] S. Accorsi, A. L. Barra, A. Caneschi, G. Chastanet, A. Cornia, A. C. Fabretti, D. Gatteschi, C. Mortalo, E. Olivieri, F. Parenti, P. Rosa, R. Sessoli, L. Sorace, W. Wernsdorfer, L. Zobbi: Tuning Anisotropy Barriers in a Family of Tetrairon(III) Single-Molecule Magnets with an S = 5 Ground State: *J. Am. Chem. Soc.* **128** (2006) 4742

[5] M. Leuenberger, D. Loss: Quantum Computing in Molecular Magnets: *Nature* **410** (2001) 789

[6] W. Wernsdorfer, D. Mailly, G. A. Timco, R. E. P. Winpenny: Resonant Photon Absorption and Hole Burning in Cr_7Ni Antiferromagnetic Rings: *Phys. Rev. B* **72** (2005) 060409

[7] E. del Barco, A. D. Kent, E. C. Yang, D. N. Hendrickson: Quantum Superposition of High Spin States in the Single Molecule Magnet Ni_4: *Phys. Rev. Lett.* **93** (2004) 157202

[8] A. Keren, O. Shafir, E. Shimshoni, V. Mauvaud, A. Bachschmidt, J. Long: Experimental Estimates of Dephasing Time in Molecular Magnets: *Phys. Rev. Lett.* **98** (2007) 257204

[9] A. Schweiger, G. Jeschke: *Principles of Pulse Electron Paramagnetic Resonance*: Oxford University Press, Oxford (2001)

[10] K. W. H. Stevens: In: *Magnetism*, eds. G. T. Rado, H. Suhl. Academic Press, New York (1963)

[11] M. Gerloch: *Ligand-Field Analysis*: Cambridge University Press, Cambridge (1984)

[12] E. M. Purcell: *Electricity and Magnetism*: McGraw-Hill, New York (1984)

[13] A. Abragam, B. Bleaney: *Electron Paramagnetic Resonance of Transition Ions*: Oxford University Press, Dover, New York (1986)

[14] L. Thomas, F. Lionti, R. Ballou, D. Gatteschi, R. Sessoli, B. Barbara: Macroscopic Quantum Tunnelling of Magnetization in a Single Crystal of Nanomagnets: *Nature* **383** (1996) 145

[15] J. R. Friedman, M. P. Sarachik, J. Tejada, R. Ziolo: Macroscopic Measurement of Resonant Magnetization Tunneling in High-Spin Molecules: *Phys. Rev. Lett.* **76** (1996) 3830

[16] D. Gatteschi, R. Sessoli, J. Villain: *Molecular Nanomagnets*: Oxford University Press, New York (2006)

[17] G. Mitrikas, Y. Sanakis, C. P. Raptopoulou, G. Kordas, G. Papavassiliou: Electron Spin–Lattice and Spin–Spin Relaxation Study of a Trinuclear Iron(III) Complex and its Relevance in Quantum Computing: *Phys. Chem. Chem. Phys.* **10** (2008) 743

[18] S. Bahr, K. Petukhov, V. Mosser, W. Wernsdorfer: Pump-Probe Experiments on the Single-Molecule Magnet Fe_8: Measurement of Excited Level Lifetimes: *Phys. Rev. Lett.* **99** (2007) 147205

[19] M. Bal, J. R. Friedman, W. Chen, M. T. Tuominen, C. C. Beedle, E. M. Rumberger, D. N. Hendrickson: Radiation- and Phonon-Bottleneck–Induced Tunneling in the Fe_8 Single-Molecule Magnet: *Europhys. Lett.* **82** (2008) 17005

[20] S. Takahashi, J. van Tol, C. C. Beedle, D. N. Hendrickson, L. C. Brunel, M. S. Sherwin: Coherent Manipulation and Decoherence of S=10 Single-Molecule Magnets: *Phys. Rev. Lett.* **102** (2009) 087603

[21] M. Schlosshauer: *Decoherence and the Quantum-to-Classical Transition*: Springer, Berlin (2007)

[22] F. Meier, J. Levy, D. Loss: Quantum Computing with Antiferromagnetic Spin Clusters: *Phys. Rev. B.* **68** (2003) 134417

[23] J. Tejada, E. M. Chudnovsky, E. del Barco, J. M. Hernandez, T. P. Spiller: Magnetic Qubits as Hardware for Quantum Computers: *Nanotechnology* **12** (2001) 181

[24] F. Troiani, A. Ghirri, M. Affronte, S. Carretta, P. Santini, G. Amoretti, S. Piligkos, G. Timco, R. E. P. Winpenny: Molecular Engineering of Antiferromagnetic Rings for Quantum Computation: *Phys. Rev. Lett.* **94** (2005) 207208

[25] G. A. Timco, S. Carretta, F. Troiani, F. Tuna, R. J. Pritchard, C. A. Muryn, E. J. L. McInnes, A. Ghirri, A. Candini, P. Santini, G. Amoretti, M. Affronte, R. E. P. Winpenny: Engineering the Coupling between Molecular Spin Qubits by Coordination Chemistry: *Nature Nanotechnology* **4** (2009) 173

[26] W. S. Warren, N. Gershenfeld, I. L. Chuang: The Usefulness of NMR Quantum Computing: *Science* **277** (1997) 1688

[27] S. Vega: Fictitious Spin 1/2 Operator Formalism for Multiple Quantum NMR: *J. Chem. Phys.* **68** (1978) 5518

[28] S. Vega, A. Pines: Operator Formalism for Double Quantum NMR: *J. Chem. Phys.* **66** (1977) 5624

[29] C. P. Poole: *Electron Spin Resonance: A Comprehensive Treatise on Experimental Techniques*: Dover Publications, Inc., Mineola, New York, 2nd edn. (1996)

[30] S. Takahashi, S. Hill: Rotating Cavity for High-Field Angle-Dependent Microwave Spectroscopy of Low-Dimensional Conductors and Magnets: *Rev. Sci. Instr.* **76** (2005) 023114

[31] P. J. Turner, D. M. Broun, S. Kamal, M. E. Hayden, J. S. Bobowski, R. Harris, D. C. Morgan, J. S. Preston, D. A. Bonn, W. N. Hardy: Bolometric

Technique for High-Resolution Broadband Microwave Spectroscopy of Ultra-Low-Loss Samples: *Rev. Sci. Instr.* **75** (2004) 124

[32] H. Mahdjour, W. G. Clark, K. Barberschke: High-Senstivity Broadband Microwave Spectroscopy With Small Nonresonant Coils: *Rev. Sci. Instrum.* **57** (1986) 1100

[33] G. Goglio, S. Pignard, A. Radulescu, L. Piraux, I. Huynen, D. Vanhoenacker, A. V. Vorst: Microwave Properties of Metallic Nanowires: *Appl. Phys. Lett.* **75** (1999) 1769

[34] M. L. Stutzmann, M. Lee, R. F. Bradley: Broadband Calibration of Long Lossy Microwave Transmission Lines at Cryogenic Temperatures Using Nichrome Films: *Rev. Sci. Instrum.* **71** (2000) 4596

[35] J. C. Brooth, D. Ho Wu, S. M. Anlage: A Broadband Method for the Measurement of the Surface Impedance of Thin Films at Microwave Frequencies: *Rev. Sci. Instrum.* **65** (1994) 2082

[36] M. Scheffler, M. Dressel: Broadband Microwave Spectroscopy in Corbino Geometry for Temperatures down to 1.7 K: *Rev. Sci. Instrum.* **76** (2005) 074702

[37] E. Ritz, M. Dressel: Influence of Electronic Correlations on the Frequency-Dependent Hopping Transport in Si:P: *physica status solidi* **5** (2008) 703

[38] J. van Slageren, S. Vongtragool, B. Gorshunov, A. A. Mukhin, N. Karl, J. Krzystek, J. Telser, A. Müller, C. Sangregorio, D. Gatteschi, M. Dressel: Frequency-Domain Magnetic Resonance Spectroscopy of Molecular Magnetic Materials: *Phys. Chem. Chem. Phys.* **5** (2003) 3837

[39] O. Ginberg, L. J. Berliner: *Very High Frequency (VHF) ESR/EPR*, vol. 22 of *Biological Magnetic Resonance*: Kluwer Academic / Plenum Publishers, New York (2004)

[40] O. Waldmann, C. Dobe, H. Mutka, A. Furrer, H. U. Güdel: Néel-Vector Tunneling in Antiferromagnetic Molecular Clusters: *Phys. Rev. Lett.* **95** (2005) 057202

[41] F. Luis, F. L. Mettes, J. Tejada, D. Gatteschi, L. J. d. Jongh: Observation of Quantum Coherence in Mesoscopic Molecular Magnets: *Phys. Rev. Lett.* **85** (2000) 4377

[42] E. Roduner: In: *Muon Science: Muons in Physics, Chemistry and Materials*, eds. S. L. Lee, S. H. Kilcoyne, R. Cywinski, Scottish Graduate Series. Inst of Physics Pub (1999)

[43] M. Seck, P. Wyder: A Sensitive Broadband High-Frequency Electron Spin Resonance Electron Nuclear Double Resonance Spectrometer Operating at 5-7.5 mm Wavelength: *Rev. Sci. Instrum.* **69** (1998) 1817

[44] C. G. Montgomery: *Technique of Microwave Measurements*, vol. 11 of *Radiation Laboratory series*: McGraw-Hill, New York (1947)

[45] M. J. Vetter, M. C. Thompson: Absolute Microwave Refractometer: *Rev. Sci. Instr.* **33** (1962) 656

[46] *Software: CST Microwave Studio*: Computer Simulation Technology, Darmstadt, Germany (2006)

[47] P. A. Smith, L. E. Davist, T. W. Button, A. N.McN.: The Dielectric Loss Tangent of Liquid Nitrogen: *Supercond. Sci. Technol.* **4** (1991) 128

[48] R. Berman, D. C. K. MacDonald: The Thermal and Electrical Conductivity of Copper at Low Temperatures: *Proc. R. Soc. Lond. A* **211** (1952) 122

[49] S. Bertaina, S. Gambarelli, T. Mitra, B. Tsukerblat, A. Müller, B. Barbara: Quantum Oscillations in a Molecular Magnet: *Nature* **453** (2008) 203

[50] G. Chabaussant: Mechanism of Ground-State Selection in the Frustrated Molecular Spin Cluster V_{15}: *Europhys. Lett.* **66** (2004) 423

[51] A. Mueller, J. Doering: A Novel Heterocluster with D3-Symmetry Containing Twenty One Core Atoms: *Angew. Chem. Int. Ed.* **27** (1988) 1721

[52] A. Tarantul, B. Tsukerblat, A. Müller: Static Magnetization of V_{15} Cluster at Ultra-Low Temperatures: Precise Estimation of Antisymmetric Exchange.: *Inorg. Chem.* **46** (2007) 161

[53] D. Gatteschi, L. Pardi, A. L. Barra, A. Müller, J. Döring: Layered Magnetic Structure of a Metal Cluster Ion.: *Nature* **354** (1991) 463

[54] A. Tarantul, B. Tsukerblat, A. Müller: High-Field Magnetization of V_{15} Cluster at Ultra-Low Temperatures: Importance of Antisymmetric Exchange and its Precise Estimation: *Chem. Phys. Lett.* **428** (2006) 361

[55] A. W. E. Dilg: Simultaneous Interpretation of Mössbauer, EPR and ^{57}Fe ENDOR Spectra of the $[Fe_4S_4]$ Cluster in the High-Potential Iron Protein I Ectothiorhodospira Halophila: *J. Biol. Inorg. Chem.* **4** (1999) 727

[56] B. Guigliearelli, C. More, A. Fournel, M. Asso, E. C. Hatchikian, R. Williams, R. Cammack, P. Bertrand: Structural Organization of the Ni and (4Fe-4S) Centers in the Active Form of Desulfovibrio Gigas Hydrogenase. Analysis of the Magnetic Interactions by Electron Paramagnetic Resonance Spectroscopy: *Biochemistry* **34** (1995) 4781

[57] J. K. Shergill, R. Cammack, J. H. Weiner: Electron Spin-Echo Envelope Modulation and Spin–Spin Interaction Studies of the Iron–Sulphur Clusters in Fumarate Reductase of Escherichia Coli: *J. Chem. Soc., Faraday Trans.* **87** (1991) 3199

[58] M. Affronte: Molecular Nanomagnets for Information Technologies: *J. Mater. Chem.* **19** (2009) 1731

[59] S. Stoll, A. Schweiger: EasySpin, a Comprehensive Software Package for Spectral Simulation and Analysis in EPR: *J. Magn. Reson.* **178** (2006) 42

[60] F. K. Larsen, E. J. L. McInnes, H. El Mkami, J. Overgaard, S. Piligkos, G. Rajaraman, E. Rentschler, A. A. Smith, G. M. Smith, V. Boote, M. Jennings, G. A. Timco, R. E. P. Winpenny: Synthesis and Characterization of Heterometallic Cr_7M Wheels: *Angew. Chem. Int. Ed.* **42** (2003) 101

[61] S. Piligkos, H. Weihe, E. Bill, F. Neese, H. El Mkami, G. M. Smith, D. Collison, G. Rajaraman, G. A. Timco, R. E. P. Winpenny, E. J. L. McInnes: EPR Spectroscopy of a Family of Cr_7M (M = Cd, Zn, Mn, Ni) "Wheels": Studies of Isostructural Compounds with Different Spin Ground States: *Chem. Eur. J.* **15** (2009) 3152

[62] G. d. Loubens, A. D. Kent, V. Krymov, G. J. Gerfen, C. C. Beedle, D. N. Hendrickson: High Frequency EPR on Dilute Solutions of the Single Molecule Magnet Ni_4: *J. Appl. Phys.* **103** (2008) 07B910

[63] C. J. Bender, L. J. Berliner: *EPR: Instrumental Methods*: Springer, Berlin (2004)

[64] E. Samuel, D. Caurant, D. Gourier, C. Elschenbroich, K. Agbaria: Bis(benzene)chromium. A Sandwich Complex Spin Trap As Revealed by ENDOR Spectroscopy: *J. Am. Chem. Soc.* **120** (1998) 8088

[65] C. Schlegel, van Slageren, J., M. Manoli, E. K. Brechin, M. Dressel: Synthesis, Structures and Magnetic Properties of Two Novel Tetranuclear Iron(III) Single-Molecule Magnets: Enhanced Energy Barriers in Solution: *Polyhedron* **28** (2009) 1834

[66] F. El Hallak, J. van Slageren, J. Gomez-Segura, D. Ruiz-Molina, M. Dressel: High-Frequency ESR and Frequency Domain Magnetic Resonance Spectroscopic Studies of Single Molecule Magnets in Frozen Solution: *Phys. Rev. B* **75** (2007) 104403

[67] R. Sessoli: Large Magnetic Anisotropy in High Spin Clusters; a Route to Magnetic Hysteresis at the Molecular Level: *Mol. Cryst. Liq. Crys.* **274** (1995) 145

[68] J. van Slageren, S. Dengler, J. Gómez-Segura, D. Ruiz-Molina, M. Dressel: Magnetism and Magnetic Resonance Studies of Single-Molecule Magnets in Polymer Matrices: *Inorg. Chim. Acta* **361** (2008) 3714

[69] A. Caneschi, T. Ohm, C. Paulsen, D. Royal, C. Sangregorio, R. Sessoli: Quantum Tunneling of the Magnetic Moment in Manganese and Iron Molecular Clusters: *J. Magn. Magn. Mater.* **177-181** (1998) 1330

[70] A. Cornia, A. C. Fabretti, P. Garrisi, C. Mortalò, D. Bonacchi, D. Gatteschi, R. Sessoli, L. Sorace, W. Wernsdorfer, A. L. Barra: Energy-Barrier Enhancement by Ligand Substitution in Tetrairon Single-Molecule Magnets: *Angew. Chem. Int. Ed.* **43** (2004) 1136

[71] R. L. Novak, F. Pineider, C. d. Julián Fernández, L. Gorini, L. Bogani, C. Danieli, L. Cavigli, A. Cornia, R. Sessoli: Magneto-Optical Studies on the Molecular Cluster Fe4 in Different Polymeric Environments: *Inorg. Chim. Acta* **361** (2008) 3820

[72] G. G. Condorelli, A. Motta, G. Pellegrino, A. Cornia, L. Gorini, I. L. Fragal, C. Sangregorio, L. Sorace: Site-Specific Anchoring of Tetrairon(III) Single Molecule Magnets on Functionalized Si(100) Surfaces: *Chem. Mater.* **20** (2008) 2405

[73] M. Mannini, F. Pineider, P. Sainctavit, C. Danieli, E. Otero, C. Sciancalepore, A. M. Talarico, M. Arrio, A. Cornia, D. Gatteschi, R. Sessoli: Magnetic Memory of a Single-Molecule Quantum Magnet Wired to a Gold Surface: *Nature Materials* **8** (2009) 194

[74] I. A. Alfaleh: http://www.ksu.edu.sa/sites/Colleges/Arabic%20Colleges /CollegeOfScience/physics/Research%20Group/ms/PublishingImages /coile.jpg (2009)

[75] R. Bircher, G. Chaboussant, C. Dobe, H. U. Güdel, S. T. Ochsenbein, A. Sieber, O. Waldmann: Single-Molecule Magnets Under Pressure: *Adv. Func. Mater.* **16** (2006) 209

[76] K. Kambe: On the Paramagnetic Susceptibilities of Some Polynuclear Complex Salts: *J. Phys. Soc. Jpn.* **5** (1950) 48

[77] R. W. Saalfrank, A. Scheurer, I. Bernt, F. W. Heinemann, A. V. Postnikov, V. Schunemann, A. X. Trautwein, M. S. Alam, H. Rupp, P. Muller: The $Fe[Fe(L1)_2]_3$ Star-Type Single-Molecule Magnet: *Dalton Transactions* **23** (2006) 2865

[78] M. Moragues-Cánovas, E. Rivière, L. Ricard, C. Paulsen, W. Wernsdorfer, G. Rajaraman, E. K. Brechin, T. Mallah: Resonant Quantum Tunneling in a New Tetranuclear Iron(III)-Based Single-Molecule Magnet: *Adv. Mater.* **16** (2004) 1101

[79] S. Arrhenius: Über die Reaktionsgeschwindigkeit bei der Inversion von Rohrzucker in Säuren: *Z. Phys. Chem.* **4** (1889) 226

[80] K. S. Cole, R. H. Cole: Dispersion and Absorption in Dielectrics I. Alternating Current Characteristics.: *J. Phys. Chem.* **9** (1941) 341

[81] C. Dekker, A. F. M. Arts, H. W. Wijn, A. J. van Duyneveldt, J. A. Mydosh: Activated Dynamics in a Two-Dimensional Ising Spin Glass: $Rb_2Cu_{1-x}Co_xF4$: *Phys. Rev. B* **40** (1989) 11243

[82] H. B. J. Casimir, F. K. Du Pré: Note on the Thermodynamic Interpretation of Paramagnetic Relaxation Phenomena: *Physica B* **V** (1938) 507

[83] L. Margheriti, M. Mannini, L. Sorace, L. Gorini, D. Gatteschi, A. Caneschi, D. Chiappe, R. Moroni, F. B. d. Mongeot, A. Cornia: Thermal Deposition of Intact Tetrairon (III) Single-Molecule Magnets in High-Vacuum Conditions: *Small* **5** (2009) 1460

[84] E. K. Brechin: Personal communication.

[85] L. Pardi, J. Krzystek, J. Telser, L. C. Brunel: Multifrequency EPR Spectra of Molecular Oxygen in Solid Air: *J. Magn. Reson.* **146** (2000) 375

[86] C. Schlegel, J. van Slageren, M. Manoli, E. K. Brechin, M. Dressel: Direct Observation of Quantum Coherence in Single-Molecule Magnets: *Phys. Rev. Lett.* **101** (2008) 147203

[87] P. Hertz: Über den gegenseitigen durchschnittlichen Abstand von Punkten, die mit bekannter mittlerer Dichte im Raume angeordnet sind: *Mathematische Annalen* **67** (1909) 387

[88] G. Jeschke, A. Schweiger: Zero-field Electron Spin Echo Envelope Modulation Spectroscopy: *Chem. Phys. Lett.* **259** (1996) 531

[89] M. A. Nielsen, I. L. Chuang: *Quantum Computation and Quantum Information*: Cambridge University Press, Cambridge (2000)

[90] J. Krzystek, A. Sienkiewicz, L. Pardi, L. C. Brunel: DPPH as a Standard for High-Field EPR: *J. Magn. Reson.* **125** (1997) 207

[91] P. Hemmer, J. Wrachtrup: Where is my Quantum Computer?: With applications in quantum cryptography, rudimentary quantum computers already exist.: *Science* **324** (2009) 473

Acknowledgments

First and foremost I want to thank my supervisor Joris van Slageren. Without his encouragement, technical help and vast knowledge in the field of molecular magnetism this PhD would have not been possible. Most of the skills I gained during my PhD I learned from him. I thank Professor Martin Dressel for offering me the position in the 1. Physikalisches Institut and his support in many ways. Moreover, I thank Professor Emil Roduner for agreeing to be my second supervisor, and for dedicating so much time and effort to the graduate college.

I want to thank my colleague Fadi El Hallak for numerous fruitful discussions, an efficient sharing of the lab, and just for a very good time. During the last year of my PhD Lapo Bogani joined our institute, he was a big support in my writing process and became a great friend.

Many thanks to all the colleagues from the institue who helped me with discussions, experimental support and much more. Here I would like to mention Gabi Untereiner, Michael Glied, Marc Duran, Bruno Gompf, Shadi Yasin, Eva Rose, Neven Barisic, Matthias Fischer, Stephan Martens, Michael Dumm, Katrin Steinberg, Marc Scheffler, Christian Stehle, Frank Teufel, Nadeschda Kirchner and Agnieszka Cienkowska-Schmidt.

Professor Denninger and Professor Mehring from the 2. Physikalisches Institut I would like to thank for experimental help and useful discussions. Thanks to Hans-Jürgen Kümmerer for his introduction to the W-Band spectrometer. During my measurements at the spectrometer I shared the lab with Gurneet Kaur, thank her very much for the good time together. I will remember Hans-Georg Libuda from the Max-Planck Research school of Advanced Materials as a real supporter of student's affairs. I would like to thank Michael Klann, Peter Brommer and Daniel Steiauf for our weekly meeting and the numerous hints which resulted from those. Märit Djupmyr I want to thank for ongoing motivating support and our extraordinary outdoor activities. Thank to Alexander Weiss for being a friend who is open for any question and discussion.

Without the different workshops this work would not have been possible. I would like to thank the members of the low temperature workshop not only for

a highly reliable supply of liquefied gases, but also for expert support in many experimental questions. I would like the members of the mechanical workshop for their highly skilled work, which is important for every experimentalist. Moreover, I would like to thank the members of the electronics and the electrical workshop for support.

I thank Fernando Luis, Enrique Burzuri and Pepa Martinez from the University of Zaragoza for the fruitful callaboration. Euan K. Brechin and Maria Manoli from the University of Manchester I thank for sample synthesis and basic characterization measurements.

With the other fellows of the Max-Planck-Research School and of the Graduate College I spent great days during workshops and lab tours, I want to thank all of them.

Finally, I thank my parents and my brother for their ongoing support. Katrin, thank you for being there for me.